1-1-1981

Accuracy limitations of CW-lidar for short range distance measurements.

Ralph W. Kettell

ACCURACY LIMITATIONS OF CW-LIDAR FOR SHORT RANGE DISTANCE MEASUREMENTS

by

Ralph W. Kettell, II

A Thesis

Presented to the Graduate Committee

of Lehigh University

in Candidacy for the Degree of

Master of Science

in Electrical Engineering

Lehigh University

1981

This thesis is accepted and approved in partial fulfillment of the requirements for the degree of Master of Science.

Dec. 9, 81
(date)

Professor in Charge

Chairman of Department

Acknowledgements

I would like to acknowledge Professor Nikolai Eberhardt for his assistance in this effort and for the experience gained while working with him. I would also like to acknowledge the Bethlehem Steel Corporation for taking an interest in and funding this research.

Table of Contents

List of Tables

Page

List of Figures

Page

Page

Abstract

The overall accuracy of the distance reading of a previously constructed CW-Lidar system has been expermintally verified for the first time and the measured data are in close agreement with the theory. Alternate methods of Light generation and detection are investigated as possible means of improving and simplifying the system and its performance.

Finally a non-heterodyning system is investigated which uses an infared single mode CW-semiconductor laser and an avalanche photodiode. The performance of such a system should be comparable to the present heterodyning system. The advantages of the semiconductor system are its simplified operation and reduced cost. Additionally the proposed system would require less adjustment and would therefore be much better suited to handle the harsh conditions encountered in an industrial environment. It will be possible to construct such a system as soon as laser diodes become available in a housing adapted for microwave modulation.

Introduction

CW Lidar is a light wave ranging system which employs continuous wave intensity modulation of a laser beam. In its present form, a He-Ne laser is intensity modulated with an electrooptic crystal modulator and focused on a target whose relative position is being measured. The scattered light is received by a telescope, demodulated with a second modulator, and ultimately detected by a photomultiplier tube. The accuracy of the system is limited by the total roundtrip attenuation, the laser power, the quantum efficiency of the photomultiplier tube, and the permissible integration time.

This paper deals with final measurements on the present Lidar system and investigations into alternative transmission and detection schemes. These schemes could be utilized to improve the performance of the present system or would lead to a simpler and a more economical approach to a Lidar system with still acceptable performance. The possible improvements to the system are direct detection of the 4 GHz light signal and direct modulation of the light beam using a semiconductor laser.

System Description

The Lidar system consists of two optical sections, a transmitter and a receiver. The function of the transmitter is to

produce an intensity modulated laser beam and focus it on a target. The receiver's function is to collect the rays scattered off the target and convert them into a modulated electrical signal. The phase angle of the received signal is a measure of the relative position of the target.

The system depicted in Figure 1 utilizes a 5 milliwatt linearly polarized He-Ne laser for the source.[1] It is followed by a lens which focuses the beam through a lithium tantalate ($LiTaO_3$) modulator crystal. The Pockels effect in the crystal is utilized to generate a phase modulation of the laser beam. The phase modulation is converted to intensity modulation by following the crystal with a polarizer oriented perpendicular to the direction of polarization of the laser. The beam then passes through a 20X Galilean collimator which focuses the beam of the target. Finally the transmitted beam must be aligned with the axis of the receiver and this is accomplished with two mirrors. First an adjustable mirror deflects the beam perpendicular to its original path, and secondly a mirror rigidly attached to the face of the telescope aligns the beam with the axis of the telescope.

The receiver section of the instrument consists of a telescope, a crystal modulator, and a photomultiplier tube. The telescope collects the scattered light from the target and focuses it onto a $LiTaO_3$ crystal. The crystal demodulates the light with a microwave signal which is locked 420 kHz away from the original microwave

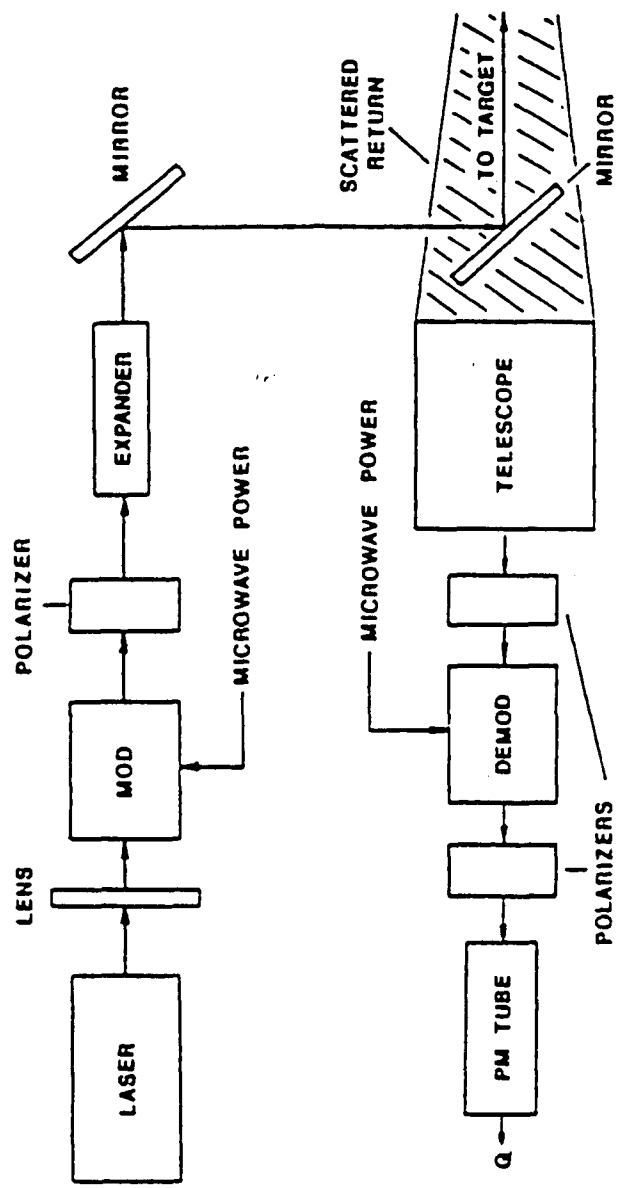

Figure 1 : Schematic of the Lidar system.

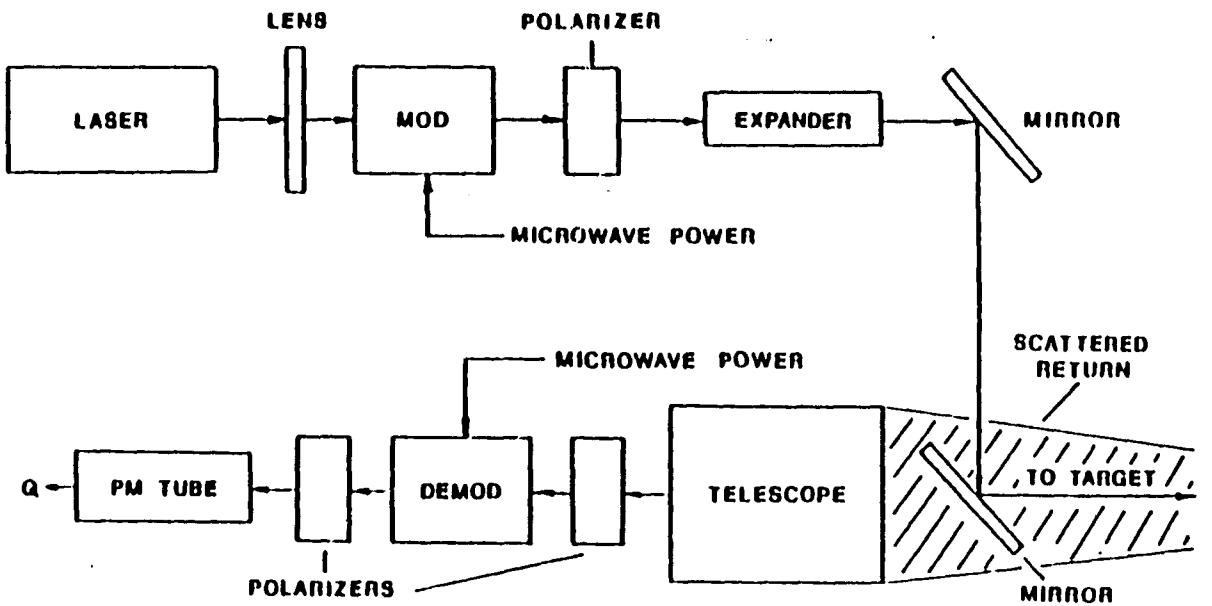

Figure 1 : Schematic of the lidar system.

modulating frequency. This produces an optical signal at 420 kHz which contains the desired phase information. The photomultiplier tube then converts the light signal into an electrical current with amplitude and phase proportional to the optical signal.

In order to determine the phase delay, the signal from the photomultiplier tube is compared to a reference signal which is derived by directly mixing the two microwave modulating signals together. The relative target distance can be ascertained by appropriately scaling the phase.

Optical Losses

The total losses in the system have been discussed previously in [1] and [2]. Their findings indicate that the primary losses in the system are the scattering loss due to the beam scattering off the target and the depth focus limitation. These losses account for the majority of the degradation in the received signal to noise ratio, which determines the overall accuracy of the system. The major source of noise in the system is quantum noise in the light signal, and therefore the signal to noise ratio is highly dependant upon the light signal intensity incident on the tube. This implies that the signal to noise ratio could be improved by either increasing the laser power or decreasing the attentuation of the optical system.

The roundtrip attenuation can be separated into three categories: transmitter losses, scattering losses, and receiver losses. The transmitter and receiver losses occur in their respective sections and result from the various operations which are performed on the laser beam. The scattering losses are caused by the beam scattering off the target and the subsequent fractional recovery of the dispersed light.

The roundtrip attenuation of the present system is as follows:

	Light Power	Attenuation
Laser Power	4 mW	0.5 dB
After lens	3.6 mW	7.1 dB
After 1st Modulator	0.7 mW	2.4 dB
Transmitter Output	0.4 mW	48.0 dB
Telescope Input	6.34 nW	13.4 dB
After 2nd Modulator	0.286 nW	6.0 dB
Total Attenuation		77.4 dB

The sources of this attenuation will now be discussed. The first lens has an attenuation of 0.46 dB which is due to reflection from its two uncoated surfaces. The 7.1 dB loss occurs in the first modulator and the Nicol prism polarizer, but the polarizer contributes little to the attenuation figure because its surfaces are coated. The crystal has a reflection coefficient of 0.371 and thus only 45% of the light passes through it. This accounts for

3.46 dB of the loss. The other 3.64 dB are attributed to non-idealities in the test setup, in particular dust which is attracted to the crystal by the high electrostatic fields present in the modulator housing. In a better design the 7.1 dB loss of the present system could be reduced to approximately 4 dB.

The remaining 2.4 dB of transmitter loss occurs in the collimator and on the two mirror surfaces. The collimator has two uncoated lens surfaces which cause 0.46 dB of attenuation, and the rest can be accounted for by imperfections in the mirrors and lenses and dust on their surfaces. The 2.4 dB figure could be reduced to 1.2 dB in a better setup and thus the optimum transmitter attenuation would be approximately 5.4 dB.

The 48 dB loss between the transmitter and receiver is the scattering loss. This loss is calculated from [2] Equation (27), and is the result of scattering off a Lambertian target with a reflectivity of 0.18 (graphite), received at a distance of 126 inches with an aperture of 3.5 inches. The scattering loss could be reduced either by reducing the distance from the target or by increasing the size of the aperture. The first option is not feasible because the system has a fixed target distance. The second option, however, is feasible with the primary drawback being a large increase in cost. If an eight-inch telescope was used, the scattering loss would be 41 dB and an eleven-inch telescope would yield a scattering loss of 38 dB.

The next source of attenuation is the telescope and second modulator and they account for 13.4 dB. Of this, 3 dB result from unpolarized light from the target passing through a polarizer. The other 10.4 dB is due to reflection from the crystal and lens surfaces, dust in the modulator housing, and non-idealities in the light ray geometry. In an optimal design the 10.4 dB loss could be reduced to 5.5 dB which along with the inherent polarization loss would yield 8.5 dB. Finally the 6 dB loss due to the laser filter could be reduced to 4 dB if a wider band filter was used. However, the wider band filter would result in a somwhat noisier signal input to the photomultiplier tube.

Ultimately in an optimal design the 77.4 dB roundtrip attenuation could possibly be reduced to 66 dB. Of this 18 dB (presently 29.4 dB) would be in the receiver and transmitter and the other 48 dB due to scattering. If an eleven-inch telescope was used in the receiver, the overall attenuation would be further reduced to 56 dB.

System Accuracy

Noise in the received signal has the effect of causing random fluctuations in the distance reading. The magnitude of these fluctuations relates directly to the amount of noise in the system. This relationship is given by Eq.(47) [1] and is as follows:

$$(1) \qquad \Delta = \frac{\lambda_m}{2}\sqrt{\frac{i^2}{I^2_{rms}}} = 37.5 \text{ mm}\sqrt{\frac{i^2}{I^2_{rms}}}$$

where Δ is the root mean square deviation in the distance measurement and the quantity under the square root is the inverse signal to noise power ratio. The signal to noise ratio in the phase measurement system is proportional to the noise bandwidth of the system. Thus including noise bandwidth in the equation gives:

$$(2) \qquad \Delta = 37.5 \text{ mm}\sqrt{(N/S)_1 \, B}$$

where $(N/S)_1$ is the noise to signal ratio normalized for a bandwidth of one hertz and B is the equivalent noise bandwidth of the system. Equation (2) indicates that a smaller bandwidth will yield a smaller standard deviation. However, a decrease in the bandwidth causes an increase in the integration time which in turn decreases the rate at which readings may be taken. Therefore a tradeoff must be made between the accuracy of the readings and the rate at which data is acquired.

With the present system configuration, i.e. roundtrip attenuation of 77.4 dB and quantum efficiency of 5%, an accuracy of 0.2 mm can be measured in $^1/_{10}$ second or 0.06 mm in 1 second. With an improved attenuation figure of 66 dB and a better quantum efficiency of 15%, 0.2 mm could be measured in $^1/_{400}$ second or 0.06 mm in $^1/_{40}$ second. Further if a larger telescope, which would yield an attenuation of 56 dB were used, an accuracy of 0.03 mm could be

measured in $^{1}/_{100}$ second and 0.01 mm in $^{1}/_{10}$ second. These numbers provide examples of the tradeoffs between the speed and accuracy of measurements for various S/N ratios.

Another theoretical limitation to the accuracy of the present laboratory system lies in the phase measurement section. This inaccuracy amounts to a maximum of ±0.15 mm and is the result of analog multiplication errors. These errors are caused by slight imperfections in the parabolic I-V characteristics of the multipliers. These errors could be reduced to ± 0.1 mm if two of the multipliers were eliminated and replaced by low pass filters to remove the 840 kHz harmonic component. Therefore increases in the signal to noise ratio beyond a certain point just provide an increase in the data acquisition rate, because the final accuracy is limited by the analog errors. It also seems that these errors could be eliminated entirely if a zero crossing detection scheme was used instead of the crosscorrelation scheme. A comparison of these schemes is presented in a later chapter on zero crossing phase detection.

Linearity Measurements

The overall accuracy of the Lidar system had to be determined and therefore distance readings were recorded over its full range to verify the linearity(analog errors). These measurements were accomplished by using a graphite target mounted on a calibrated

moveable stage. After each reading was recorded, the target position was incremented by 0.5 mm and another reading taken. This process was repeated 100 times to obtain a linearity plot for the system over 50 mm of travel. After all the readings were recorded, they were plotted on a Hewlett Packard plotter attached to the HP9815 computer, and the plot is presented in Figure 2. As shown in the figure the accuracy of the system is reasonably good, deviating from the theoretical line by at most 0.4 mm. However, the accuracy is less than the predicted value of ±0.15 mm, which was expected from analog multiplication errors. The additional errors can be attributed to discontinuites incurred when the circuitry switches between tangent and cotangent signals depending on the quadrant in which the phase angle is located.

Theory of RMS Distance Error

The RMS distance error of the overall system is a function of the signal to noise ratio as shown in Eq.(1). This is then transformed in Eq.(2) in terms of a normalized signal to noise ratio and the equivalent noise bandwidth, and the noise level varies directly with the bandwidth. Thus if low pass filters (as described in the next chapter) were inserted into the phase measurement system after the multipliers, the signal to noise ratio and the RMS deviation would improve. However to determine the amount of the improvement, the noise overall bandwidth of the system with the filters must be determined.

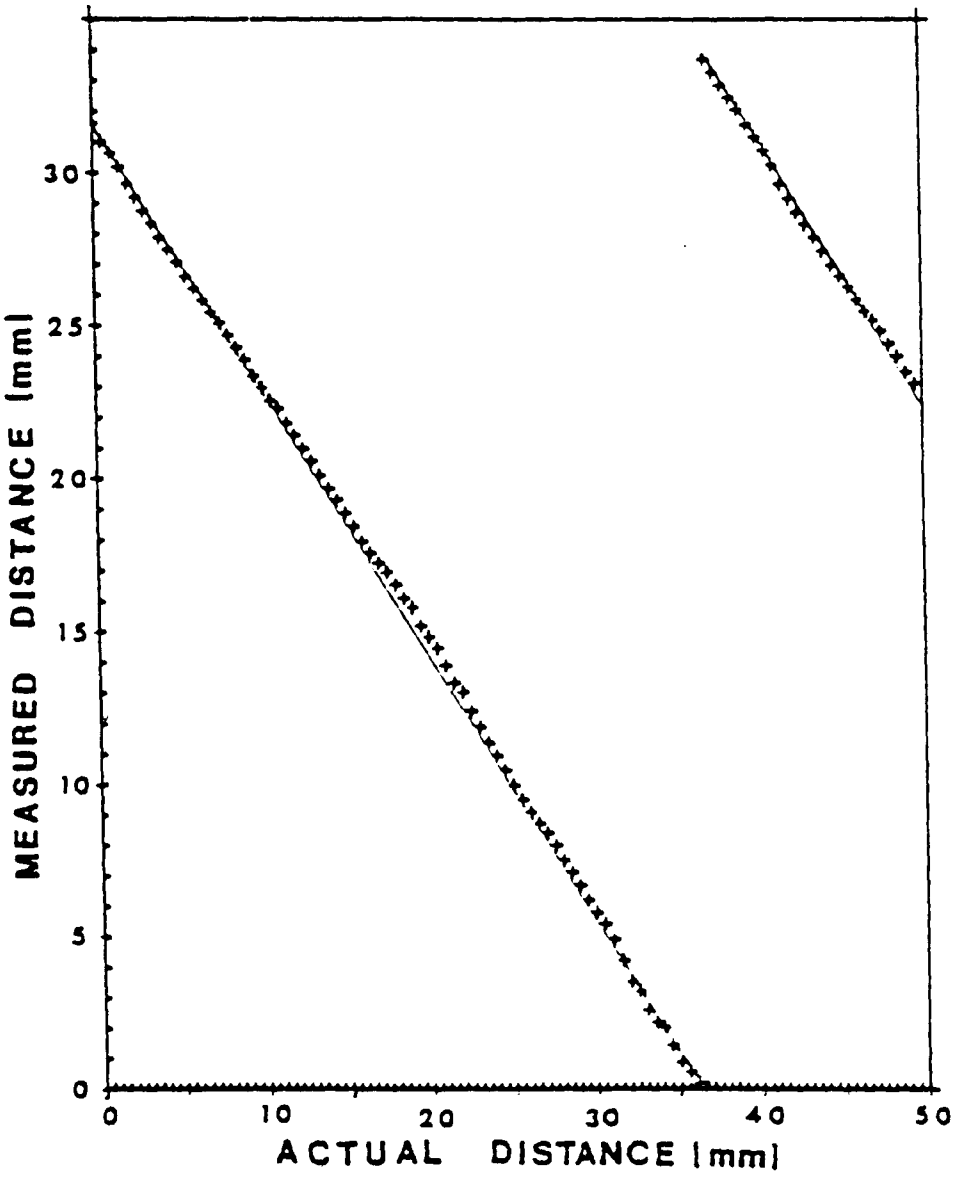

Figure 2 : Lidar System Linearity Plot.

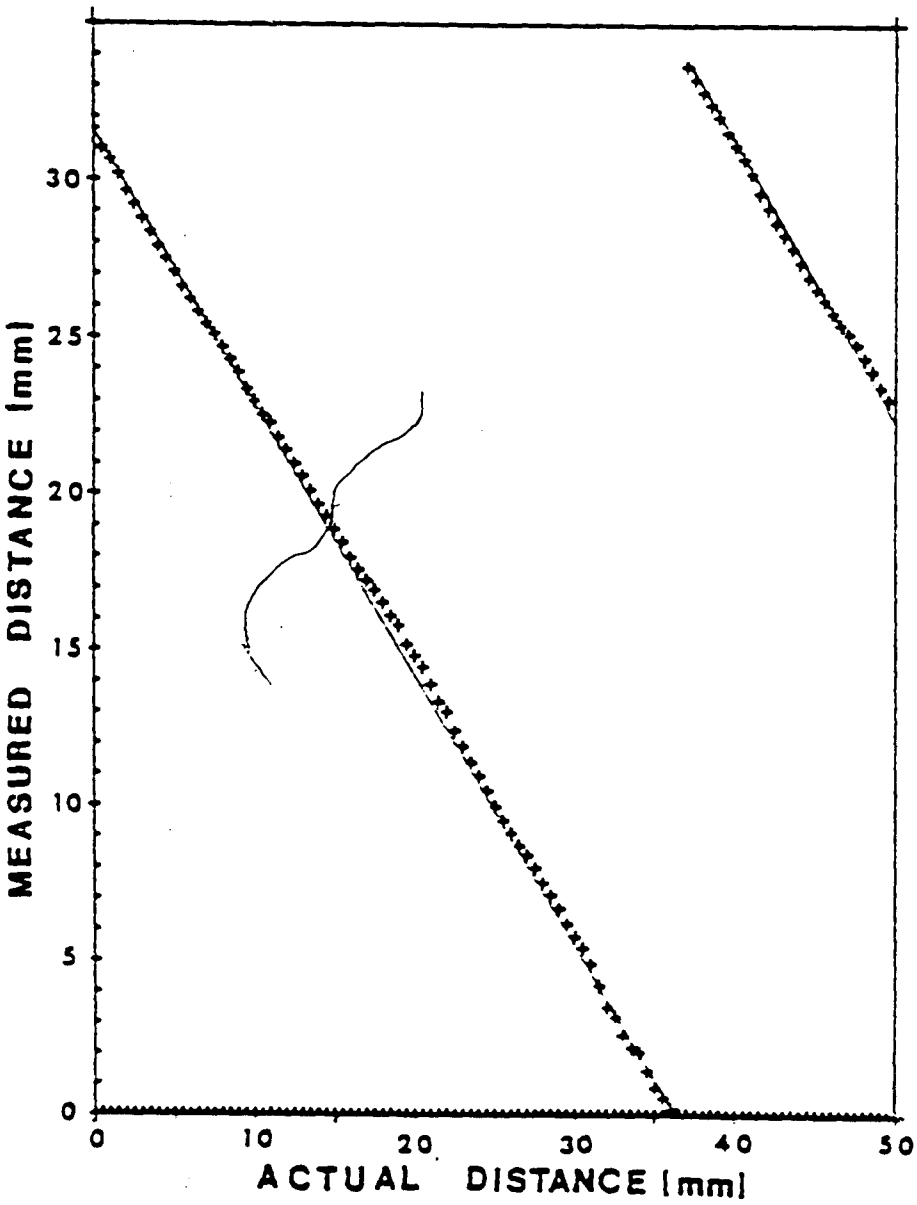

Figure 2 : Lidar System Linearity Plot.

The two devices in the Lidar system which affect the equivalent noise bandwidth are the 420 kHz amplifier and the low pass filters mentioned above. The noise is first limited to a bandwidth of 16 Hz by the amplifier and is then further reduced by the bandwidth of the low pass filters. The noise equivalent bandwidth of the system is defined as:

$$(3) \qquad B_n = \frac{1}{\left|H(f)\right|^2_{max}} \int_0^\infty \left|H(f)\right|^2 df$$

where H(f) is the amplitude response of the system and $\left|H(f)\right|_{max}$ is the maximum value of the amplitude curve. The amplitude response of the Lidar System is the product of the low pass filter response and the 420 kHz amplifier response shifted down by the amount of the intermediate frequency. Therefore the IF must be known to calculate the equivalent noise bandwidth, because the shape of the systems response curve is highly dependant upon the IF. For instance if the intermediate frequency is located at the center frequency of the amplifier, the system response will be its narrowest because the modulation will cause the upshifted and downshifted spectra to exactly overlap. However if the intermediate frequency is larger or smaller, the response curve will be flatter and broader, because the spectra will not precisely overlap. Therefore the equivalent noise bandwidth and the standard deviation will be larger if the IF signal is not centered on the amplifiers response curve. In conclusion, the two variables which are needed to calculate the RMS distance deviation are the signal to noise ratio and the IF.

The theoretical curves were plotted on a CDC 6400 computer. A flowchart of the program which accomplished the plotting is presented in Appendix C. The inputs to the program are the signal to noise ratio and the intermediate frequency. Initially the program uses the IF to compute the shifted amplifier response. This response is stored, and a product of the stored curve and the low pass filter response is formed. The resulting curve is squared and numerically integrated. The integration sum is then divided by the square of the maximum value of the stored response curve to give the equivalent noise bandwidth. Finally, the number is multiplied by a scale factor which the computer determines from the S/N ratio, and the square root is taken. The final result is the standard deviation of the system for the given low pass filter bandwidth. The above calculation is then repeated for several low pass filter bandwidths and a curve is plotted with the resulting data. Two curves obtained in this manner are shown in Figures 7a and 7b.

In conclusion, the RMS deviation is a function of the intermediate frequency and the signal to noise ratio. The S/N ratio has a direct effect on the amplitude of the noise and is not frequency dependant. However, the influence of the IF on the deviation is more subtle. It influences the width of the response curve and so it affects the distance deviation, but its effect is dependant upon the bandwidth of the low pass filter. For small filter bandwidths it will have little effect but for larger bandwidths it will have a greater effect, and thus the shape of the

resulting theoretical curve is highly dependant upon the IF.

Measurement of RMS Distance Error

In order to calculate the RMS distance deviation, a large number of samples must be taken. Also the readings must be acquired quickly enough that the thermal drift in the laboratory system does not affect the measurement. To verify the RMS distance error theory, The RMS deviation must be measured for several low pass filter bandwidths and two optical signal levels. In order to calculate the theoretical curves, several parameters must be determined. These are the the low pass filter response, the 420 kHz amplifier response, the S/N ratio, and the IF. They are determined as follows.

To provide for adjustment of the integration time, two variable bandwidth low pass filters were constructed and inserted in the phase measurement system just after the analog multipliers. These filters can be used to vary the integration time from $^{1}/_{100}$ second to 8 seconds. They are two pole VCVS low pass filters with maximally flat Butterworth response. The circuit diagram of the filters is given in Appendix B along with a mathematical analysis and response curve. These filters will improve the S/N ratio of the system, but at the same time they limit the data rate of the system.

The response curve of the 420 kHz amplifier is shown in Figure

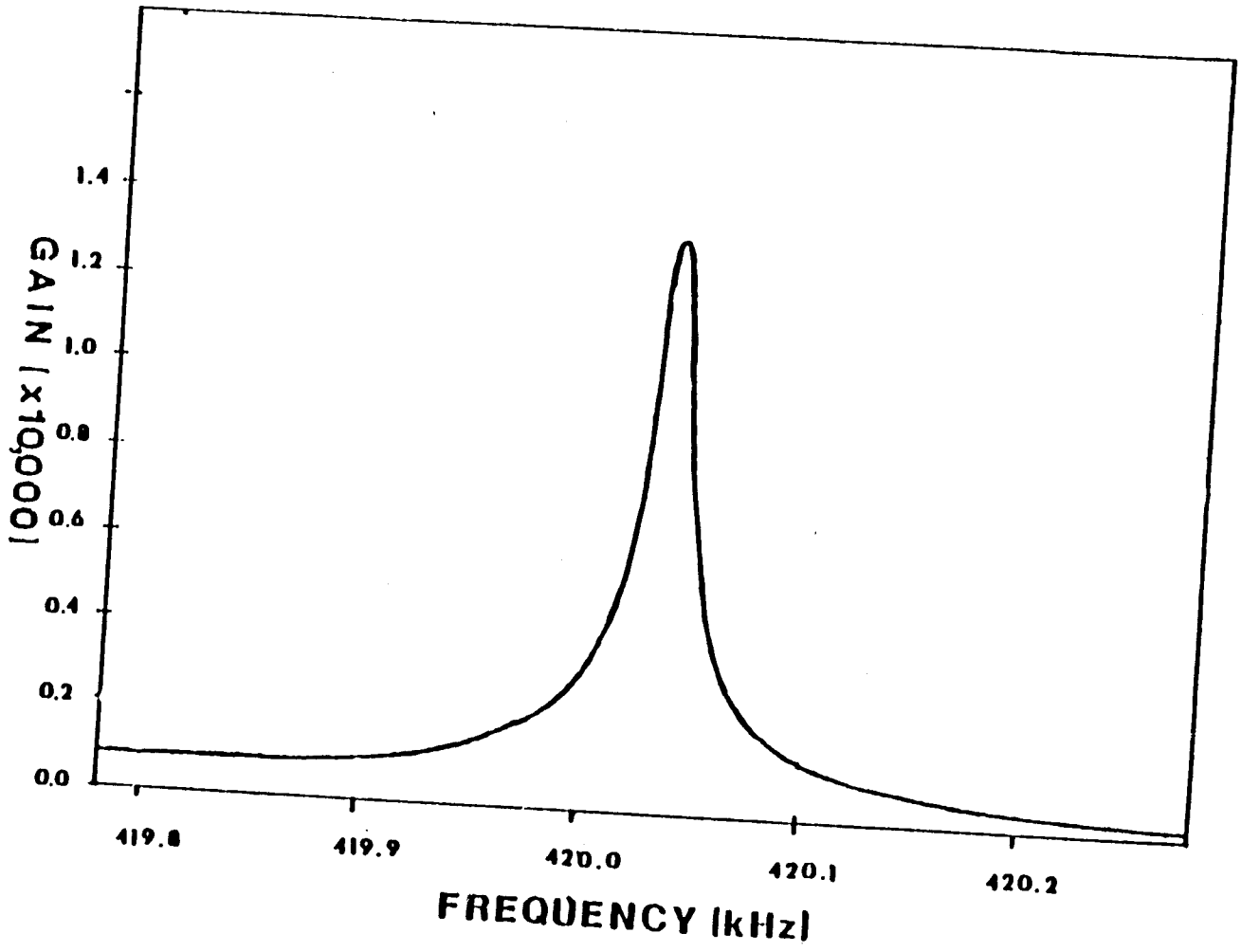

Figure 3 : Response curve of the 420 kHz amplifier

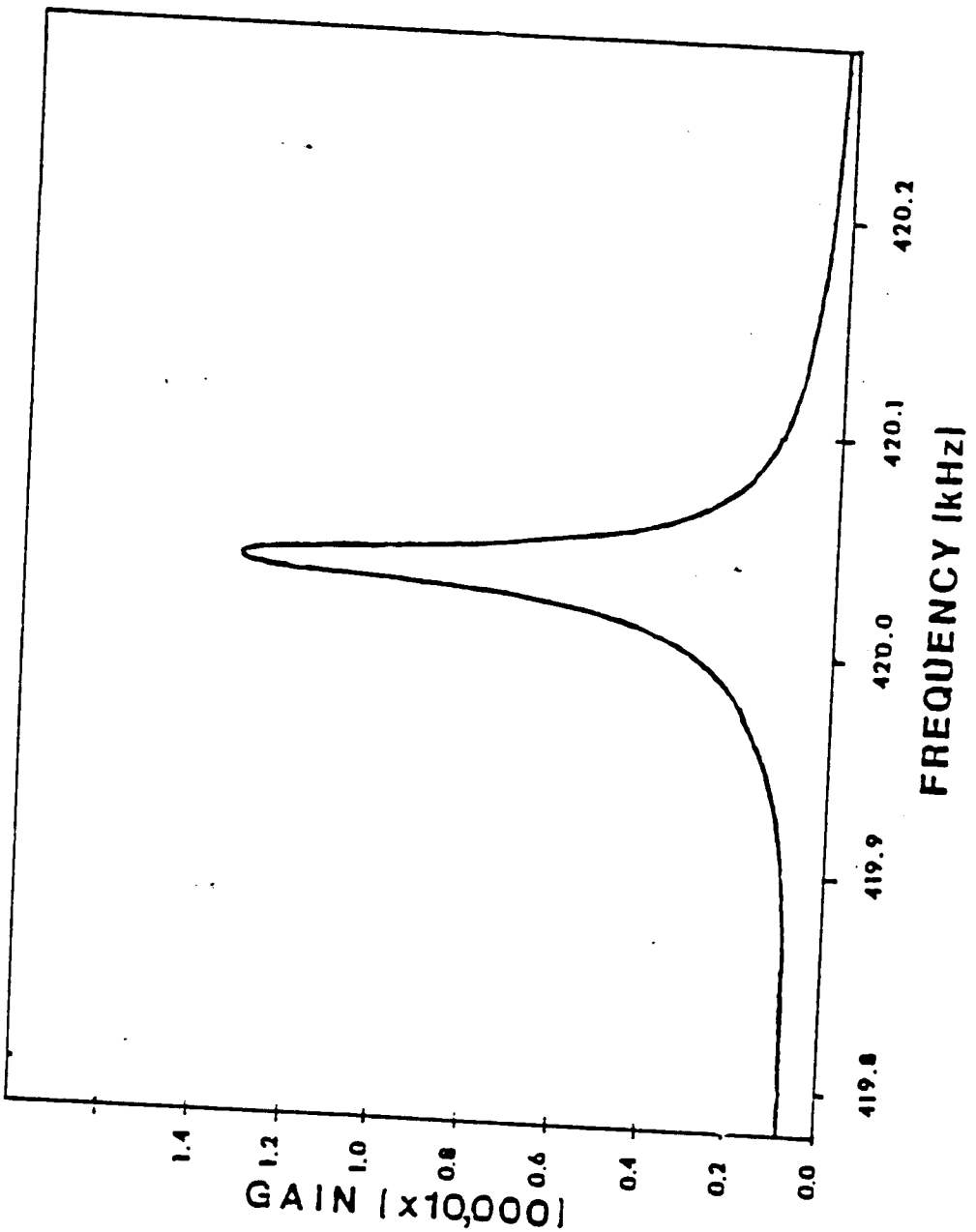

Figure 3 : Response curve of the 420 kHz amplifier

3. It was measured by connecting the input of the amplifier to a signal generator and the output to an oscilloscope. With the input level held constant, the frequency was incremented and the output was measured on the scope. The values were recorded and later plotted.

The S/N ratio and the IF have yet to be determined. They are measured with the aid of the computer and a Hewlett Packard 9853 Selective Level Meter. The receiver (HP9853) communicates with the computer via the IEEE 488 instrumentation bus. A program was written for the HP 9815 to step the frequency of the Selective level meter from 419.990 kHz to 420.090 kHz in one hertz steps. For each frequency the signal level was read by the computer and plotted on the plotter. Two plots obtained using this technique are shown in Figures 6a and 6b. The signal to noise ratio and the IF can both be determined from these plots. The S/N is measured by reading the maximum signal level and the noise level from the curve and forming the difference. The IF is then just the frequency on the plot where the signal is at a maximum.

Initially an attempt was made to take the RMS error measurements manually, but this did not succeed because the process was too slow and thermal drift influenced the measurements. Therefore in order to take reading rapidly enough, an interface was built to provide for automated measurement of the distances using the Hewlett Packard 9815 computer. The HP 9815 communicates with

external instruments via an IEEE standard 488 bus and the interface was built to interact accordingly. A schematic and a timing diagram of the interface is presented in Appendix A and a block diagram is shown in Figure 4. The primary function of the interface is to read the address from the bus, determine which data byte is being requested and ultimately put the appropriate data on the bus line.

A schematic of the IEEE-488 bus is shown in Figure 5. Each instrument on the bus is assigned an address or addresses so that it knows when to talk or listen. Additionally one instrument on the bus is the controller and it controls communication on the bus. In this case the controller is the computer (HP 9815) and it initiates communication with the Lidar system by setting the ATN line low. This causes the listener (Lidar interface) to set the NRFD and NDAC lines low, indicating it is ready to receive the address. Next the controller sets the DAV line low which tells the listener that the address is available on the bus. The listener proceeds by reading the address from the bus. Upon completion of the read cycle the listener sets NDAC high, indicating the data has been accepted. The controller then sets DAV high and in turn the listener sets NDAC low and NRFD high. Finally, the controller sets the ATN line high which indicates that the address cycle is complete. When the ATN line goes high, the Lidar system becomes the talker and the controller (HP 9815) becomes the listener.

After the ATN line is set high, the listener (HP 9815) sets the NRFD and NDAC lines low. This causes the talker (Lidar) to place

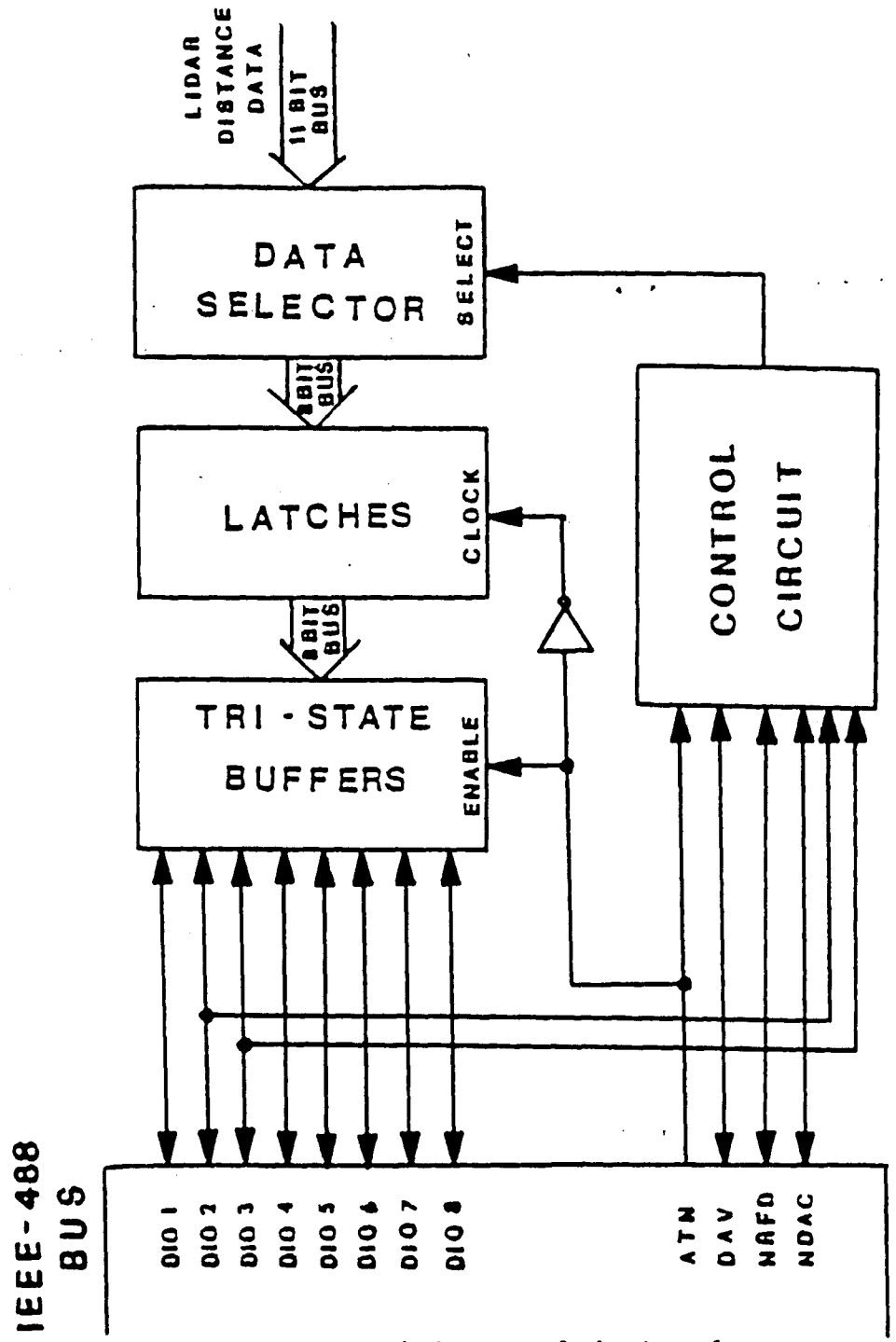

Figure 4 : Block diagram of the interface.

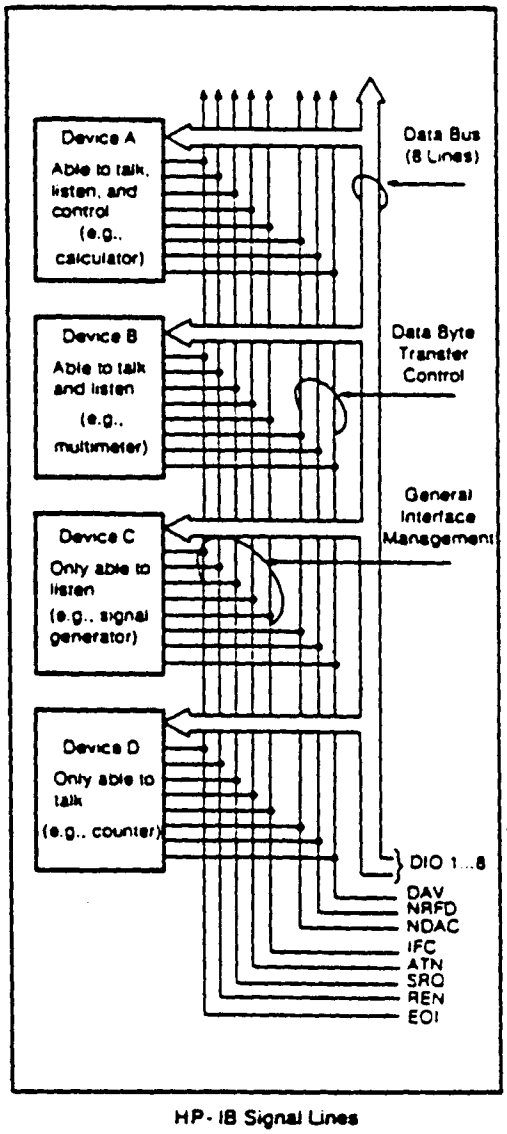

Figure 5 : Schematic of the IEEE-488 bus.

data on the bus lines and set DAV low. Then the computer reads the data byte and sets NDAC high. In turn the talker sets DAV high which causes the listener (HP 9815) to set NDAC low and NRFD high, completing the read cycle.

As shown in Figure 5, the IEEE-488 bus consists of sixteen lines ; however, only eight of them are data lines. It is therefore only possible to transfer eight bits of information at a time. This presents somewhat of a problem because the distance data consist of eleven bits of information. The problem is solved by sending the data in two read cycles as an eight bit byte and a three bit byte. When the interface receives an address of four it sends the lower eight bits of the binary distance data and when it receives an address of six it sends the higher three bits of information.

A program was written for the Hewlett Packard computer to record the distance readings. It first executes a read byte instruction with a bus address of four, which causes the interface to send the lower eight bits of the distance reading. This number is divided by 100 to account for the decimal point in the distance reading. The computer then executes a read byte instruction with a bus address of six to read the higher three bits of the distance data. This value is scaled by 2.56 and added to the lower byte to obtain the distance reading. This process is repeated 100 times and the standard deviation of the hundred readings is calculated. The result is the RMS distance error.

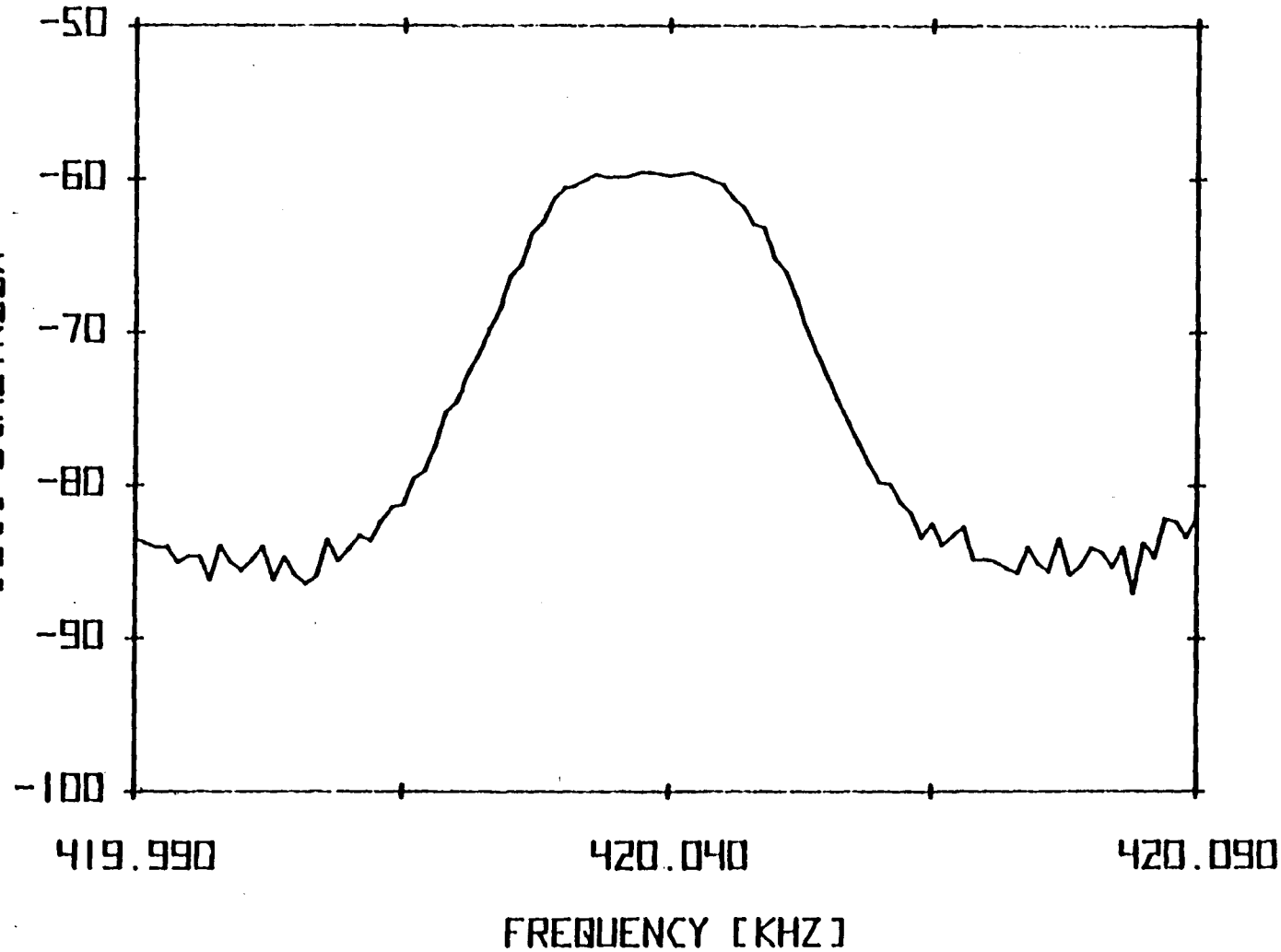

Figure 6a : Signal to noise ratio plot(S/N = 26dB)

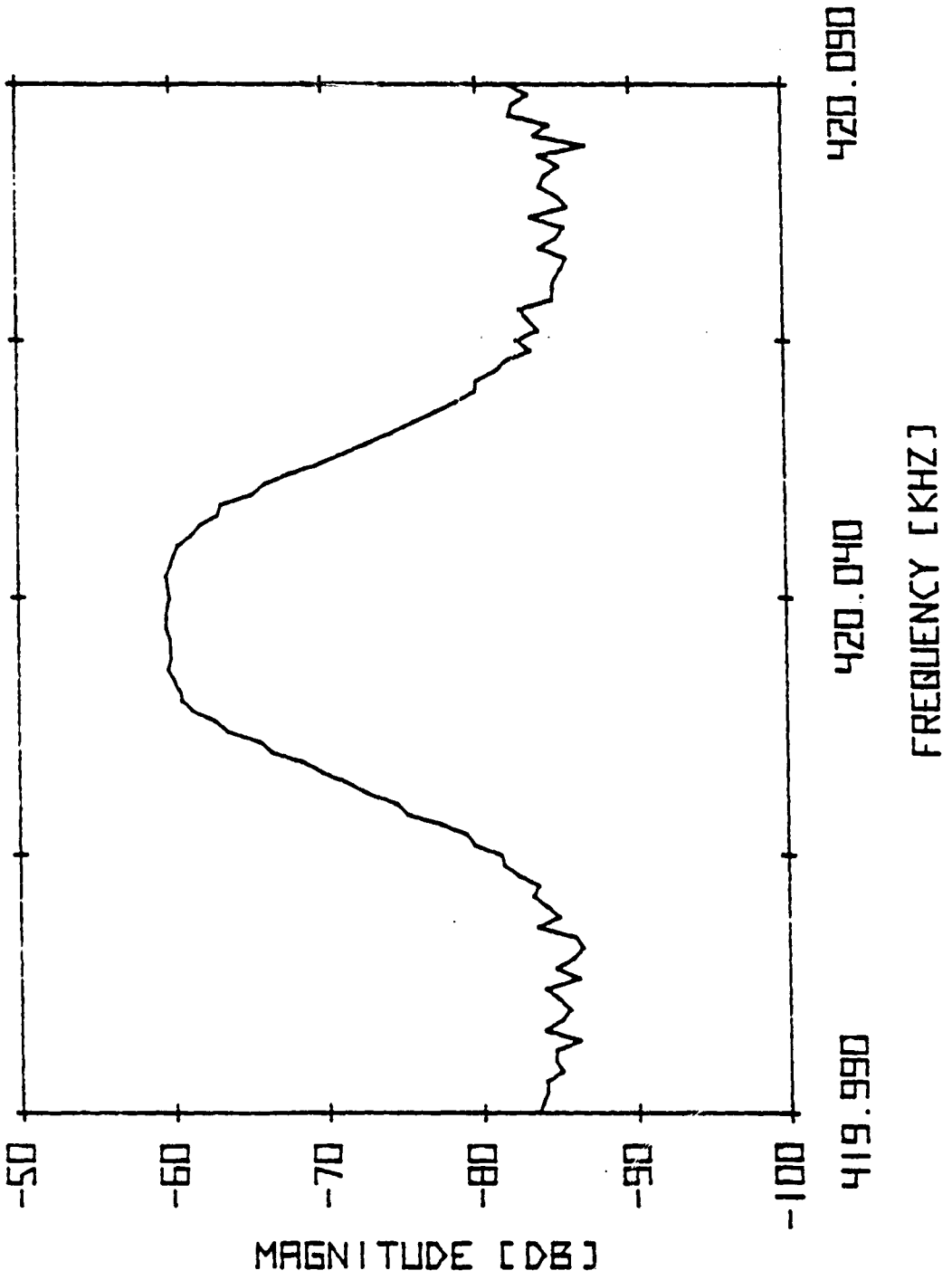

Figure 6a : Signal to noise ratio plot(S/N = 26dB)

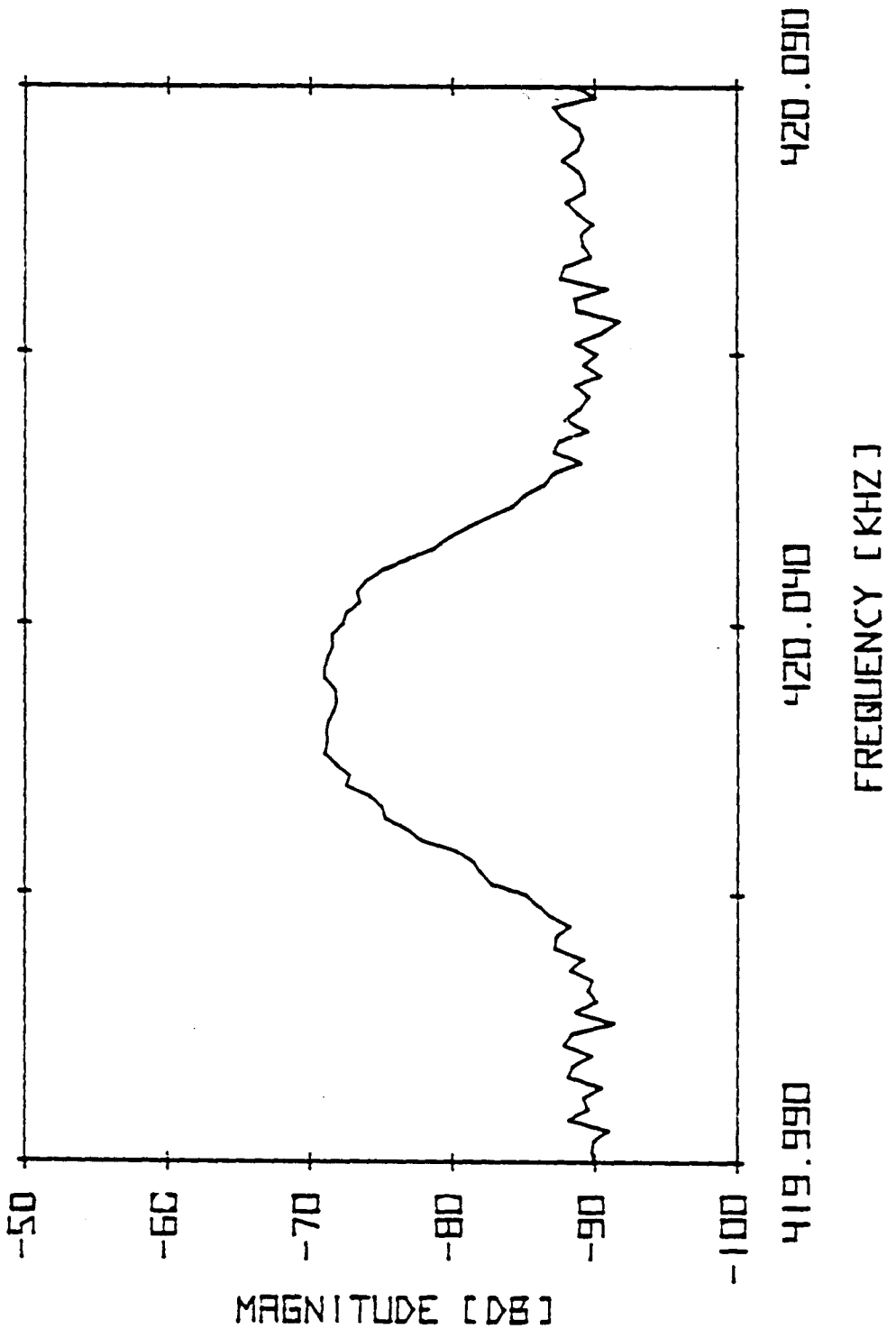

Figure 6b : Signal to noise ratio plot(S/N = 17.5dB).

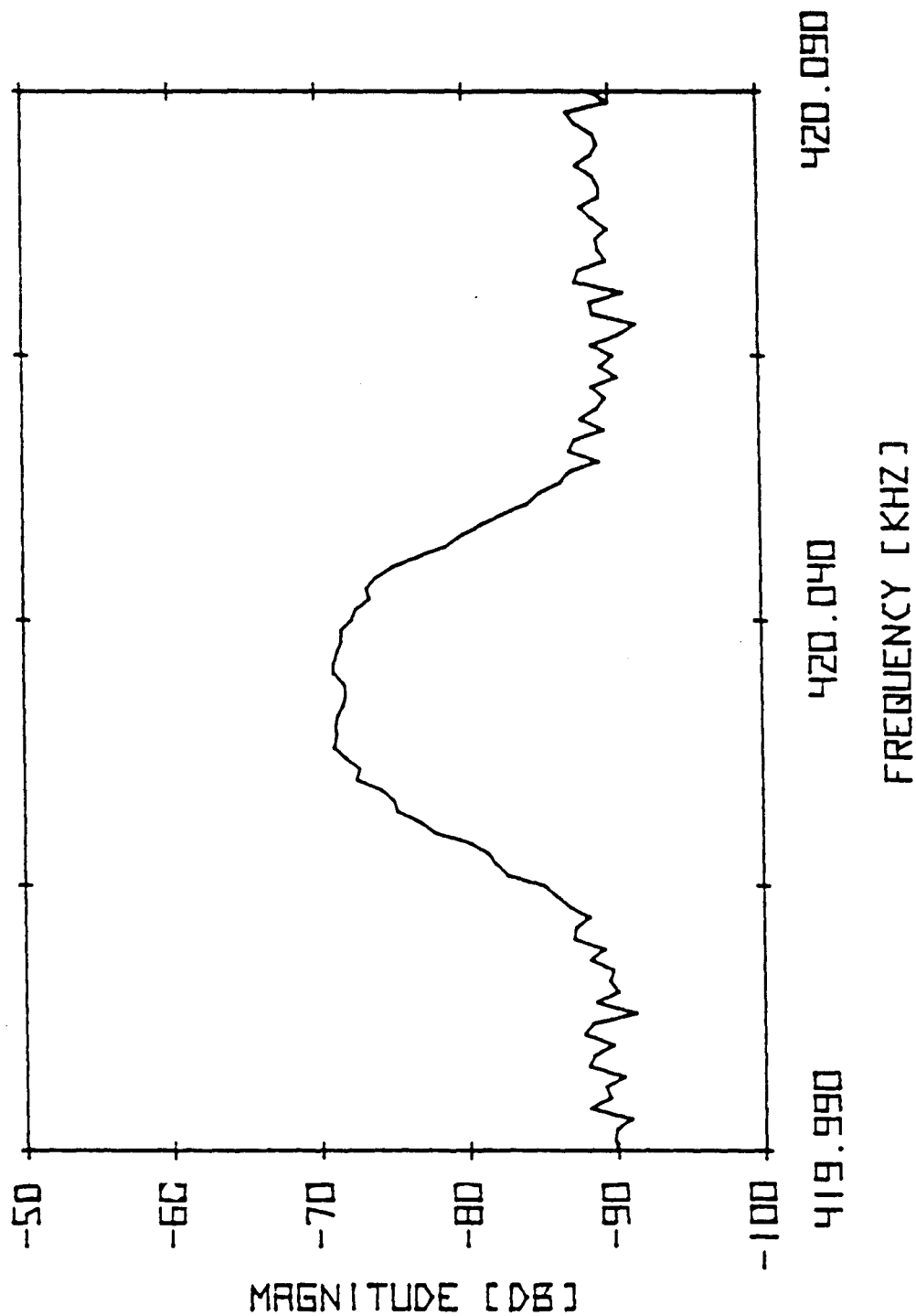

Figure 6b : Signal to noise ratio plot(S/N = 17.5dB).

The procedure that was used to measure the RMS distance error is as follows. First the S/N ratio and IF frequency were measured as described in the previous chapter. This provided the data needed to plot the theoretical distance error curveas desribed earlier. The theoretical curve was plotted on the CDC 6400. Next the low pass filter bandwidth was set at 0.1 Hz and the Hewlett Packard computer utilized to measure the RMS error of 100 distance samples. The error was measured five times for each filter bandwidth and the five values averaged to produce the final result. Next the filter bandwidth was increased and the RMS error was measured again. This process was repeated for several filter bandwidths up to 100 Hz. After the measurements were taken, the measured RMS distance error was plotted versus the filter bandwidth on the same plot as the theoretical RMS error curve.

As mentioned previously the RMS error had to be measured at two optical signal levels to properly verify the theory. First the system was optically aligned in the best possible manner and this resulted in a S/N ratio of 26 dB. The signal to noise plot for this configuration is shown in Figure 6a. The RMS distance errors were then measured per the above procedure and this gave the distance error plot shown in Figure 7a. Next a 10% transmission optical attenuator was placed in the light path and this yielded a signal to noise ratio of 17.5 dB. The S/N plot for this configuration is given in Figure 6b, and the RMS error plots resulting from measurements are pictured in Figure 7b. Additionally the measured

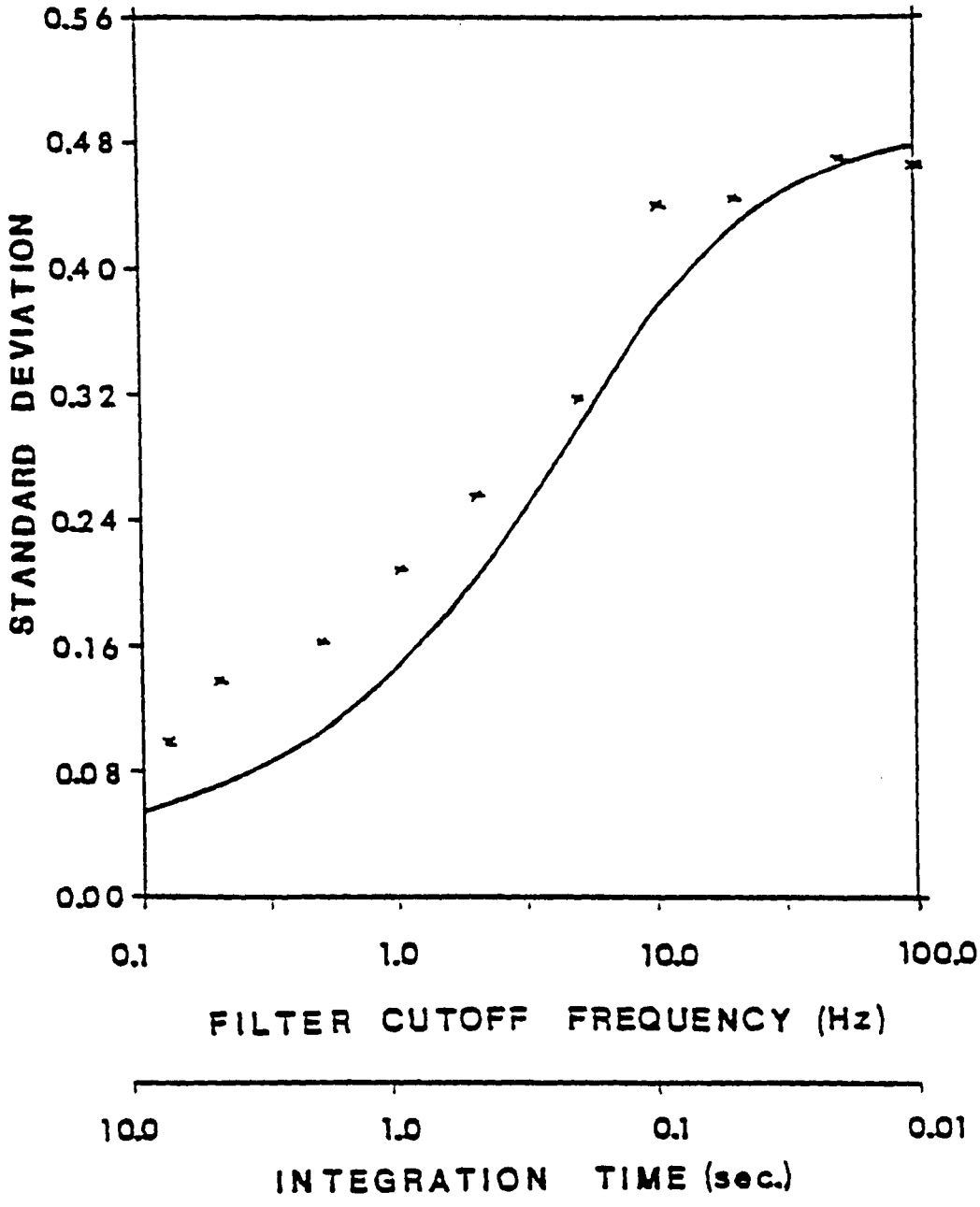

Figure 7a : RMS Distance Error Plot(S/N = 26dB).

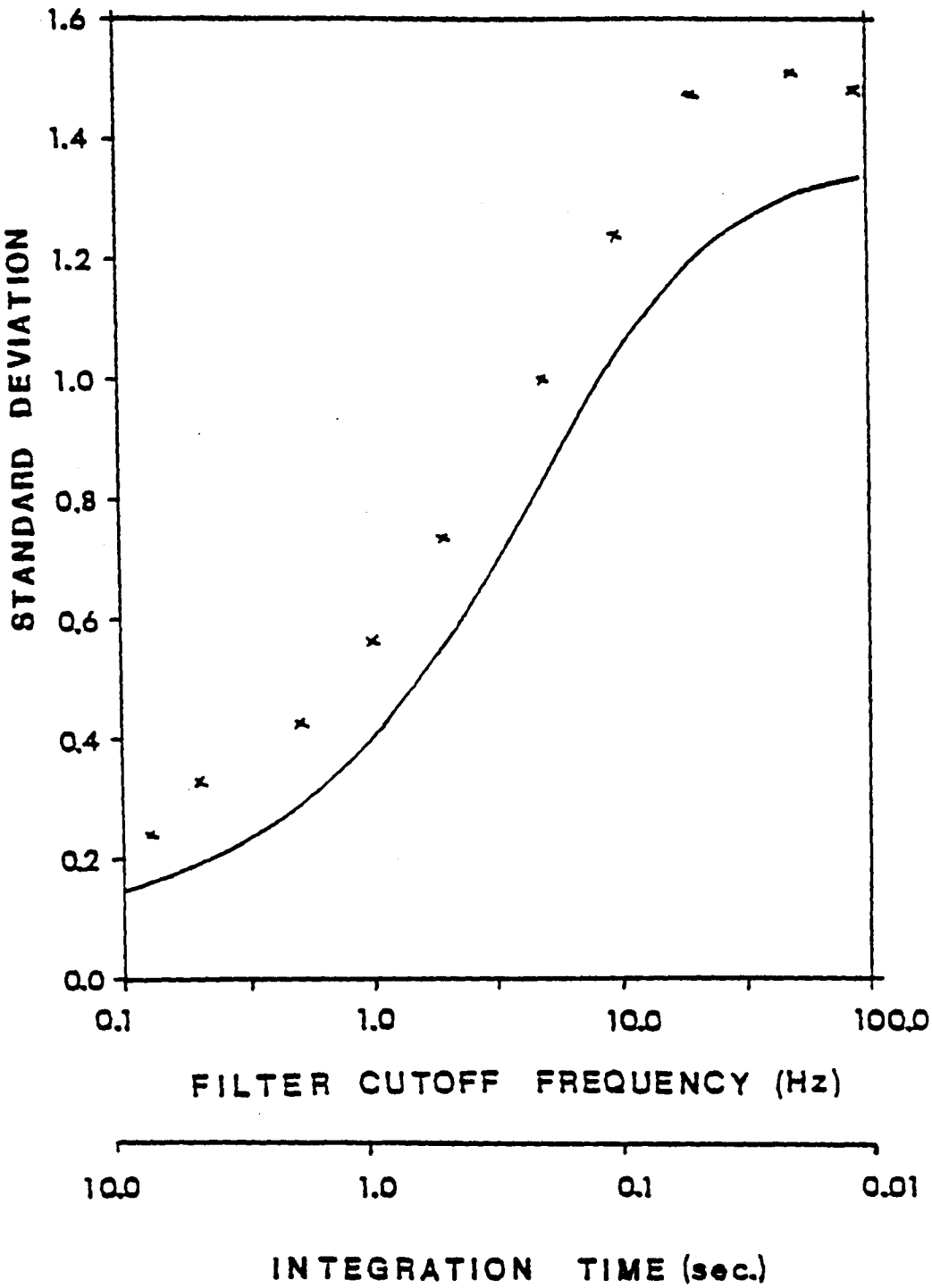

Figure 7b : RMS Distance Error Plot(S/N = 17.5dB).

data are listed in Table 1.

INTEGRATION TIME(SEC)	STANDARD DEVIATION (mm)	
	S/N = 26 dB	S/N = 17.5 dB
8	0.101	0.245
5	0.137	0.331
2	0.162	0.426
1	0.208	0.570
0.5	0.256	0.726
0.2	0.328	1.031
0.1	0.441	1.267
0.05	0.456	1.476
0.02	0.473	1.493
0.01	0.467	1.453

Table 1 : Measured Values of Standard Deviation

In conclusion, these measurements for the first time verify the performance of the entire Lidar system. The close fit of the measured data to the theoretical data, as demonstrated in Figure 7, verifies the RMS distance error theory presented herein and the phase angle estimation theory in [1].

Zero Crossing Phase Detection

As mentioned previously the cross correlation phase detection scheme of the present system introduced ±0.15 mm in errors due to the analog multipliers. These errors could be eliminated if a zero crossing detection scheme was used because the multipliers would be

eliminated. The detector would operate by measuring the time delay between the zero crossing of the distance signal and the reference signal. The time delay could then be scaled by an appropriate amount to give the phase angle or the relative distance. It has been shown in [1] Eq.54 that the zero crossing scheme will provide the same accuracy as the cross-correlation scheme. The primary disadvantage of such a scheme is the need to use a lower intermediate frequency to improve the resolution of the output to an acceptable level.

A block diagram of a zero crossing phase detection system which could be used with the Lidar system is pictured in Figure 8. The first portion of the system consists of two zero crossing detectors which determine when the two signals pass through zero. The outputs of the detectors are fed to a gated counter with the reference signal's zero crossing initializing the counter and the distance signal's zero crossing terminating the counter. The output of the counter is then accumulated and averaged. Ultimately it is scaled by a multiplier circuit and displayed.

The primary advantage of the zero crossing phase detector is its comparative simplicity and also its inexpensiveness. It is far simpler than the cross correlation detector because it eliminates the multipliers, the A/D converters, and the PROM (lookup table). These components are replaced by a high speed clock and counter, and two zero crossing detectors. Because of this simplification much less signal processing is required, both analog and digital.

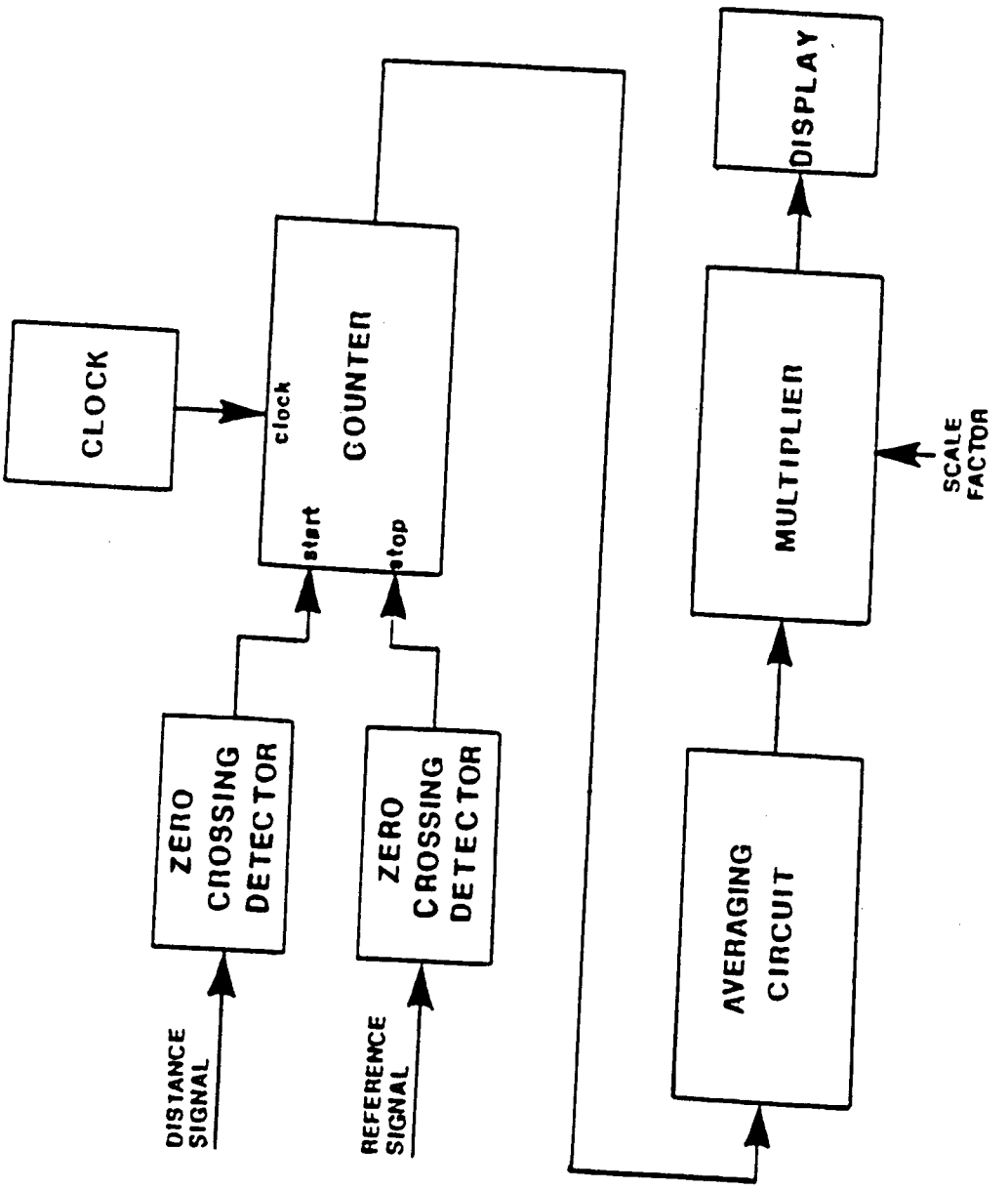

Figure 8 : Block diagram of Zero Crossing Phase Detector.

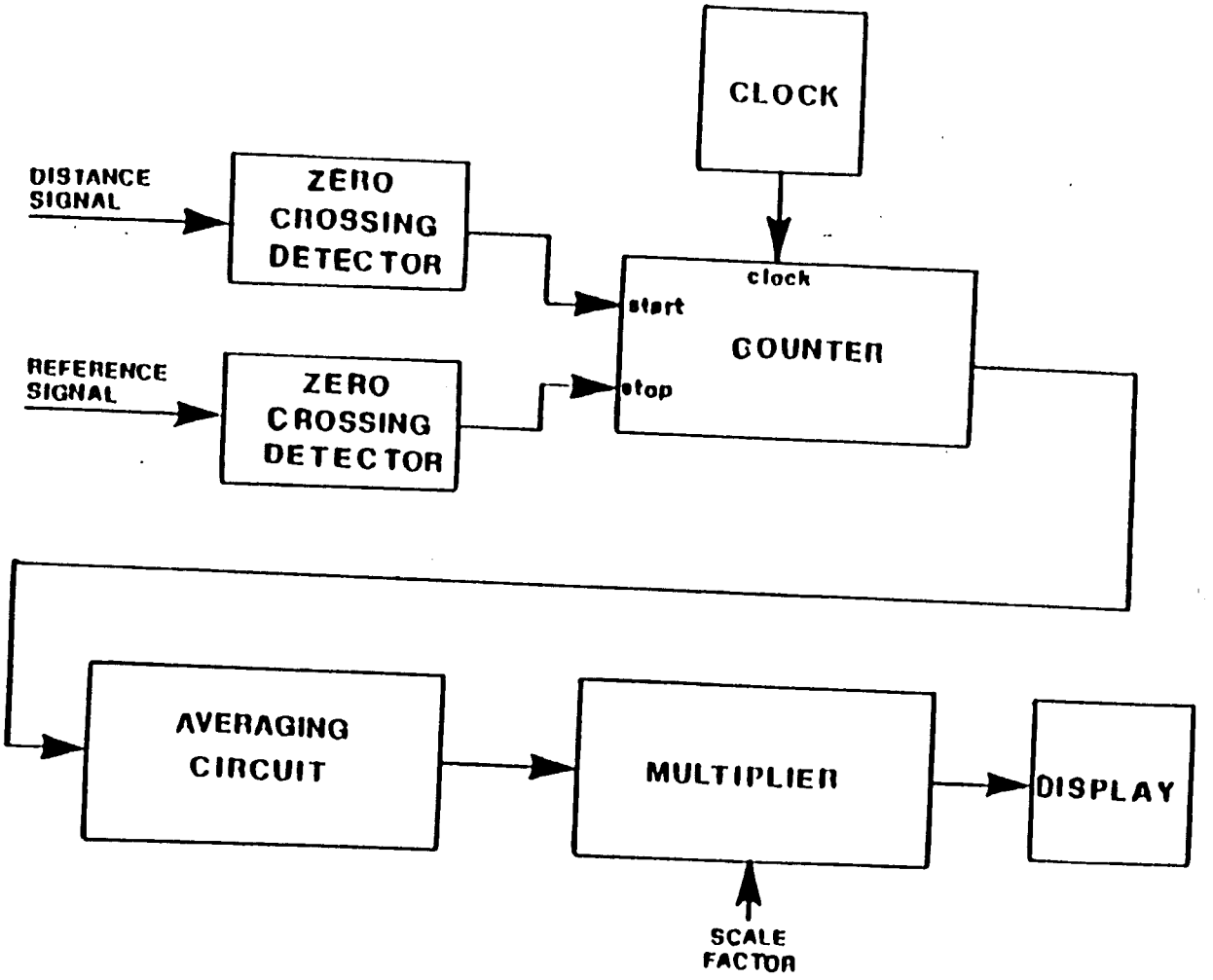

Figure 8 : Block diagram of Zero Crossing Phase Detector.

Another benefit of this scheme is that the phase detector measures the phase angle directly as opposed to the present system which measures the tangent of the phase angle and from that determines the phase angle. Thus the present technique necessitates the use of a lookup table and causes discontinuities in the distance result.

The primary disadvantage of the zero crossing detector is the need to utilize a relatively low IF in order to achieve acceptable resolution in the distance. If the clock frequency is 30 MHz, the resolution in the distance reading for the 420 kHz signal would be just:

$$(4) \qquad \Delta = \frac{\lambda_m}{2.} \frac{f_{signal}}{f_{counter}} = 0.53 \text{ mm}$$

Therefore the signal frequency must either be shifted by down conversion or a lower IF used. If an IF of 20 kHz was used, the resolution would become 0.025 mm.

From [1] Eq. (54) the signal variance for a zero crossing detector system would be:

$$(5) \qquad \sigma_\phi^2 = \frac{\sigma_s^2}{\hat{v}^2} = \frac{\overline{i^2}}{I_{rms}^2}$$

This is identical to the result that was obtained for the cross correlation detection scheme. The primary advantage of the cross correlation scheme over the zero crossing scheme is that it can be low pass filtered after the multiplier section and the standard

deviation reduced considerably. For the same results with the zero crossing scheme the signal must be filtered prior to the detector with a very narrow band pass filter or averaged after the counter. Although averaging after the counter is more complex, it causes no increase in integration time. When the present phase detector was constructed, a cross correlation scheme was chosen because it was thought to have better accuracy for a given signal to noise ratio. The accuracy of the two schemes turned out to be the same and thus for simplicity and better resolution in future systems zero crossing schemes will probably be utilized.

Direct Detection

A sizeable portion of the optical attenuation occurs during demodulation and detection of the signal. So if an alternative scheme was devised which eliminated the second modulator, the attenuation could be reduced drastically. This would require direct detection of the 4 GHz microwave signal. One possibility is the use of a fast photomultiplier tube capable of operating at or near 4 GHz. There are presently two devices which satisfy this requirement and might fit the application. The first is a tube manufactured by ITT which is a microchannel plate design primarily used for digital transmission. The second device is a static crossed field photomultiplier tube manufactured by Varian.

The signal to noise ratio for a Lidar system with direct 4 GHz

detection according to [1] Eq.(57) would be:

$$(6) \quad \frac{I_{RMS}^2}{i^2} = \frac{q_e \, A \, N_0 \, J_1^2(M\pi/2) \, \sin^2(B\pi)}{2 \, h \, r \, a^2 \, \Delta f[\, 1 - J_0(M\pi/2) \, \cos(B\pi)}$$

Therefore with direct detection the S/N ratio of the system would increase from the present 22 dB to 44 dB, assuming that there is no excess noise introduced into the photomultiplier tube. From [1] Eq.(58) the measurement error of such a system would be:

$$(7) \quad \Delta_D = \frac{c \, a \, (h\nu)^{\frac{1}{2}}}{1.414 \, f_m \, J_1(\pi/2)} \, (q_e \, A \, N_0)^{-\frac{1}{2}} (F)^{-\frac{1}{2}} (T)^{-\frac{1}{2}}$$

This relates to the error of the heterodyne system as follows:

$$(8) \quad \Delta_D = \frac{J_1(\ /2)}{1.414} \, (F)^{\frac{1}{2}} \, \Delta_H = 0.4 \, (F)^{\frac{1}{2}} \, \Delta_H$$

where F is the noise degradation factor due to incomplete modulation. A graph of F versus the modulation index is shown in Figure 9. With full modulation (i.e., M = 1), F equals unity, and $\Delta_D = 0.4 \, \Delta_H$, which means that all distance errors are reduced by a factor of 0.4 with the direct detection scheme. If the coefficient of modulation is less than unity the degradation factor ($F^{-\frac{1}{2}}$) will come into play and further increase the advantage of direct detection over the heterodyning technique. For the present system, M = 0.42 and from Figure 9 this gives F = 0.15. Therefore if direct detection was used in the present lab setup the standard deviation would be reduced by a factor of 0.25.

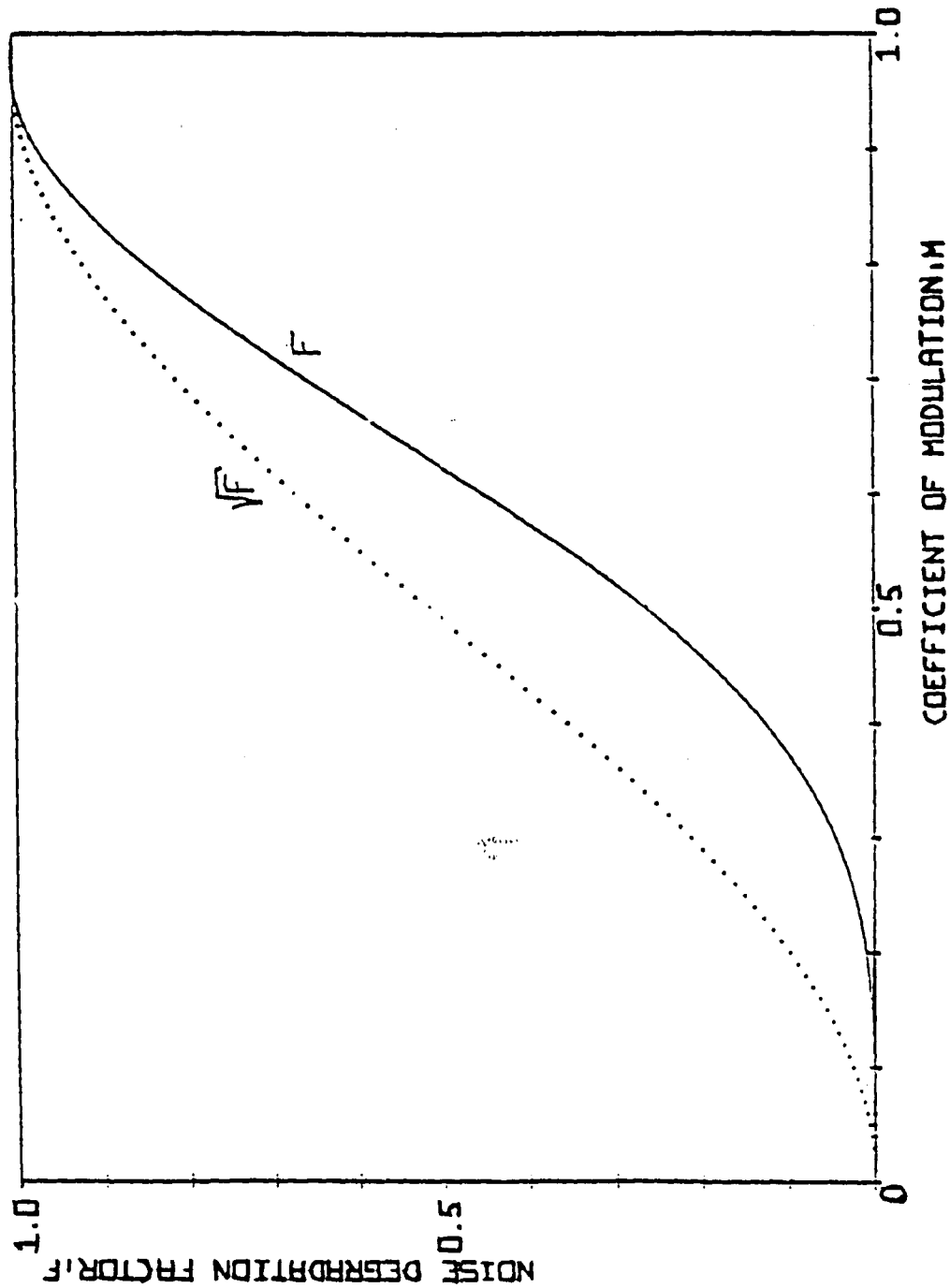

Figure 9 : Plot of F(noise degradation factor) versus M(modulation index).

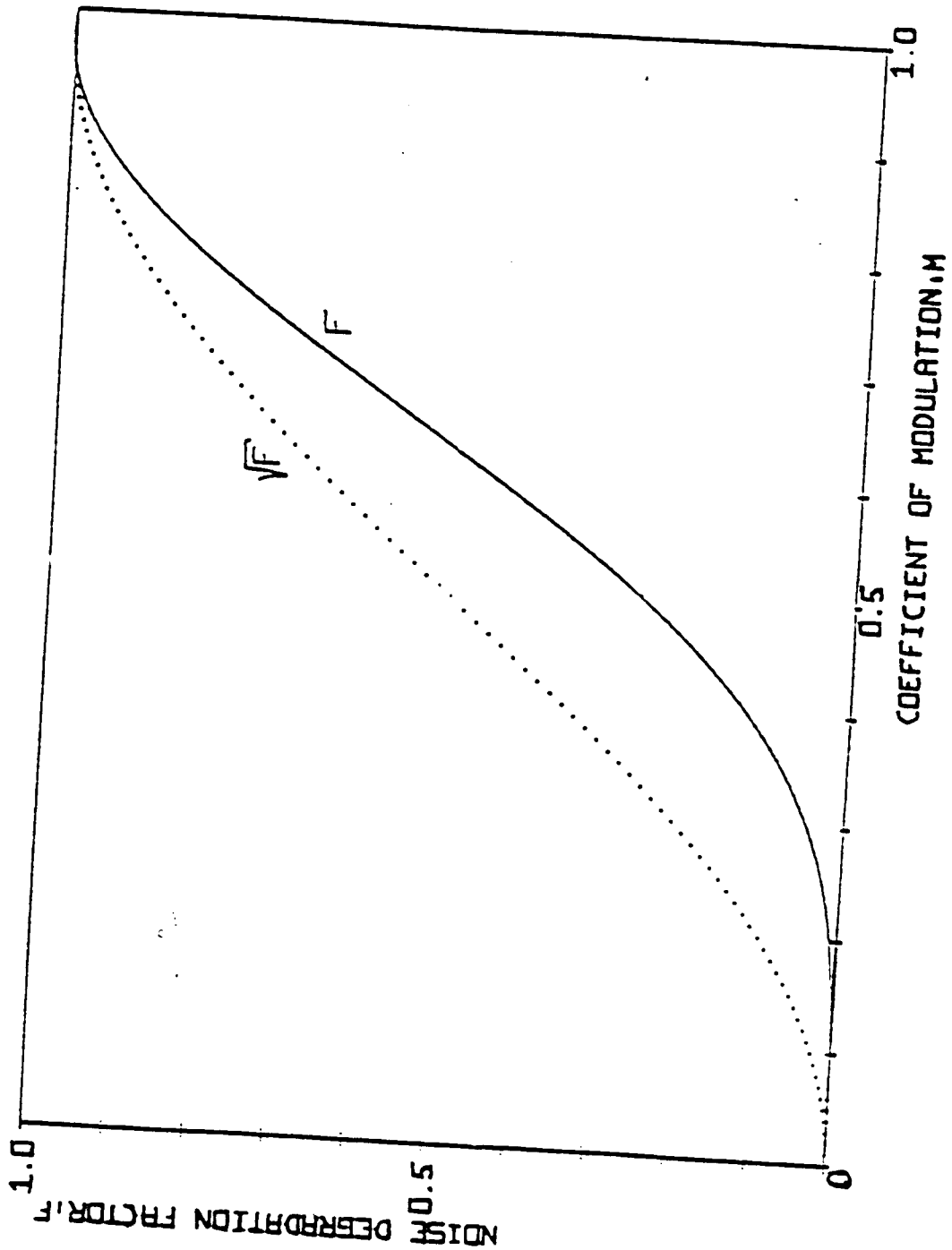

Figure 9 : Plot of F(noise degradation factor) versus M(modulation index).

Additional advantages of direct detection would be simplication of the receiver, elimination of the depth focus problem, and reduction of the roundtrip attenuation. The receiver is simplified becuase the number of components is reduced to just two, a telescope and a fast photomultiplier tube. Since the modulator is eliminated the modulator tuning problems are disposed of, and the critical alignment of the telescope and modulator crystal is eliminated. The depth focus problem inherent in the present setup is not a problem with the direct detection system because the light beam no longer has to thread through a tiny modulator crystal. Finally the roundtrip attenuation is reduced by about 8.5 to 9 dB which was attributed to the modulator and its associated components.

Fast Phototube Measurements

Microchannel plate photomultiplier tubes are available with a risetime of 150 picoseconds. This risetime would yield an acceptable response at 2.8 GHz. However, these tubes have not previously been used for CW detection and thus their frequency response is not characterized. Their pulse response, however, is well known because their primary use is in digital communication systems.

A microchannel plate photomultiplier tube model No. 4129 was borrowed from ITT in order to investigate its microwave properties and determine its suitability for incorporation into a Lidar system. As obtained from the manufacturer the tube has no capability for

easily connecting it to a coaxial 50 ohm line. Therefore an adapter was constructed in an attempt to match the output of the tube to a coaxial line in the best possible manner. The tube and its adapter setup are depicted in Figure 10. As shown in the figure, the adapter is a 4-inch cone. It was made from sheet brass, and the stepped inner core was constructed from varying sizes of brass tubing. One end of this fixture was attached to the photomultiplier tube with conductive copper tape and the other end was soldered to a coaxial N type connector. The output of the tube was ultimatley connected to a double stub tuner in series with a microwave biasing tee. The output of the tee was connected to a microammeter and a Hewlett Packard Signal Analyzer. The ammeter was used to monitor the average output current to avoid damaging the tube and the signal analyzer was used to detect the received microwave signal level.

The photomultiplier tube test setup is depicted in Figure 11. It consists of a 5 milliwatt linearily polarized He-Ne laser followed by a crystal modulator to generate a 2.8 Ghz intensity modulated light source. Additionally there was a variable attenuator to adjust the light level and a Babinet-Soleie compensator to adjust the working point of the modulator. After modulation, the beam was split with half going to a reference detector and the other half to the photomultiplier tube. The reference beam traveled through a scanning Fabry-Perot interferometer and was detected by a photo diode. The other half of the beam was spread with a zoom lens, deflected with an adjustable

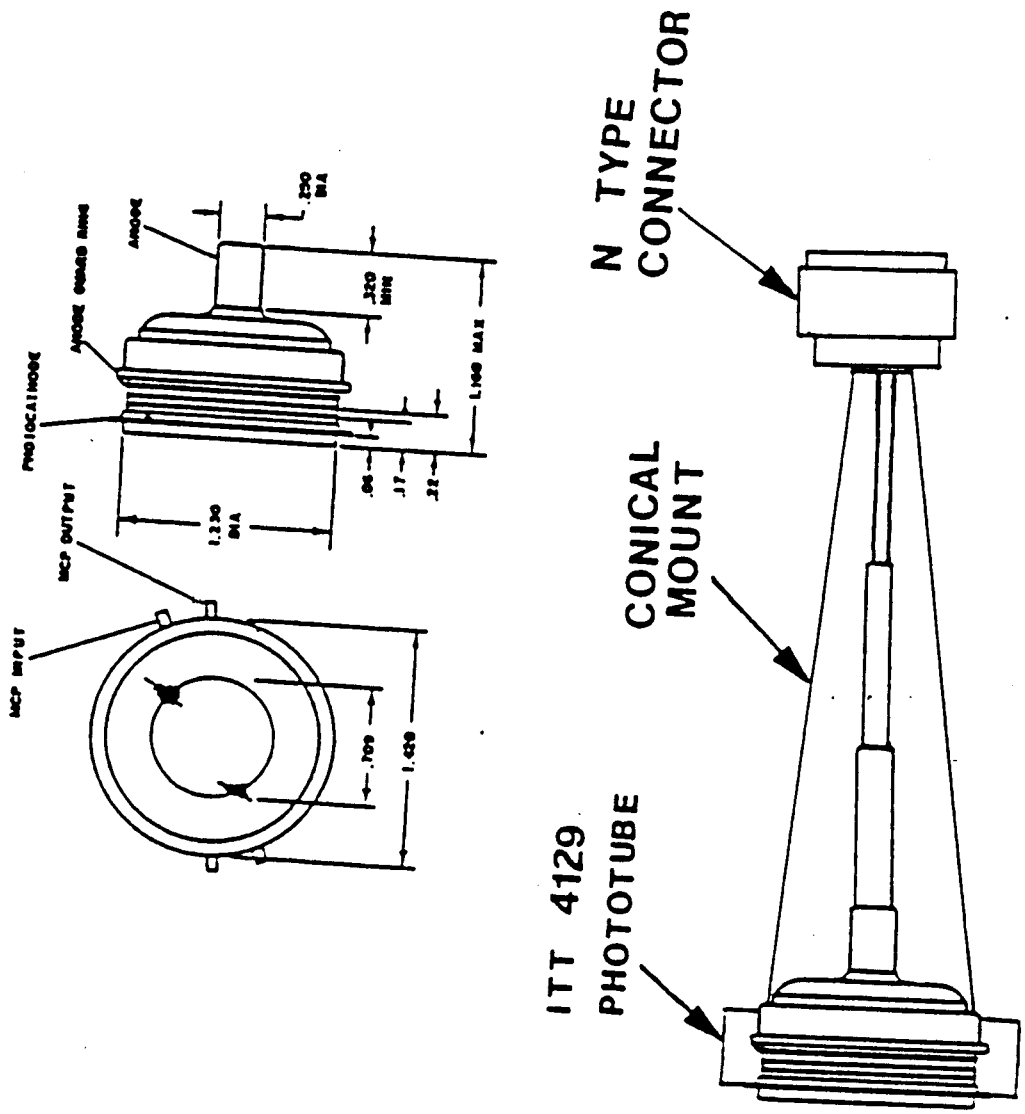

Figure 10 : Fast PM tube and Adapter.

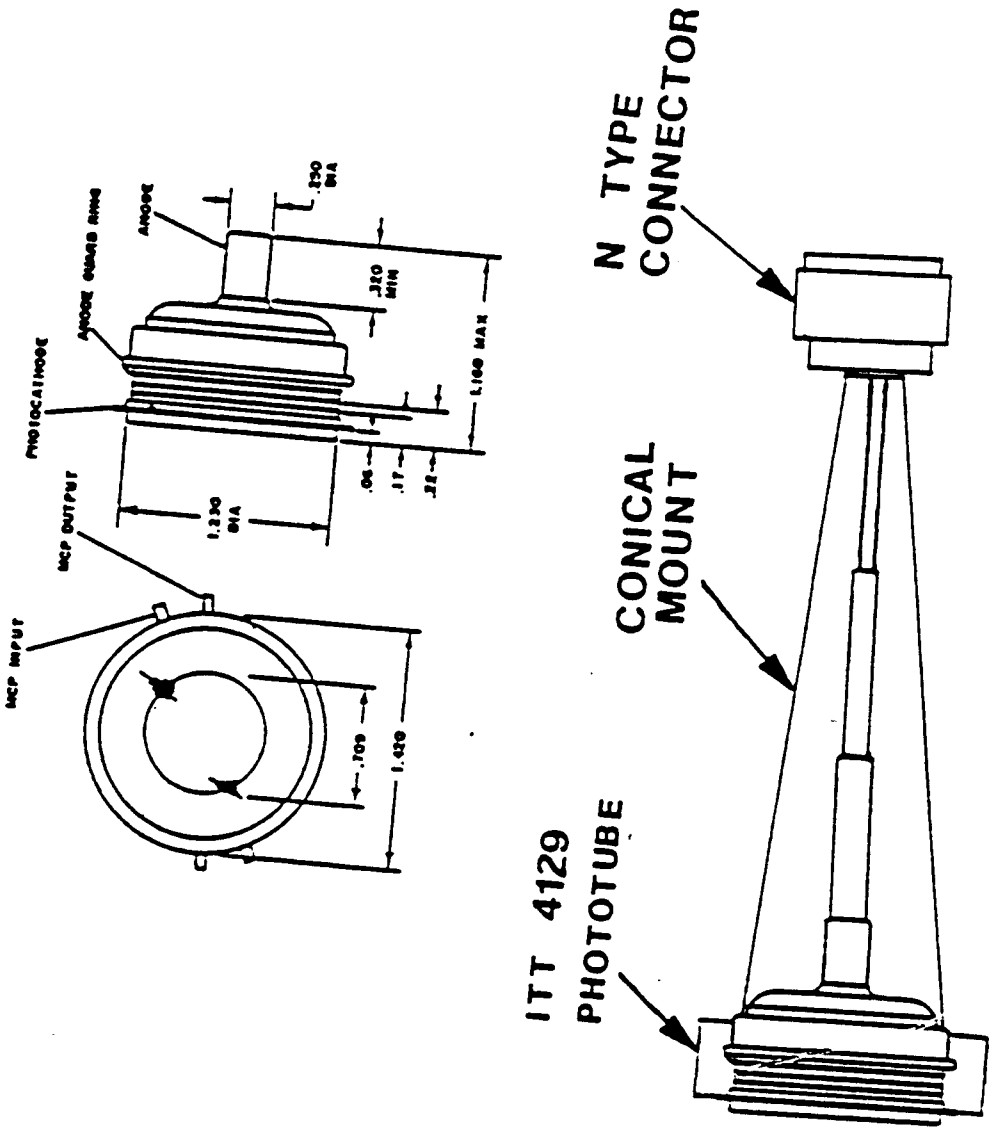

Figure 10 : Fast PM tube and Adapter.

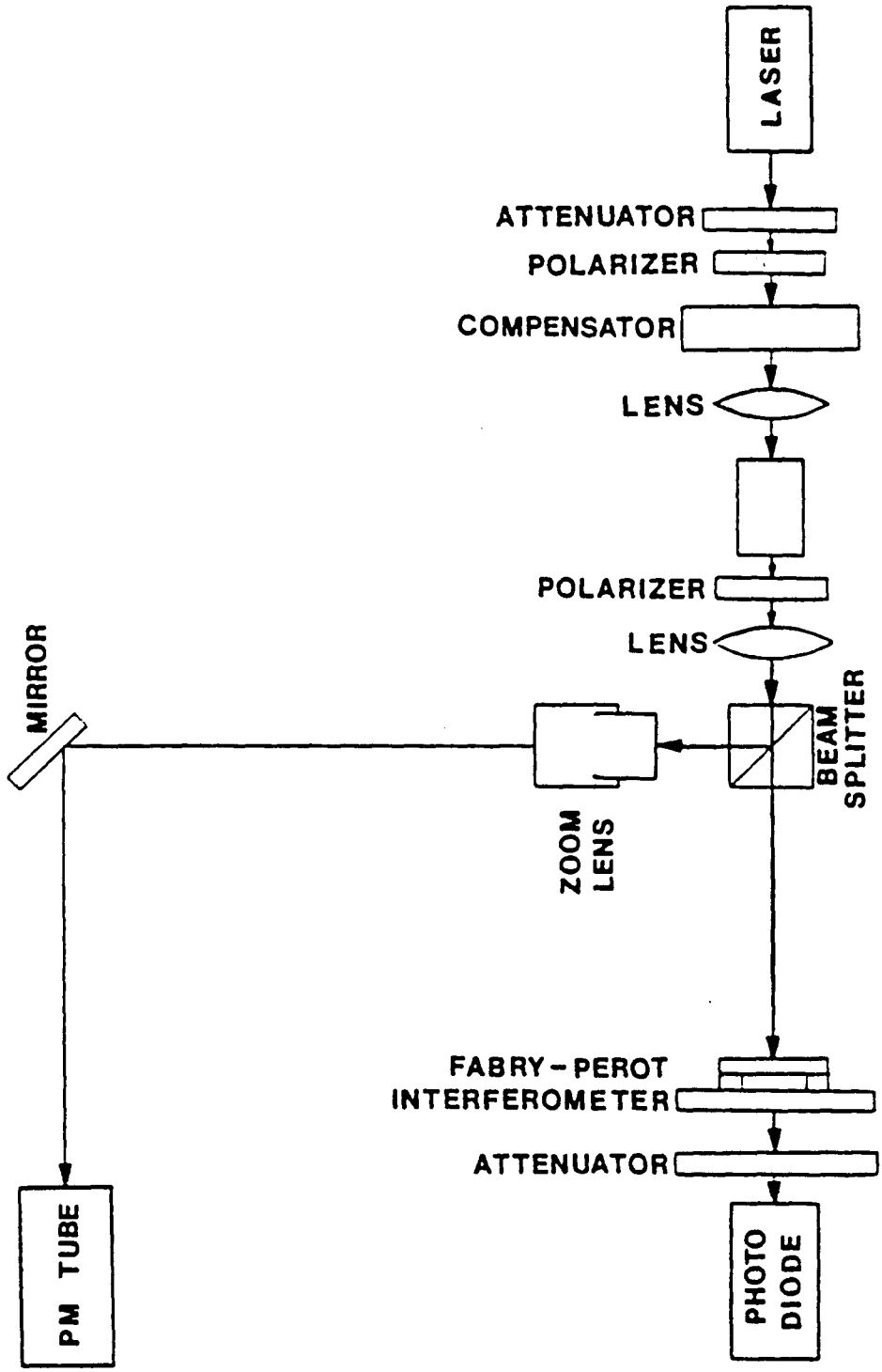

Figure 11 : Fast PM tube Laboratory Setup.

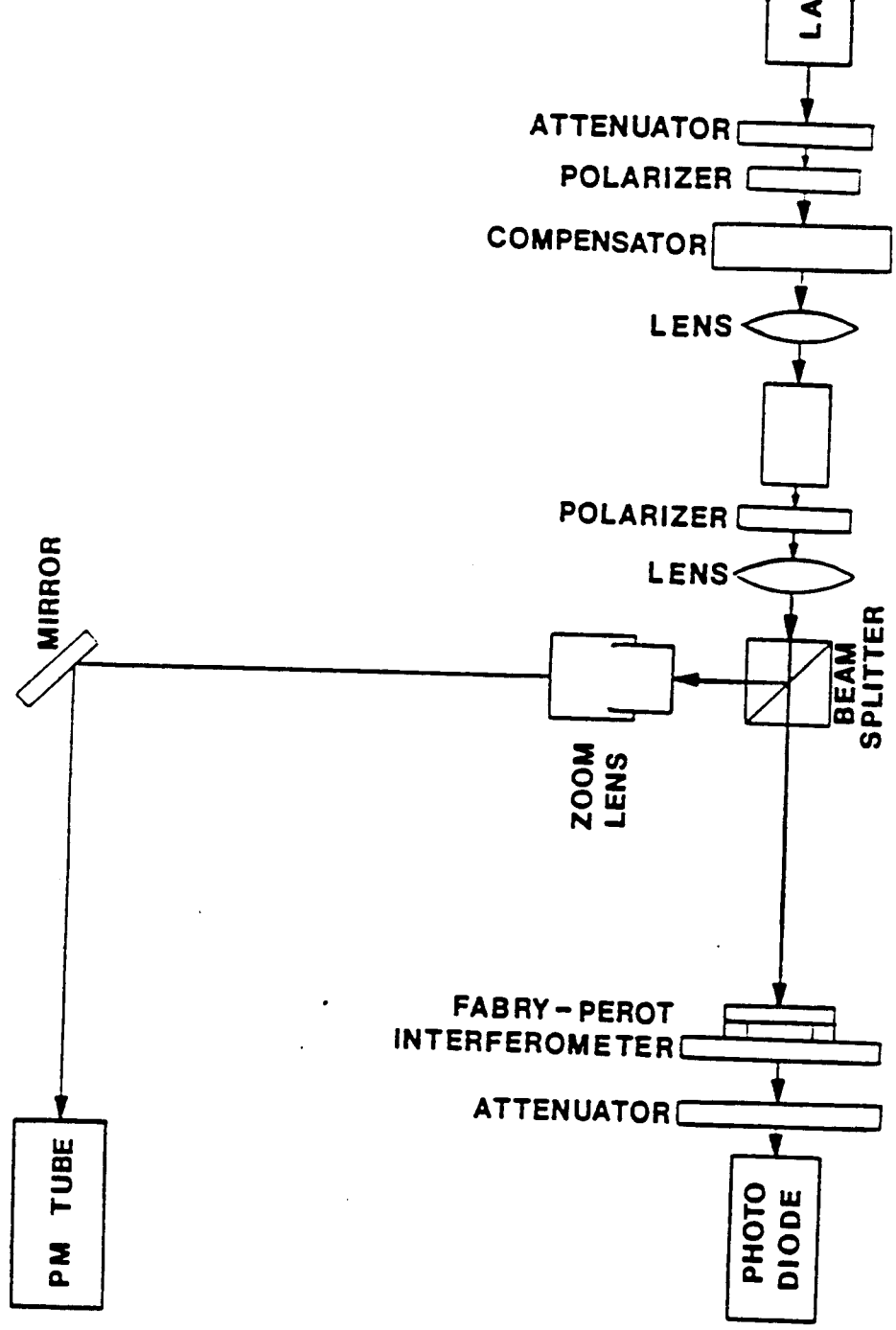

Figure 11 : Fast PM tube Laboratory Setup.

mirror, and ultimately illuminated the photocathode of the photomultiplier tube.

The photomultiplier tube was biased as shown in Figure 12. In order to supply the proper bias voltages, a voltage divider network was constructed with 40 2.7 megohm resistors which divided the 6000V supply voltage down into 150 V increments. The power was initially attached to the tube to give 150 V from the photocathode to the Micro Channel Plate (MCP) input, 1500 V across across the MCP's, and 300 V from the MCP output to the anode.

The first problem in measuring the performance of the tube was spurious (parasitic) transmission. This was eliminated by properly shielding the photomultiplier tube and the modulator, and by draping microwave attenuating foam rubber over susceptible areas of the setup. The spurious transmission was ultimately reduced to -105 dBm on the receiver. With that background level it is reasonable to assume that a -100 dBm signal would be observable on the receiver.

At low frequencies with 100% modulation and -105 dBm spurious transmission an output current, I_{RMS}, of 0.037 μA would have given 0.068 picowatts into 50 ohms or -100 dBm. Assuming that there is no frequency response degradation, the data in Table 2 gives the signal levels on the receiver versus the output current necessary to generate them.

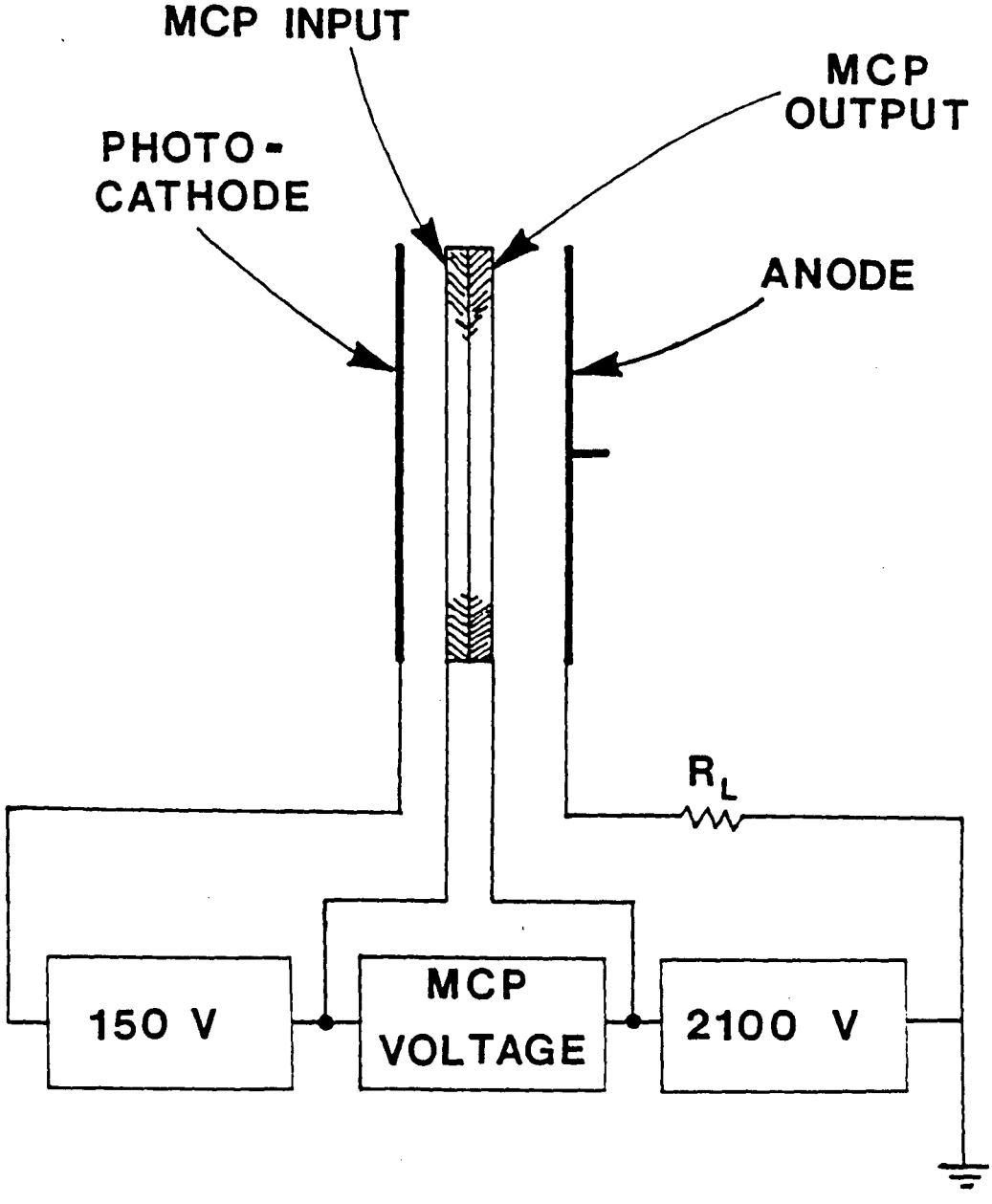

Figure 12 : Photomultiplier tube biasing.

After the spurious transmission was reduced, attempts were made to extract a signal from the tube. The double stub tuner was used in an attempt to better match the tube to the 50 ohm line. Next the bias voltage across the MCPs and the voltage from the MCP to the anode were increased to 2400 V and 2100 V respectively. No signal was observed. The light level was increased until the output current was 1.5 times the maximum allowed level of 0.1 A, and again no output was observed. Finally the modulation power was increased to seven watts, which gave nearly 100% modulation; no output was observed.

P_D(dB)	I_{RMS}(A)
-104	0.013
-102	0.025
-100	0.037
-98	0.050
-96	0.066
-94	0.086
-93	0.097

Table 2 : List of signal level readings vs. current needed to generate them.

The tube would have had to put out only .037 A or 52% of its maximum output to give a -100 dBm reading. With seven watts modulating power we were getting near 100% modulation, and we were overdriving the tube by 50%. This means that if the tubes degradation factor at 2.8 GHz was more than 0.35 we would certainly have observed an output.

It was decided that the ITT tube is unsuitable for CW-microwave use primarily because of its extremely low output current. Its maximum average output current is 0.1 μA which yields an RMS output current of 0.071 μA and into 50 ohms this gives -91.5 dBm. To detect that level requires sophisticated amplifiers and signal analyzers. Also at that output level the device is highly sensitive to spurious transmission. An additional problem with the tube is that it is not well matched for microwave use. Presently, however, no microchannel plate phototube with higher output current or better microwave matching is available.

An alternative to this phototube would have been the static crossed field photomultiplier tube previously manufactured by Varian. It had several advantages over microchannel plate photomultiplier tubes and the problems inherent in those tube are eliminated. First the Varian tube had a maximum average output current of 50mA which is 500 times greater than the ITT microchannel plate phototube. This means that the maximum average power output is -39 dBm. Also the Varian tube had a 50 ohm coaxial output which makes it much more useful for microwave frequencies. The Varian tubes, however, are presently not being manufactured.

Solid State Detectors

An alternative to photomultiplier tubes for direct detection is the photodiode. Two types of photodiodes are available which may

operate fast enough for this application. They are PIN diodes and avalanche photodiodes (APD). Generally photodiodes are characterized by three properties: spectral response, rise-time, and noise. In most photodiodes the quantum efficiency and rise-time are sufficient and the problem problem area is noise, because optical detection generally deals with very weak signals. Whereas the photomultiplier tubes were basically quantum noise limited, these devices introduce excess noise, particularly the APD. Noise arises from basically four different sources: quantum noise in the optical signal, quantum noise in the detector, excess noise generated by avalanche gain in the detector, and noise in the amplifier. Therefore in so far as applying one of these devices to a Lidar system is concerned, three primary factors must be considered: first, is the device fast enough, second, does it introduce too much excess noise, and third does it have enough output?

The operation of solid state photodiodes depends on the existence of a depleted semiconductor region with a high electric field serving to separate photo-excited electron-hole pairs. High speed photodiodes generally operate at large reverse biases into relatively low impedences. The large bias has the effect of reducing the carrier transit time and reducing the junction capacitance. The low impedence load allows the photoexcited carriers to induce a current in the load circuit while they are traversing the high field region of the diode.

The operation of a reverse biased PIN photodiode with a load resistance R_L is shown in Figure 13. In this device, the incident light, which is not reflected off the surface, penetrates some depth into the surface before being absorbed. The photon absorption generates electron hole pairs(EHPs). EHPs generated in the high field region are quickly collected. However, when EHPs are generated in the bulk material, the minority carriers must diffuse into the high field region and then be collected. Generally minority carriers which are generated within a diffusion length of the junction will diffuse into the high field region.

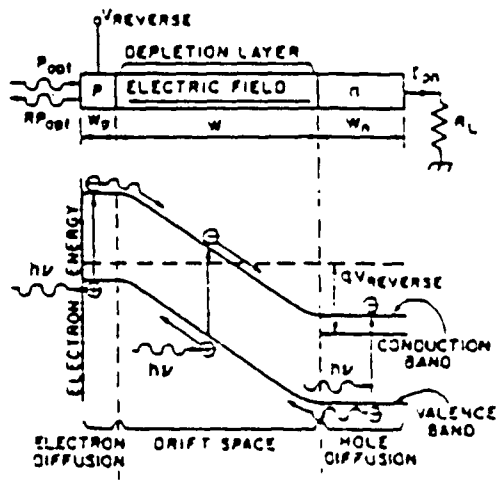

Figure 13 : Operation of a reverse bisaed PIN diode.

The minority carrier diffusion is a slow process and it limits the frequency bandwidth of the device. For this reason, high speed photodetectors are designed in such a way as to have most of the EHPs generated in the high field region. This reduces the transit

time considerably because at sufficiently high biases the carriers are collected at scattering limited velocities rather than diffusion velocities. In this fashion the operating bandwidths of the devices can be dramatically increased. In the PIN diodes a trade-off is often made between the quantum efficiency and transit time. In order to have as small a transit time as possible the high field region must be short. Whereas to have a high quantum efficiency the high field region must be long to allow a greater percentage of the photons to be absorbed.

In an ideal photodiode, every incident photon will create an EHP and at a wavelength of one micron the responsivity is about 0.8 Amperes per watt. Thus with typical received optical signals in the nanowatt range the output current of such devices will be a few nanoamperes. These small currents are extremely difficult to process without adding excessive amplifier noise. Therefore a mechanism is needed to increase the output current prior to amplification, and this mechanism is avalanche gain.

Avalanche photodiodes are specially constructed devices which combine optical signal detection with internal photocurrent amplification. A schematic diagram of an APD is shown in Figure 14. The avalance gain occurs in an APD when carriers build up sufficient enrgy by moving through the high-field region to release additional E/H pairs by impact ionization. Impact ionization is an inelastic collision in which energy is given up by a photoexcited carrier to

move an electron from the valence band to the conduction band. Impact ionization is characterized by the ionization rates α , for electrons and β,for holes. The ionization rates indicate the number

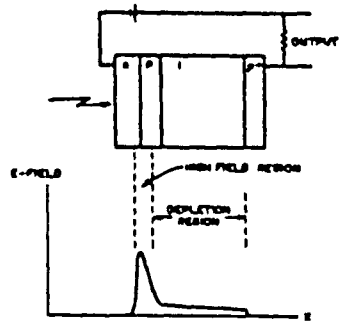

Figure 14 : Schematic of an Avalanche Photodiode.

of secondary carriers created by a single initiating carrier traveling one cm. in an electric field of strength E. Avalanche gain has feedback associated with it as shown in Figure 15. Each multiplication creates an EHP. If the initiating carrier is an

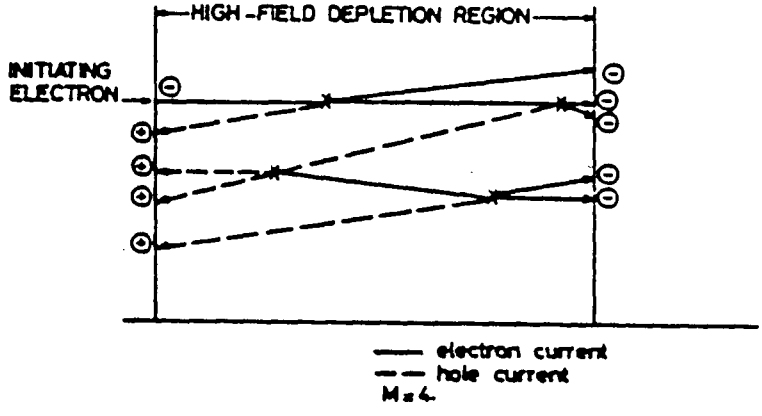

Figure 15 : Avalanche Gain Feedback Process.

electron as illustrated in the figure, then the holes created by the collision are the feedback carriers. These holes are accelerated in the direction from which the electron entered the junction; and as they traverse the the depletion region they may undergo ionizing collisions. These collisions will generate more electrons which will be swept in the opposite direction. This is the process which leads to avalanche.

In avalanche photodiodes, response time is a critical parameter. As was true for the PIN diode, the APDs speed is initially limited by diffusion time. Thus these devices are designed so that the carriers are generated in the high field depletion region and not in the bulk of the material. Ultimately, the device speed is limited by the avalanche gain itself. The feedback process described above is the cause of the delay, and the delay is inversely proportional to the device gain because if the device has a large gain that implies a large amount of feedback. Conversely if the device has a small gain, fewer ionizing collisions will occur and the delay will be shorter. This implies a tradeoff between response time and gain. Presently avalanche diodes are available with gain bandwidth products on the order of 100 GHz.

Noise in Solid State Detectors

The sensitivity of a photodiode is determined by two factors: the quantum efficiency and the noise. Noise comes from two sources

the detector and the pre-amplifier. The detector noise is from three sources: quantum noise in the received signal, shot noise in the detector, and excess noise caused by photomultiplication within the device. The signal to noise ratio after the pre-amp can be expressed as : [3]

$$(9) \qquad \frac{S}{N} = \frac{\text{signal power}}{\text{(shot noise power) + (amplifier noise power)}}$$

The signal power is determined by squaring the photocurrent and is expressed as :

$$(10) \qquad \overline{i_s^2} = \tfrac{1}{2} [\, 2 N_{RMS} S \,]^2$$

where N_{RMS} is the RMS value of N(t), which is the sinusoidally varying light power; and S is the sensitivity of the detector and is defined as:

$$(11) \qquad S = \eta q / h\omega$$

The optical signal contains quantum noise and if a semiconductor laser is the light source, the noise is :

$$(12) \qquad \overline{i_{ns}^2} = 4 e [\, \bar{N} S \,] B$$

The quantum noise in the photodiode is proportional to the dark current and is :

$$(13) \qquad \overline{i_{nd}^2} = 2 e i_d B$$

The noise power in the amplifier is a function of the effective noise temperature of the amplifier. It is given by :

$$(14) \qquad \overline{i_{na}^2} = [(4 k T_{eff})/R_L] B$$

Noise may be further minimized if R_L is chosen as large as possible

without adversely effecting the bandwidth. The maximum value of R_L which will not degrade the frequency response is $\frac{1}{2 \pi BC}$. If the detector is biased near breakdown such that avalanche gain occurs, the signal power and shot noise power will increase but the amplifier noise will not. The amplifier noise dominates the other noise terms and thus the maximum useful avalanche gain is that amount which increases the shot noise power up to the level of the amplifier noise power. Combining the previous equations and including the multiplication factor for avalanche gain, results in the output S/N ratio being :

$$(15) \quad \frac{S}{N} = \frac{2 \left[N_{RMS}\ S \right]^2 M^2}{\left[\left[2ei_d + 4e \left(\overline{N}\ S \right) \right] M^2 F(M) + 4k\ T_{eff} / R_L \right] B}$$

where : M is the multiplication factor for avalanche gain

and

F(M) is the excess noise factor which depends on the impact ionization rates in the detector.

Excess noise in avalanche gain is directly related to the amount of feedback and can be expressed in terms of the impact ionization rates α and β. As and become more dissimilar only the carrier with the larger ionization rate contributes to impact ionization, and the excess noise factor decreases tending toward its lower limit of one. If $\alpha = \beta$, the excess noise factor is at its maximum of M the multiplication gain. The actual dependance of avalanche gain can be expressed as : [4]

$$(16) \quad F = M \left[1 - (1-k) \left[(M-1)/M \right]^2 \right]$$

for the case where electrons have the higher impact ionization rate and $k = \beta / \alpha < 1$. A similar expression exists for hole dominated avalanche gain.

Semiconductor Laser Diodes

Another modification to the Lidar system which could improve the S/N ratio of the system would be direct modulation of the laser beam. This would involve eliminating the He-Ne laser and the crystal modulator and replacing them with a single mode CW semiconductor laser. Two factors must be considered to determine the suitability of these devices for a Lidar system: these are their focusability and modulation characteristics.

All CW injection lasers consist of four basic epitaxial layers grown on a substrate as shown in Figure 16. The shaded layer in the figure is the active region where the light is generated. It is sandwiched between two layers of a large bandgap, low refractive index material which serves to contain the light beam, and confine the injected carriers for recombination within the active layer. By making the active layer sufficiently thin the device will be single mode in the vertical direction.

Lasers designed for CW operation are stripe-geometry lasers. In a stripe-geometry laser, the stripe is formed by isolating the elctrical contact region through which the current flows. The amount of current spread in the active layer determines the lateral

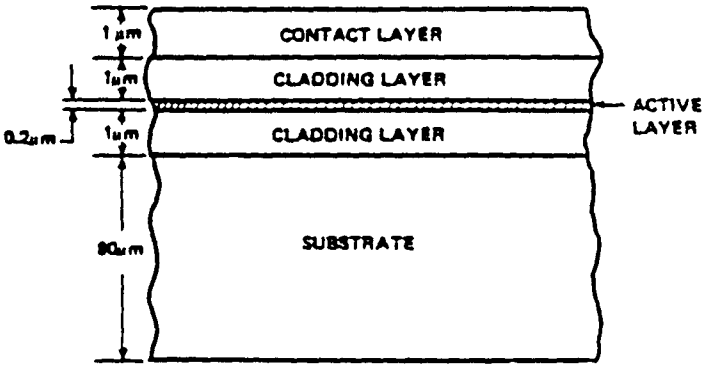

Figure 16 : CW injection laser structure.

dimension of the waveguide. The current spread is a function of the current and thus the waveguide expands and contracts during modulation, causing non-linearities and lateral mode instability. One method of controling the current spread which has been particularly effective is proton implantation. In this technique protons are implanted in the upper two epitaxial layers in the region surrounding the contact stripe. This causes the implanted areas of the material to become highly resistive, and the current spread is virtually eliminated. With this technique the lateral beam width can be precisely controlled and a stable mode of operation obtained in the lateral direction.

The mode structure in the vertical and lateral diredtions are not symmetrical. In the vertical direction the light is guided by

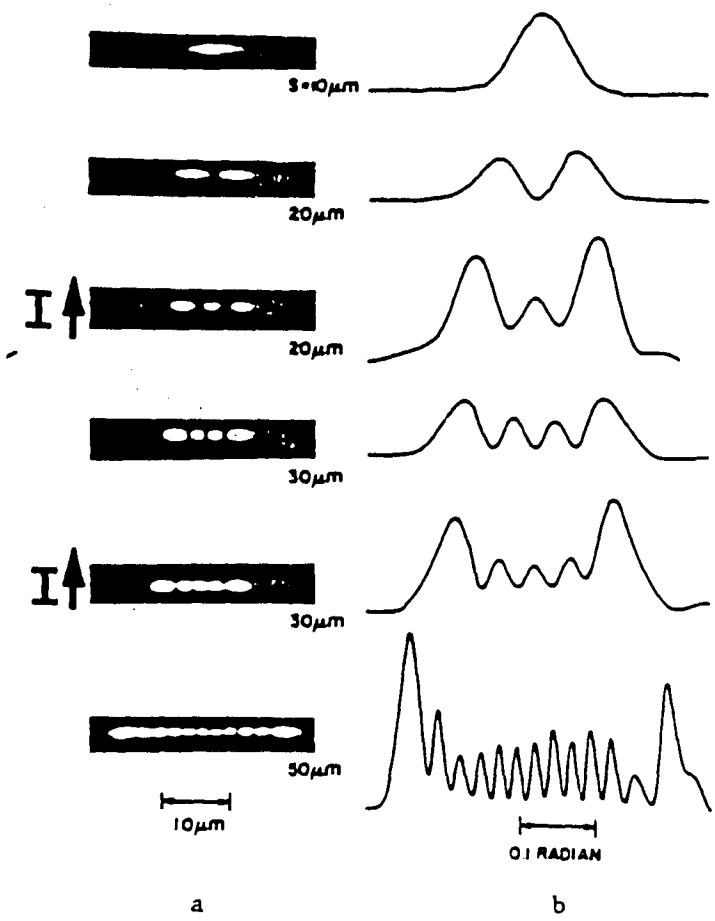

Figure 17 : Emmision patterns of stripe-geometry lasers.

a) near-field, and b) far-field.

the cladding meterial. This mode is highly stable and remains so up to very high optical power levels. However, the mode structure in the lateral direction is determined by the stripe width. As the stripe width is increased higher order modes become visible. This is illustrated in the emmission patterns, near-field and far-field, of four stripe-geometry lasers in Figure 17. As shown in the figure for S = 20 and 30 μm, the mode order increased as current increased, illustrating the instability of stripe-geometry lasers in the lateral direction. An increase in power can cause the laser to switch from single mode operation to multimode operation in the lateral direction.

Laser Diode Measurements

A laser diode Model No. SCW-30 was purchased from Laser Diode Laboratories. It is a single mode CW laser with a maximum power output of 7 mW at 8327 Å. An I-V curve and Power-Current curve for the device are shown in Figure 18. Investigations were done on the operation of the diode to determine its suitability for incorporation into a Lidar system. The two parameters which determine the suitability are : the diodes ability to be focused to a small spot at about 3 meters distance, and the modulation characteristics of the diode. Because the laser emits in the infrared portion of the electromagnetic spectrum, observations of the beam were made with an IR Find-R-Scope. From the initial observations of the laser spot, it was determined that the laser was

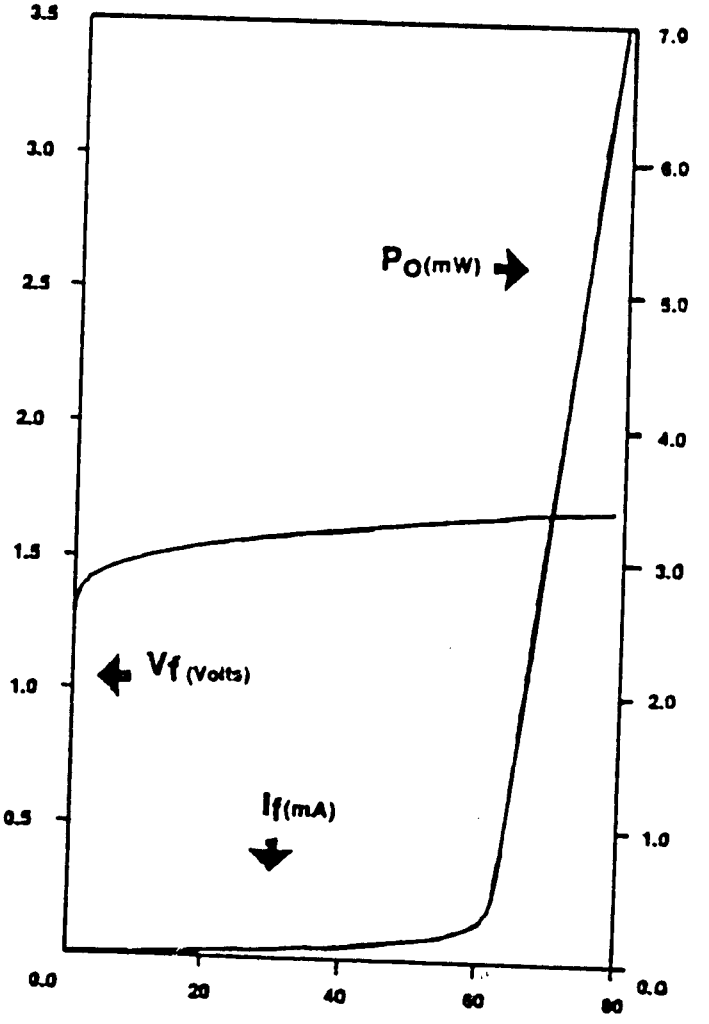

Figure 18 : Operating characteristics of SCW-30 laser

only single mode in the vertical direction and in the lateral direction was dual mode.

The diode was packaged in a 50 ohm coaxial housing with a threaded end, as depicted in Figure 19. A cylindrical mount shown in Figure 20 was constructed to hold the diode and also act as a heat sink to avoid thermal damage to the diode. The mount was threaded on one end to hold the diode and an SMA connector was attached to the other end. The cylinder was then mounted inside a cylindrical ring with setscrews to provide 360^{o} rotation of the laser for ease of positioning while taking measurements.

The first measurement done on the diode was the determination of the beam characteristics. To do this required a calibrated moveable detector to measure the beam width at various distances from the diode. The detector consisted of a photodiode with a pinhole mounted in front of it. The assembly was then mounted on a calibrated X-Y stage with a flexible shaft attached to to the X positioning micrometer. The other end of the flexible shaft was connected to a potentiometer, which was used to generate a voltage proportional to the position of the stage. This voltage was used to drive the X input of an X-Y plotter, and the Y input was driven with the output of the photodiode. In this manner, plots were taken of the beams cross-section.

Figure 19 : Case configuration of SCW-30 laser.

Figure 19 : Case configuration of SCW-30 laser.

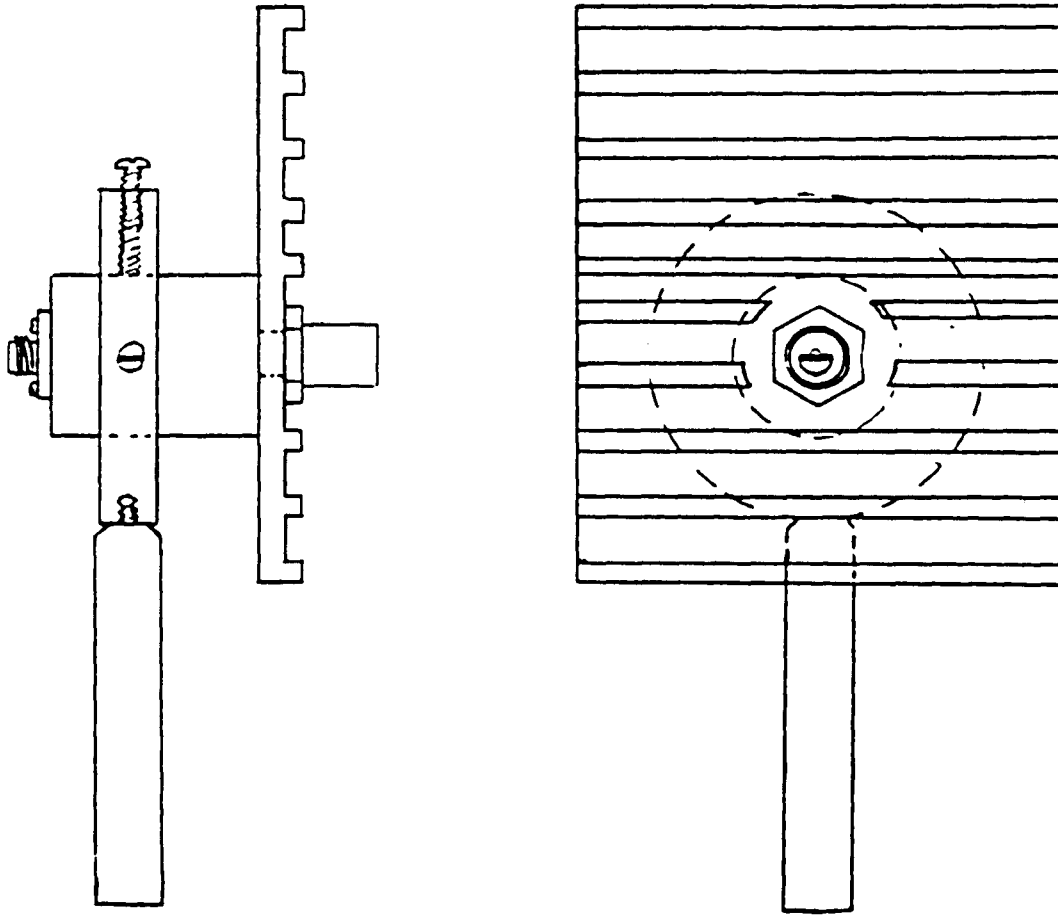

Figure 20 : Laser diode mount.

In order to characterize the beam, plots were taken in the horizontal and vertical axes of the laser. Because the beam had two lateral modes, two plots were taken in the vertical axis, each peaked on one of the lateral modes. The beam widths were measured at four distances 20 cm, 40 cm, 60 cm, and 80 cm, and thus twelve plots were taken in all. The plots are presented in Figure 21. From these plots, the vertical and lateral beam widths were measured and are listed in Table 3. By approximating the gaussian beam

Measurement Distance (cm)	Beam Widths (cm)			
	Lateral	Vertical		
		1st	2nd	Average
20	0.105	0.030	0.023	0.026
40	0.285	0.064	0.053	0.058
60	0.420	0.087	0.078	0.083
80	0.578	0.120	0.112	0.116

Table 3 : Lateral and vertical beam widths of the laser diode.

spread with a linear approximation, the divergence angles of the beam can be determined from simple trigonometry. This ammounts to the following :

$$(17) \quad \text{Angle} = 2 \times \arctan[(\text{Beam Width}_{80} - \text{Beam Width}_{40})/(2\times 40\text{cm})]$$

Utilizing the formula results in a lateral divergence angle of 0.42^{o} and a vertical divergence angle of 0.09^{o}.

The first attempt at focusing the beam was done without trying to correct for the elliptical asymetry of the beam. The

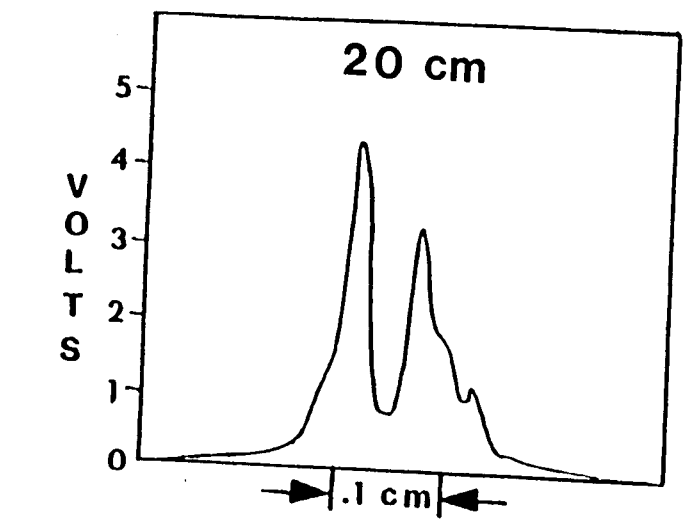

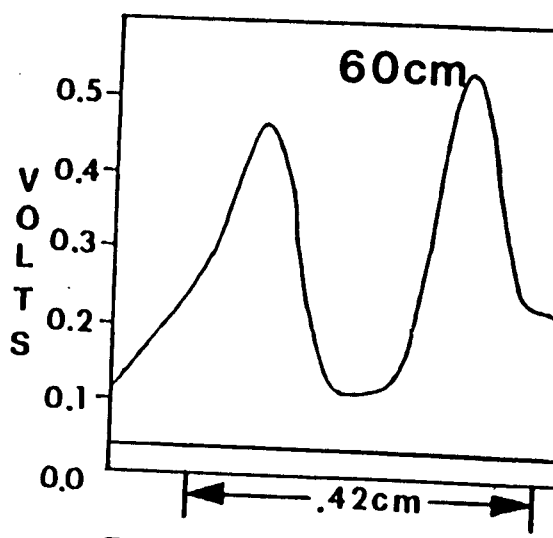

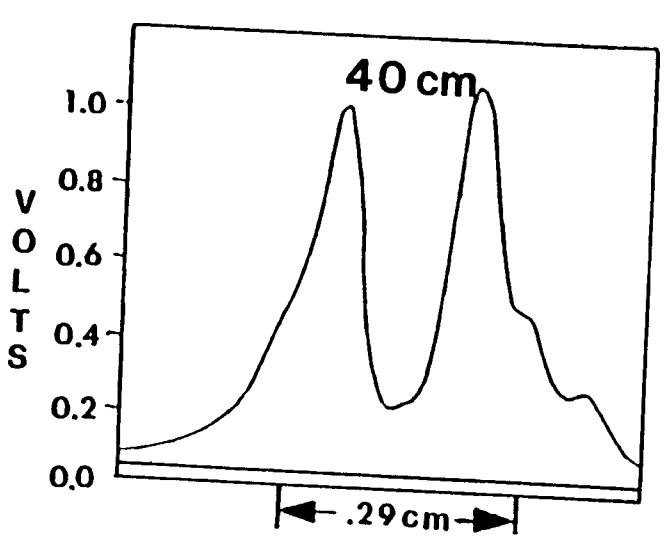

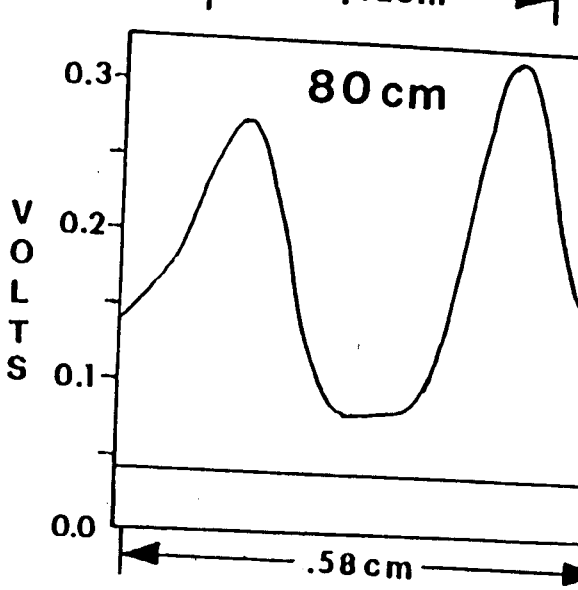

Figure 21a : Lateral beam scans.

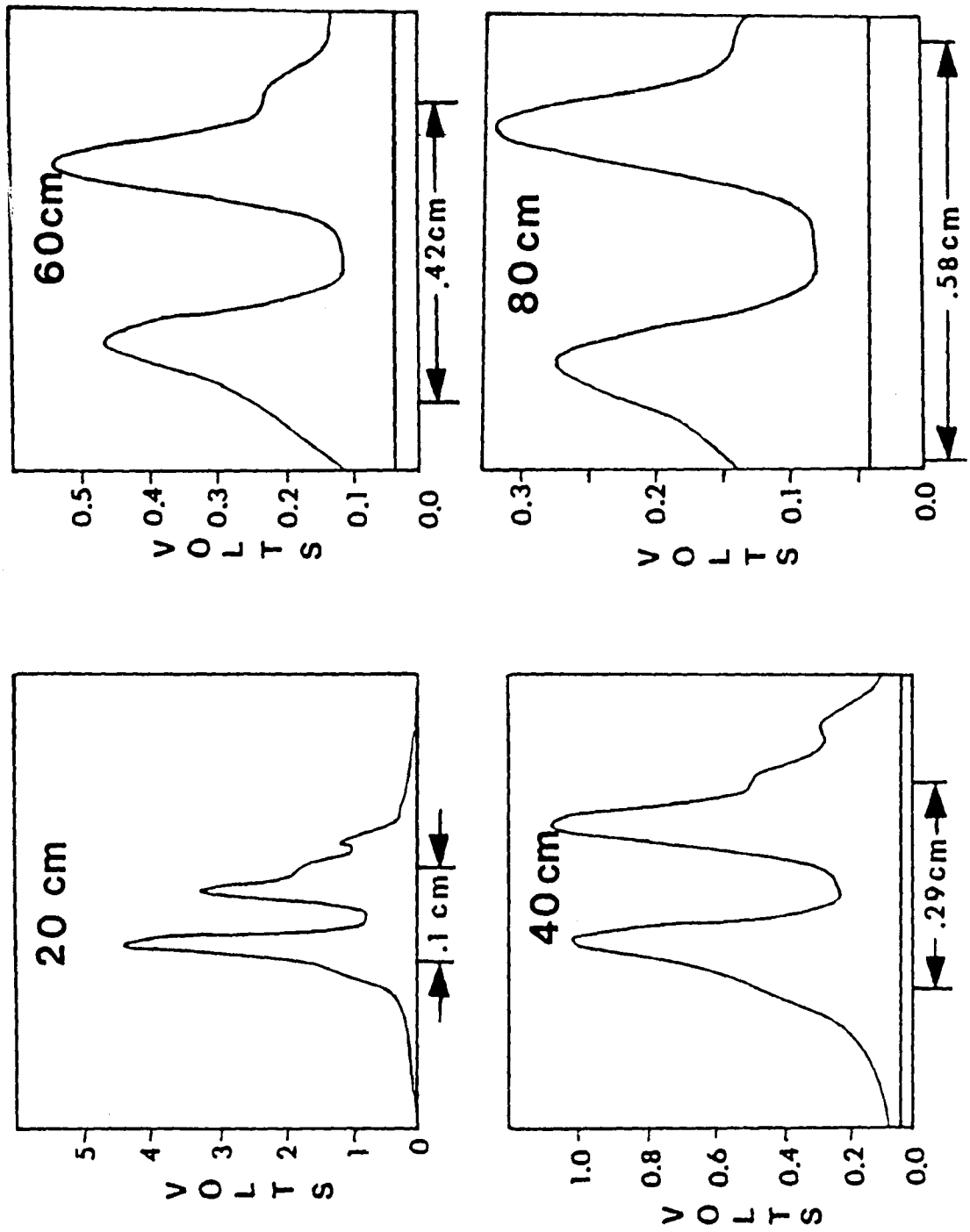

Figure 21a : Lateral beam scans.

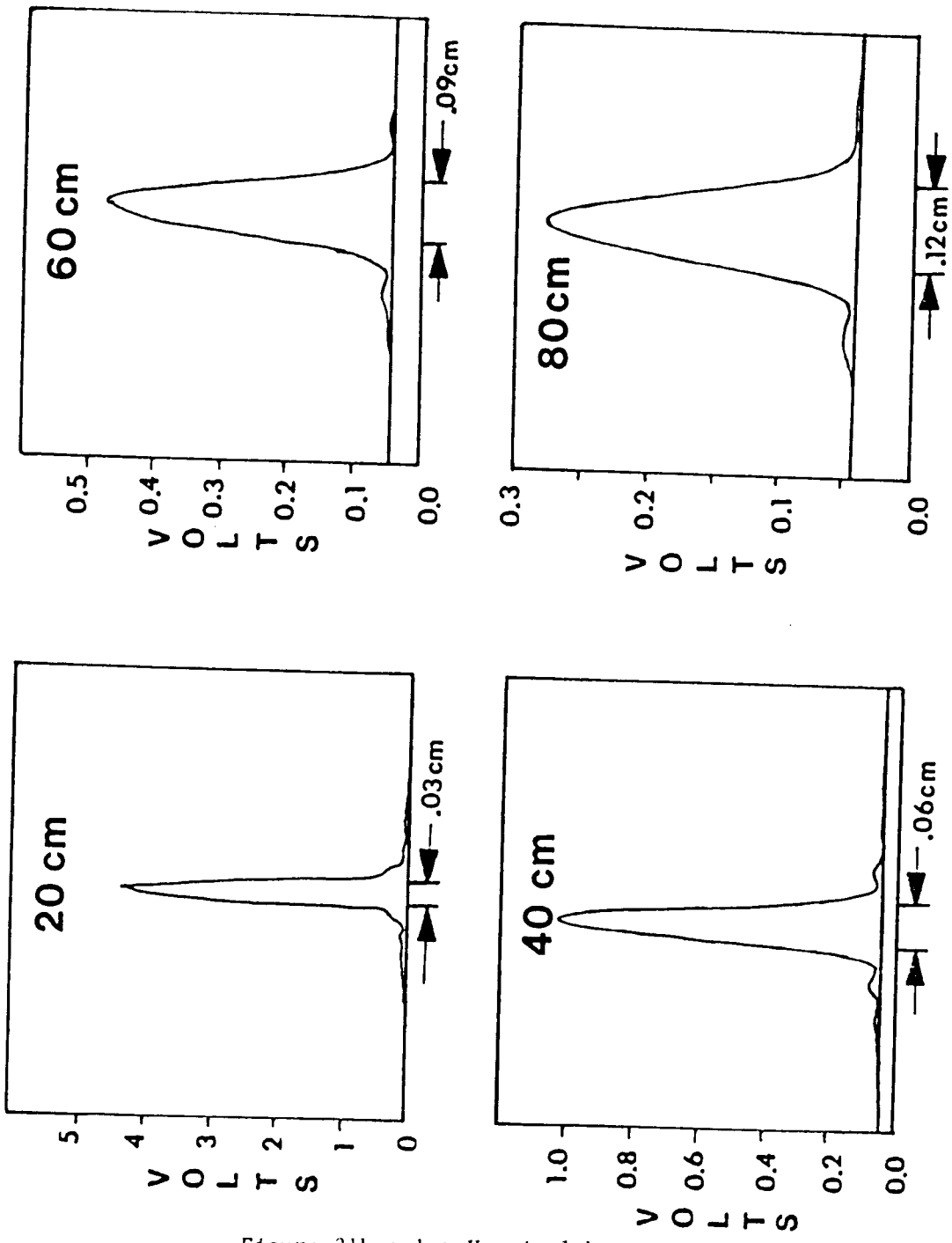

Figure 21b : 1st Vertical beam scans.

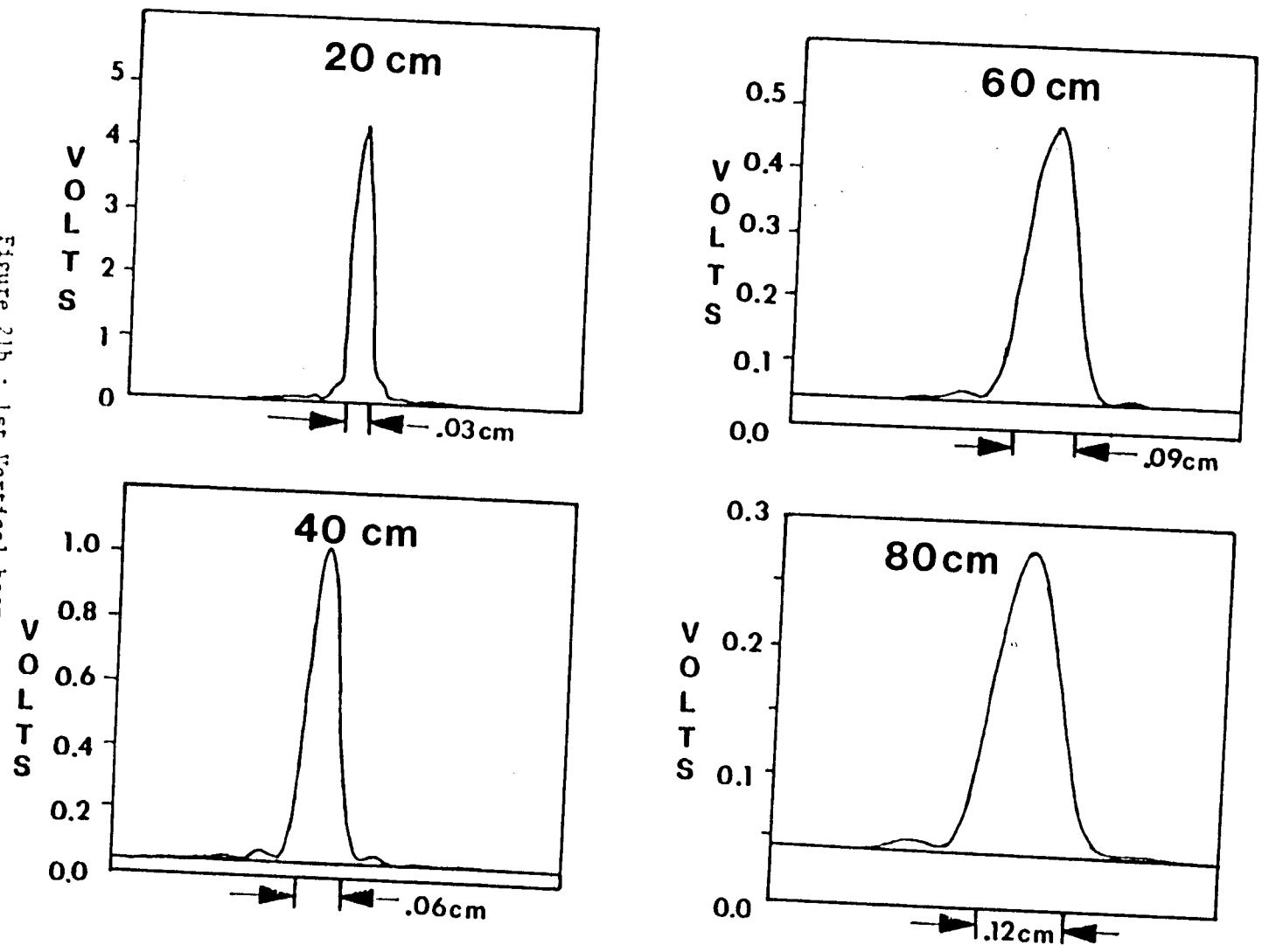

Figure 21b : 1st Vertical beam scans.

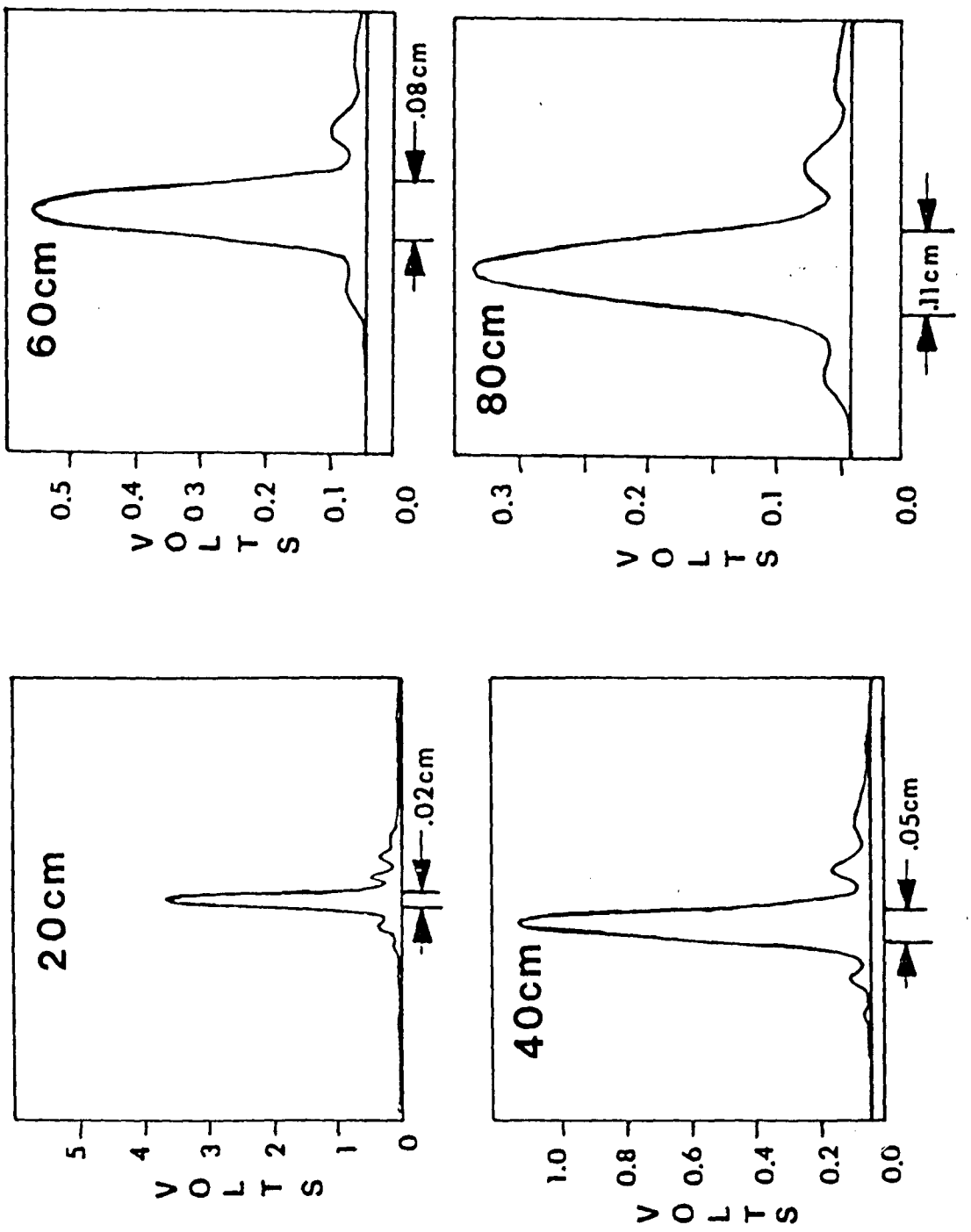

Figure 21c : 2nd Vertical beam scans.

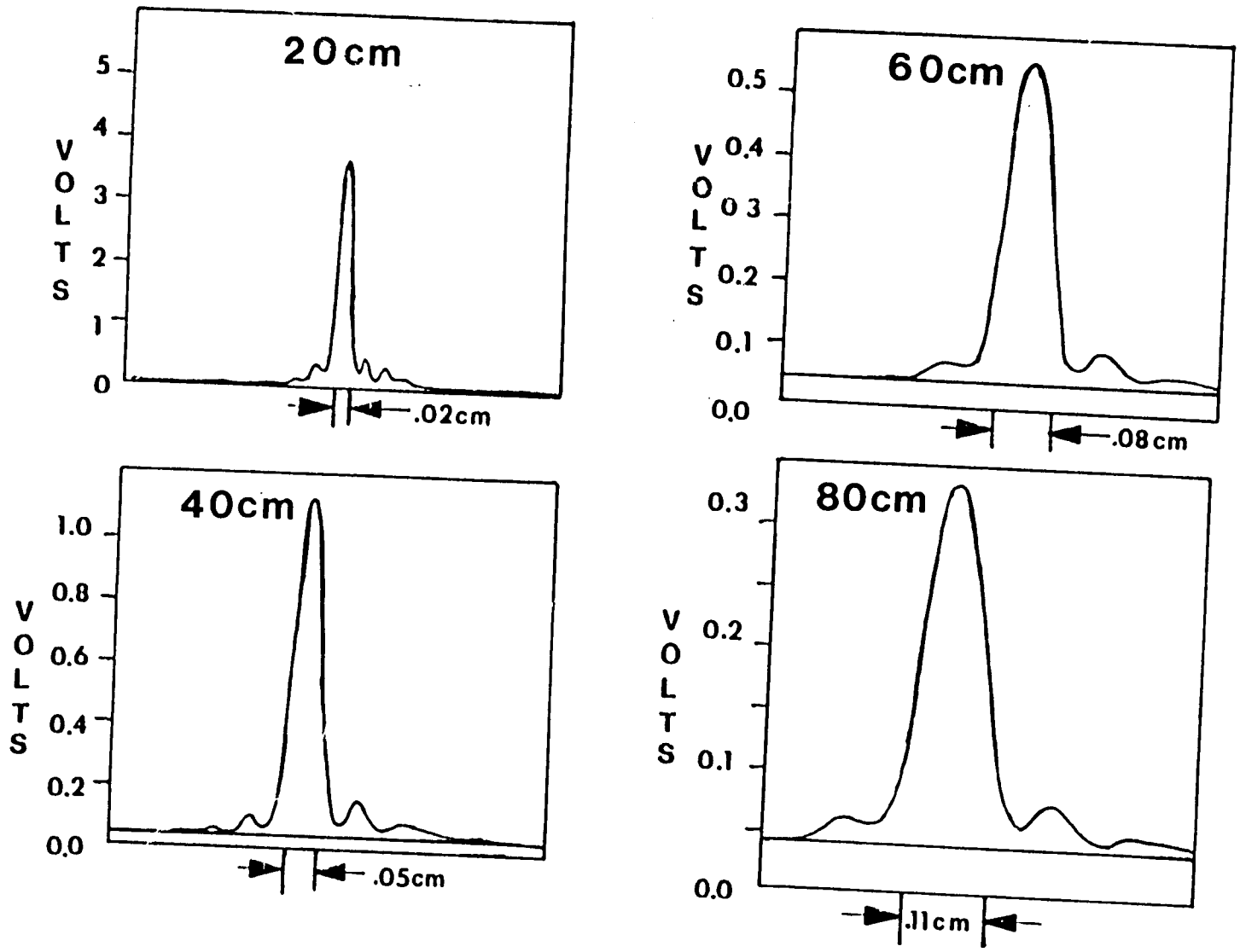

Figure 21c : 2nd Vertical beam scans.

experimental setup is depicted in Figure 22. It consisted of the laser, followed by a concave lens to increase the divergence of the beam, and ultimately focused with a Gallilean collimator. The measured curves were taken at a distance of approximately 3 meters and the calibrated detector described previously was used to accomplish the plotting. The resulting curves are shown in Figure 23. This focusing technique resulted in a 0.3 mm vertical beam width and a 1.4 mm lateral beamwidth.

In order to focus the beam to a smaller spot, its elliptical crossection must be compensated. This can be done by using two cylindrical lenses oriented crossed to each other and aligned with the axes of the laser diode. By placing them at the proper distance from the laser, the convergence angles can be made identical. The calculation to determine the proper distance is presented in Appendix D. The inputs for the calculation are : f = 3.3 mm, g = 1.4 mm, $\alpha = 0.42^{\circ}$, and $\beta = 0.09^{\circ}$. These inputs yield a distance between the diode and the first lens of 8.95 mm, between the diode and the second lens of 12.6 mm, and between the diode and the waist of the focused beam of 14.2 mm. Using these distances an experimental setup was assembled in an attempt to focus the beam. The setup is shown in Figure 24, and it consists of the laser, an adjustable fixture to hold the cylindrical lenses, and a convex lens for focusing the beam. The distances between the lenses were adjusted to give the minimum spot size and the beam was focused about one meter from the diode. Again utilizing the calibrated

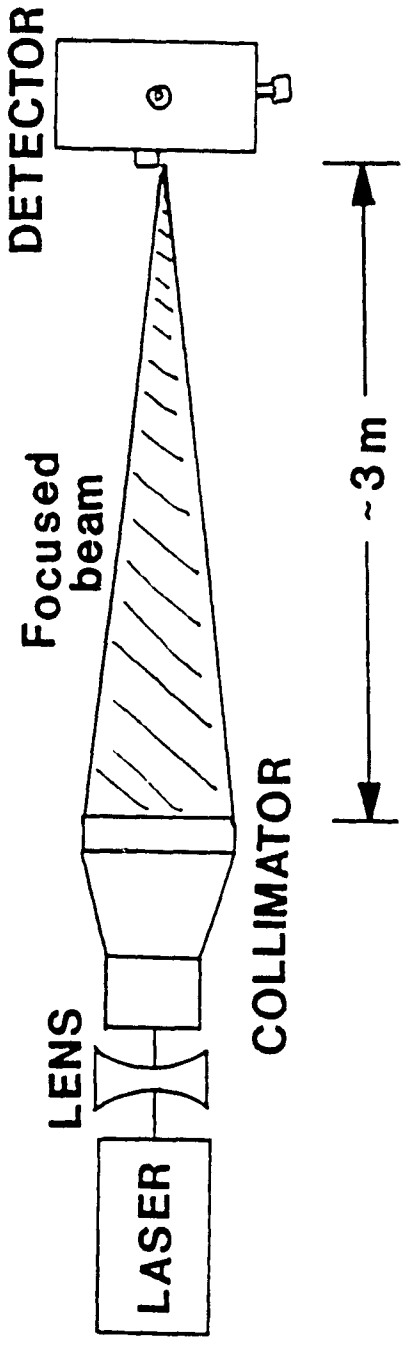

Figure 22 : Uncorrected focusing setup.

Figure 22 : Uncorrected focusing setup.

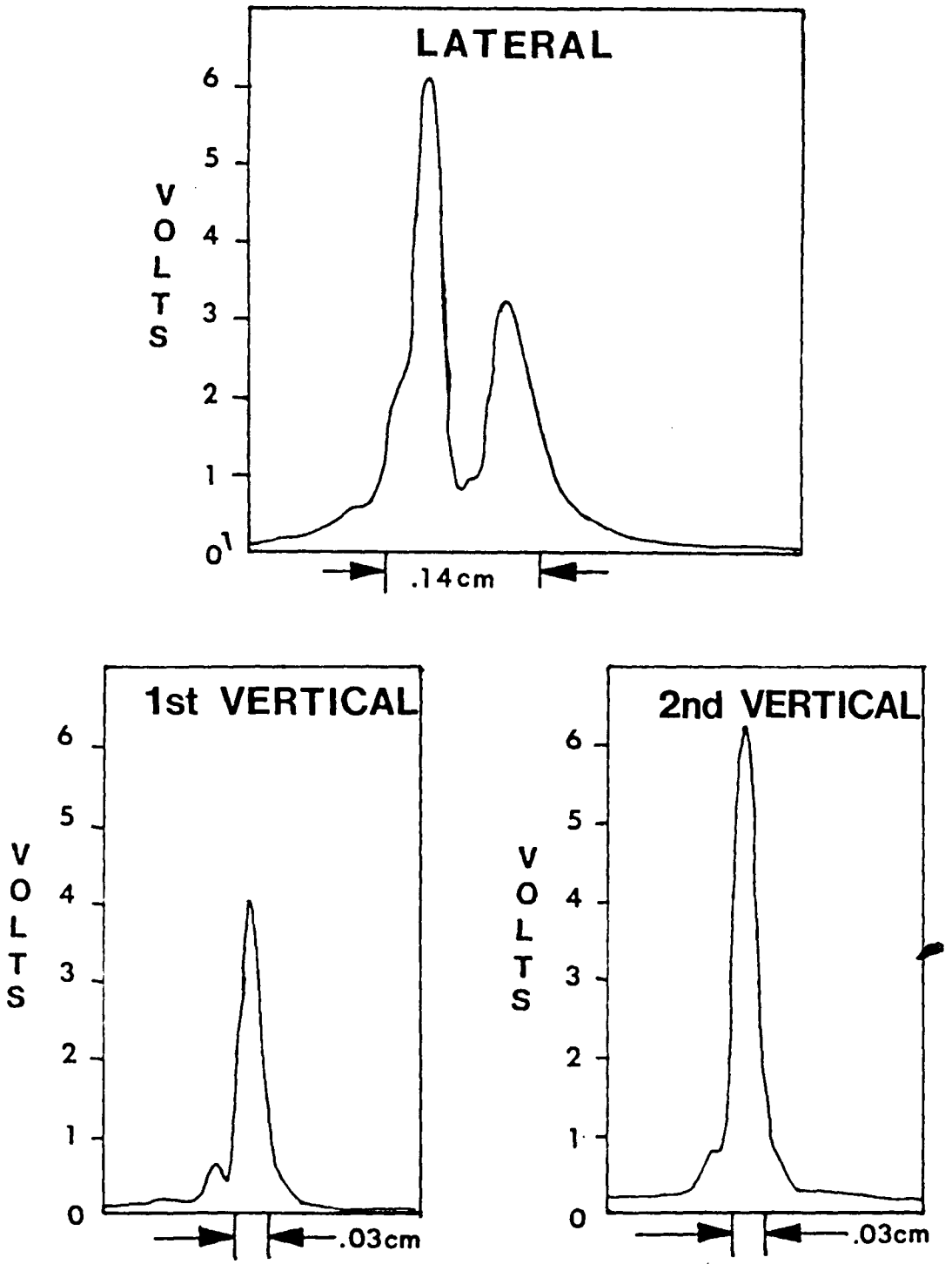

Figure 23 : Uncorrected focusing scans.

detector, beam width curves were plotted. They are presented in Figure 25. The resulting beam widths were approximately 0.2 mm in both directions which is considerably better than obtained above. The primary drawback to this scheme is the large halo surrounding the focused spot, but it is not an extreme problem because it contains little light power. Focusing at larger distances was not attempted due to failure of the laser diode, but this should have given a spot size at three meters comparable to the one meter focused spot size.

The other suitability criterion for the laser diode was the modulation characteristics. Properly housed stripe geometry-lasers can be 100% linearly modulated up to 10 GHz*. The modulation of the Laser Diode Laboratories laser, however, was only demonstratable up to 10 MHz due to the failure of the diode and the housing configuration. Diodes for microwave modulation should become available soon.

In conclusion, the focused spot sizes which can be achieved with stripe-geometry laser diodes are comparable to the spot sizes of focused He-Ne lasers. This was demonstrated with a less than ideal dual-lateral-mode laser diode. Therefore if a better single-lateral-mode laser was used the spot size could be made even smaller. Such devices are presently available.

---

*) Private Communication by Dr. D. Botez, RCA.

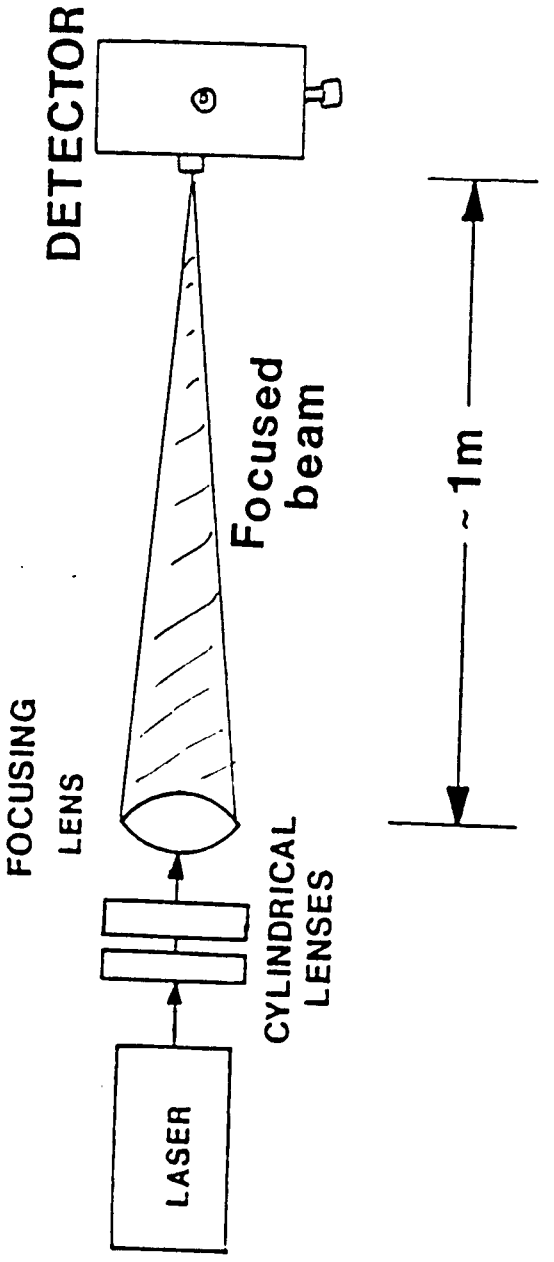

Figure 24 : Elliptically corrected focusing setup

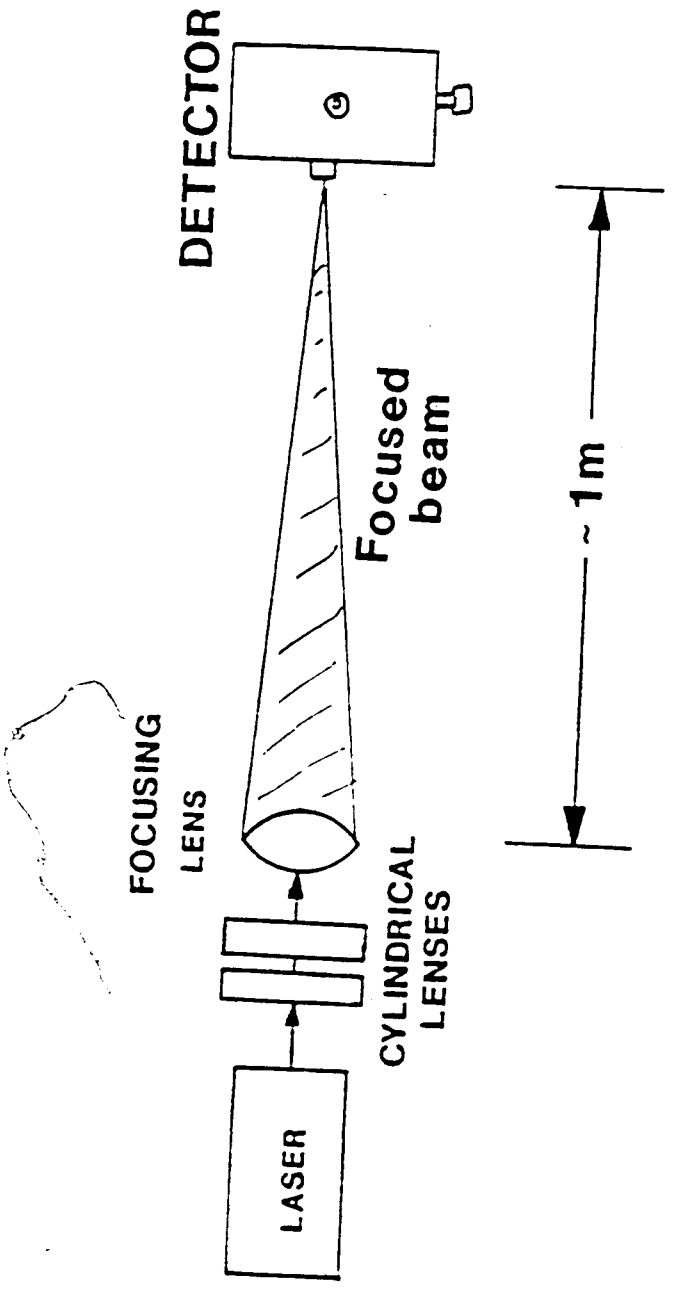

Figure 24 : Elliptically corrected focusing setup

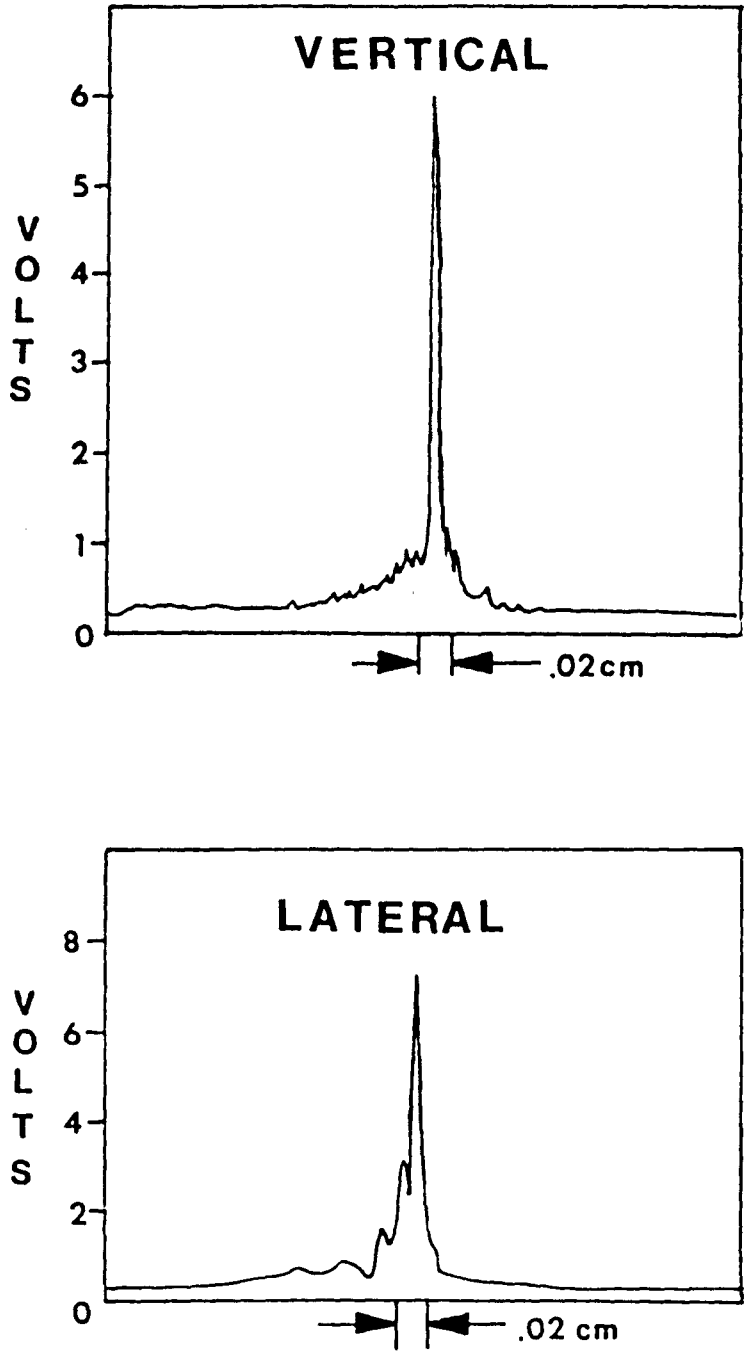

Figure 25 : Elliptically corrected focusing scans

Linear Modulation

Due to the output characteristics of laser diodes, nearly 100% linear modulation can be achieved with them. The modulation process is depicted in Figure 26, for an arbitrary bias b and a peak to peak swing of 2m.

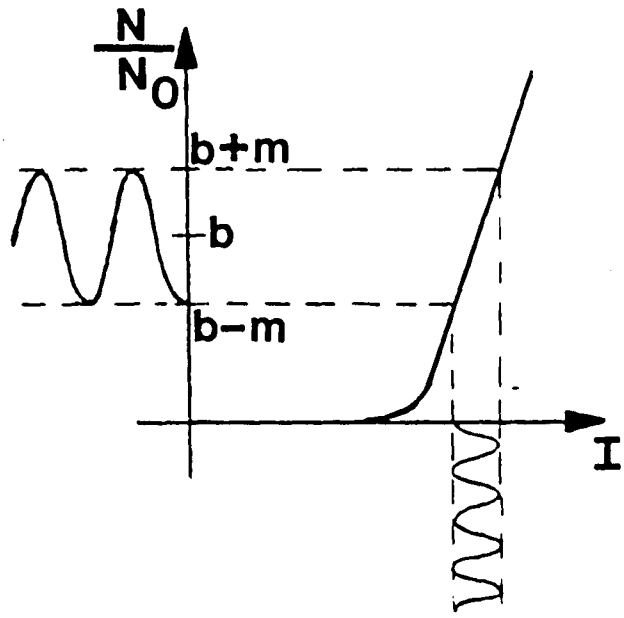

Figure 26 : Modulation of a laser diode.

From the figure the normalized output power can be seen to be :

$$(18) \qquad \frac{N(t)}{N_0} = b + m\cos(\omega_m t + \theta_m)$$

From this equation it is evident that the average light power is just :

$$(19) \qquad \overline{N} = b\,N_0$$

It can also be seen from Eq.(18) that the ω_m frequency component is :

$$(20) \qquad N\omega_m = N_0\, m \cos(\omega_m t + \theta_m)$$

This leads to an RMS signal power of :

$$(21) \qquad N_{RMS} = 0.707\, m\, N_0$$

If roundtrip attenuation is included in the equations the average and RMS light power will be :

$$(22) \qquad \overline{N} = A\, b\, N_0 \qquad \text{and} \qquad N_{RMS} = 0.707\, A\, m\, N_0$$

Solid State Lidar System

Now a solid state Lidar system will be proposed and the performance of such a system calculated. This system would consist of a semiconductor laser, focusing lenses, a telescope, and an avalanche photodiode detector. A diagram of the system is shown in Figure 27. The laser would be a single-mode, stripe-geometry, double heterostructure laser. The focusing system would consist of two crossed cylindrical lenses and a convex spherical lens as described in the chapter on laser diode measurements. The telescope would collect the scattered light from the target. For this system a 4 inch telescope would be used which would yield a scattering loss of 48 dB. The avalanche photodiode detector would then detect the collected light and convert it into an electrical current.

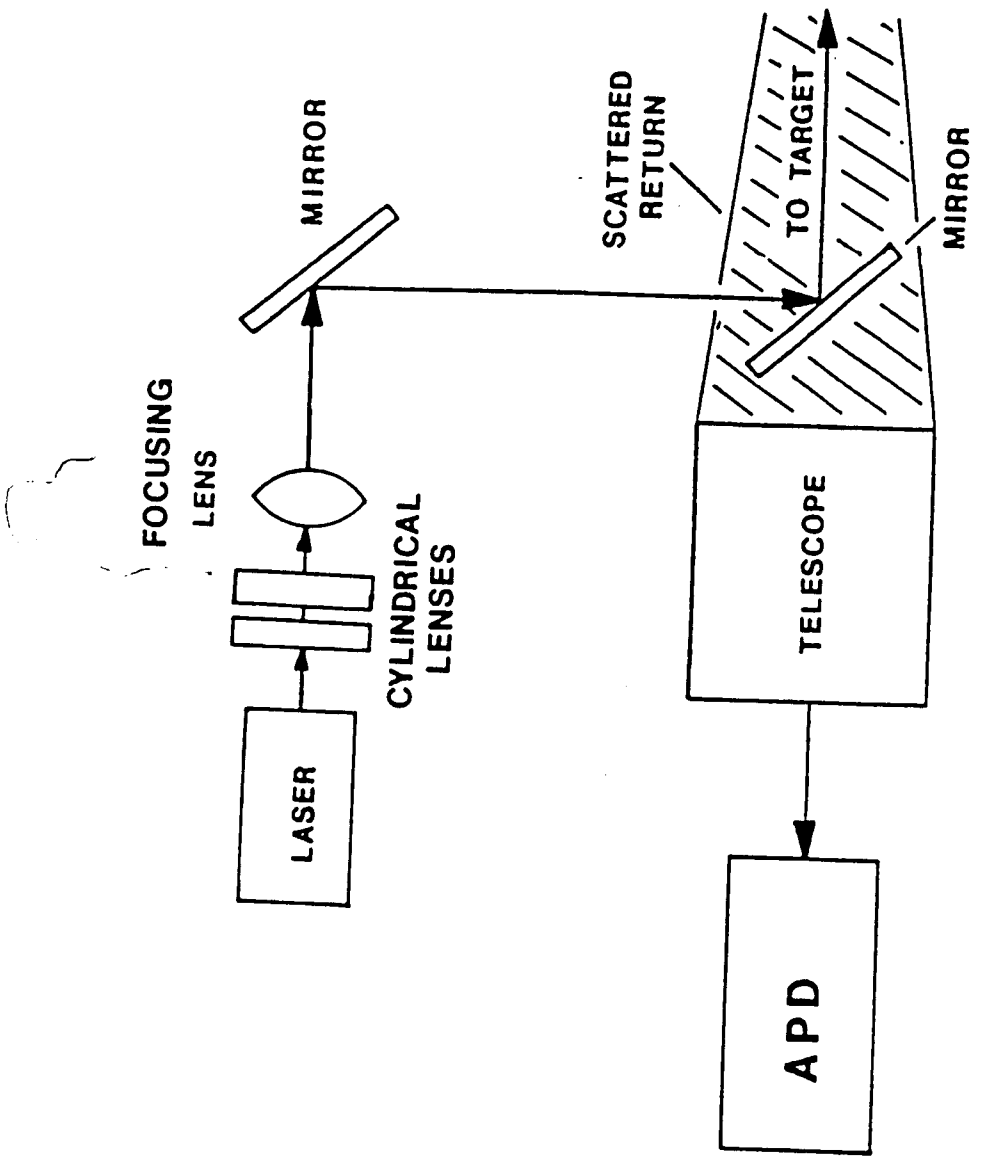

Figure 27 : Solid State Lidar System

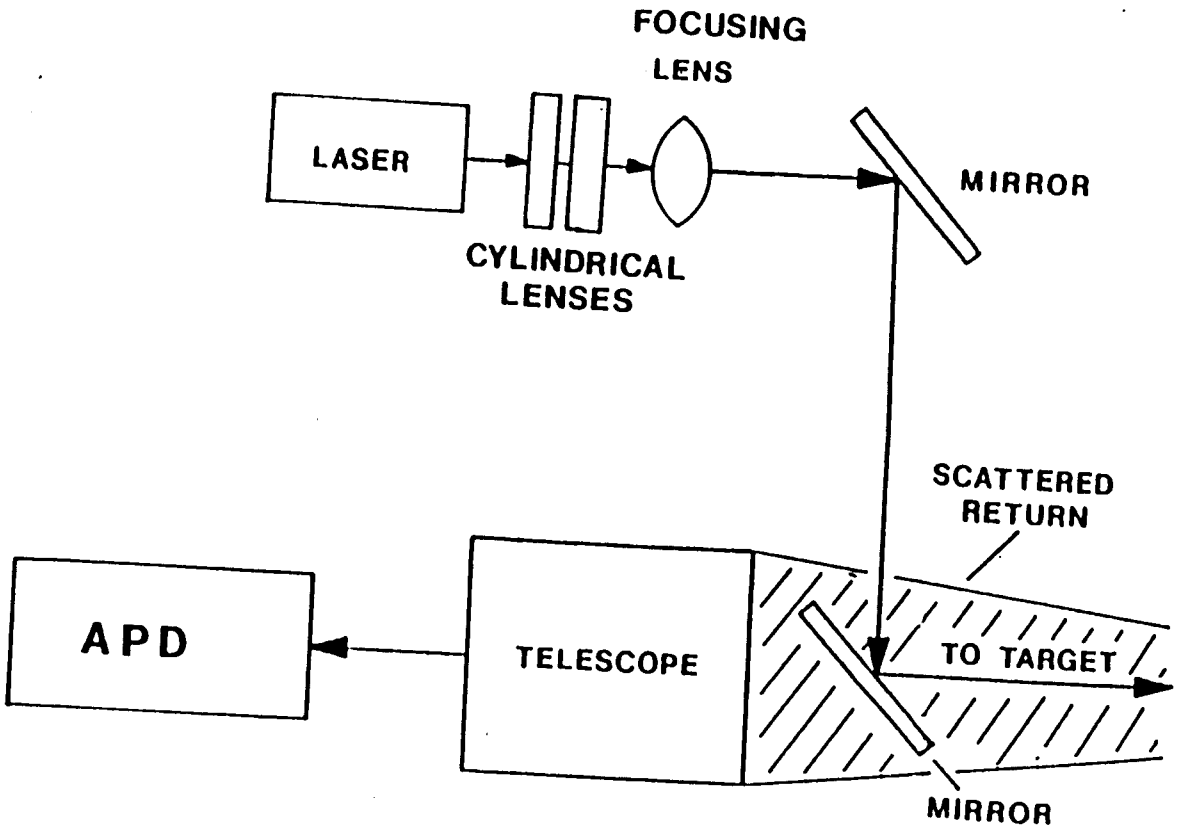

Figure 27 : Solid State Lidar System

The design of this system assumes that a laser becomes available which is packaged and designed for microwave use. For instance the RCA Model No. DB181A in a different package should be useful. It is single-mode in both directions and has an output power of 5 mW at 0.84 μm for single mode operation. The operating characteristics of the laser are shown in Figure 28. Because it is single mode in both directions it should be possible to focus it to a very small spot size and should thus give good performance.

The laser would produce a microwave modulated light beam with nearly 100% linear modulation. The laser beam would then be corrected for the elliptical beam shape per the calculation in Appendix D. The convex lens focuses the beam on the target at approximately 3 meters distance. Next the beam is aligned with the axis of the receiver in the same manner as the present system. If coated lenses and good quality optical mirrors the transmitter attenuation should be less than 2 dB. The scattering loss would then be 48 dB as in the present system. Finally, the telescope loss would be about 2 dB due to the uncoated lenses and the mirror surfaces and therefore the total system attenuation would be 52 dB.

The proposed detector for this system is the Photon Kinetics Silicon APD-1. This photodiode has a responsivity of 0.45 A/W at 0.8 μm, a rise time of 120 ps, avalanche gain of 70, and a detector area of 0.03 mm^2. The 120 ps rise time should give very good frequency response at 2 GHz and thus this frequency was chosen for the microwave modulating signal.

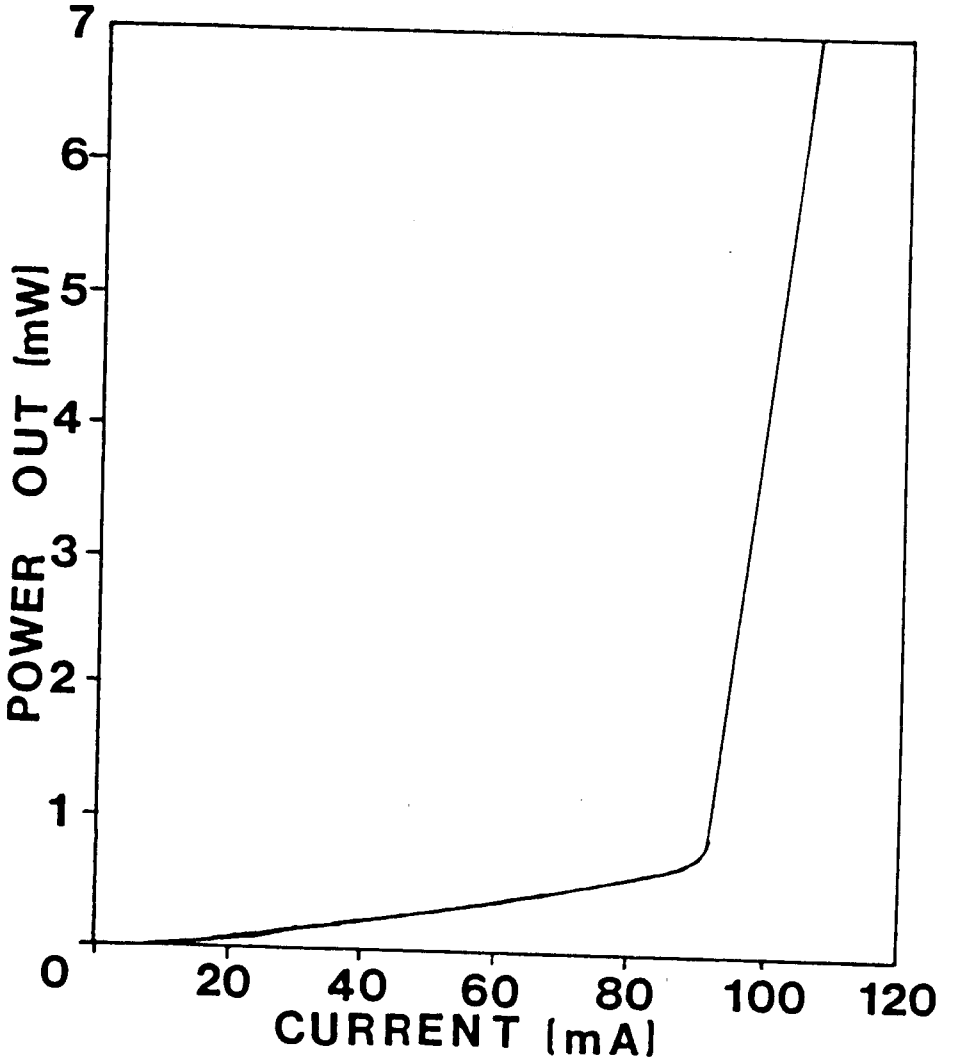

Figure 28 : Operating characteristics of DB181A

The S/N ratio of this system can be determined by substituting Eq.(22) into Eq.(15) to account for the 100% linear modulation. This yields the following :

$$(23)\quad \frac{S}{N} = \frac{A^2 N_0^2 M^2 S^2 m^2}{[[\ 2ei_d + 4e(AN_0bS)]M^2F(M) + 4k\ T_{eff}/\ R_L]\ B}$$

This analysis ignores the noise introduced by the laser diode because after the optical attenuation the diode noise is insignifigant compared to the remaining noise. The laser is operating at 100% modulation and thus $m = b = \frac{1}{2}$. Also needed for the calculation is T_{eff}. For a state of the art F.E.T. amplifier the noise temperature is about 300°K. For Silicon, $i_d = 10^{-9}$ A/cm^2 [3]. The load resistance, R_L, would be 50 ohms, and the amplifier bandwidth would be chosen to be 1 MHz. The final variable to be determined is F(M), the noise degradation factor of the APD. The avalanche gain of this device is 70 and the ionization ratio for Silicon is 0.1 worst case. This yields F(M) = 8.79. Thus the S/N ratio for this system would be 27 dB, which is slightly better than the calculated value for the present system.

The accuracy of this system would be comparable to the present system because the improvement in the signal to noise ratio would be offset by the loss of resolution from using a lower modulating frequency. However in either of the systems, the accuracy is ultimately limited by the resolution of the detector and thus this system should yield somewhat superior performance.

Conclusions

The overall accuracy of the present Lidar system has been verified for the first time and the measured data is in close agreement with the theory. A zero crossing phase detector which is superior to the present cross correlation scheme was presented and analyzed. It was indicated that due to its simplicity and performance the zero crossing detector would be used on future systems. Direct detection was investigated next. An attempt was to receive a CW-microwave signal with a microchannel plate phototube, but this was unsucessful because of the inherently low output current of the device. Direct detection with solid state photodiodes was discussed and a noise analysis presented. It was concluded that devices are available which could be utilized in one of these systems. Next direct modulation with a semiconductor laser was investigated. The focusability of the laser had to be determined to see if the device would be suitable for a Lidar system. A method was evolved for focusing the beam to a spot size similar to a He-Ne laser and thus the suitabiltiy of such devices was verified.

Finally a semiconductor Lidar system was presented. The performance of the system is comparable to the present heterodyning system. The advantages of the semiconductor system are simplicity of operation and cost. The cost of the optical portion of this system would be considerably less than the present system. The simplicity

of operation is demonstrated by the ease of adjustment of the system. Only the mirrors which align the beam would require adjustment and this would be a simple adjustment to give maximum output signal. Additionally this system does not have the thermal warmup and drift problems inherent with the crystal modulators of the present system. Therefore this system would be much better suited to handle the harsh conditions encountered in an industrial environment.

References

1. Eberhardt,N., "Additional Measurements, Review and Conclusions", A Study of CW-Lidar, Lehigh University, 1980.

2. "Design Study of a Lidar System for Close Range Distance Measurements", A thesis by John R. Regazzi, Lehigh University, 1979.

3. Pearsall, T.P., "Photodetectors for Integrated Optics and Fiber Optical Communications" in Fiber and Integrated Optics, ed. Ostrowsky, D.B., Plenum Press, New York, 1978, pp. 141-156.

4. Webb, P.P., McIntyre, R.J., and Conradi, J., R.C.A. Review 35 , 235(1974).

5. Pratt, W.K., Laser Communication Systems, John Wiley and Sons, Inc., New York, 1969, pp. 87-110.

6. Casey, H.C., Panish, M.B., Heterostructure Lasers Part B : Material and Operating Characteristics, Academic Press, New York, 1978, pp. 174-276.

7. National Semiconductor TTL Data Book, Santa Clara, California, National Semiconductor Corporation, 1977, pp. 75-178.

8. RCA CMOS Data Book, Somerville, N.J., RCA Solid State Division, 1978, pp. 177-263.

9. Denton, R.T., Chan, F.S., Bakman, A.A., Lithium Tantalate Light Modulators, Journal of Applied Physics, Volume 38, No. 4, pp. 1611-1617, 15 March 1967.

10. Kaminov, Ivan P., Introduction to Electrooptic Devices, Academic Press, New York, 1974, pp. 73-87.

11. Kressel, H., Butler, J.K., Semiconductor Lasers and Heterojunction LEDs, Academic Press, New York, 1977, pp. 78-167.

12. Barnowski, M.K., Fundamentals of Optical Fiber Communications, Academic Press, New York, 1976, pp.109-181.

13. Botez, Dan, "InGaAsP/InP Double-Heterostrusture Lasers : Simple Expressions for Wave Confinement Beamwidth, and Threshold Current over Wide Ranges in Wavelength(1.1 - 1.65 μm)" I.E.E.E. Journal of Quantum Electronics, Volume QE-17, No. 2, February 1980.

Appendix A : Schematic of Lidar Interface.

Control and Handshaking Circuitry

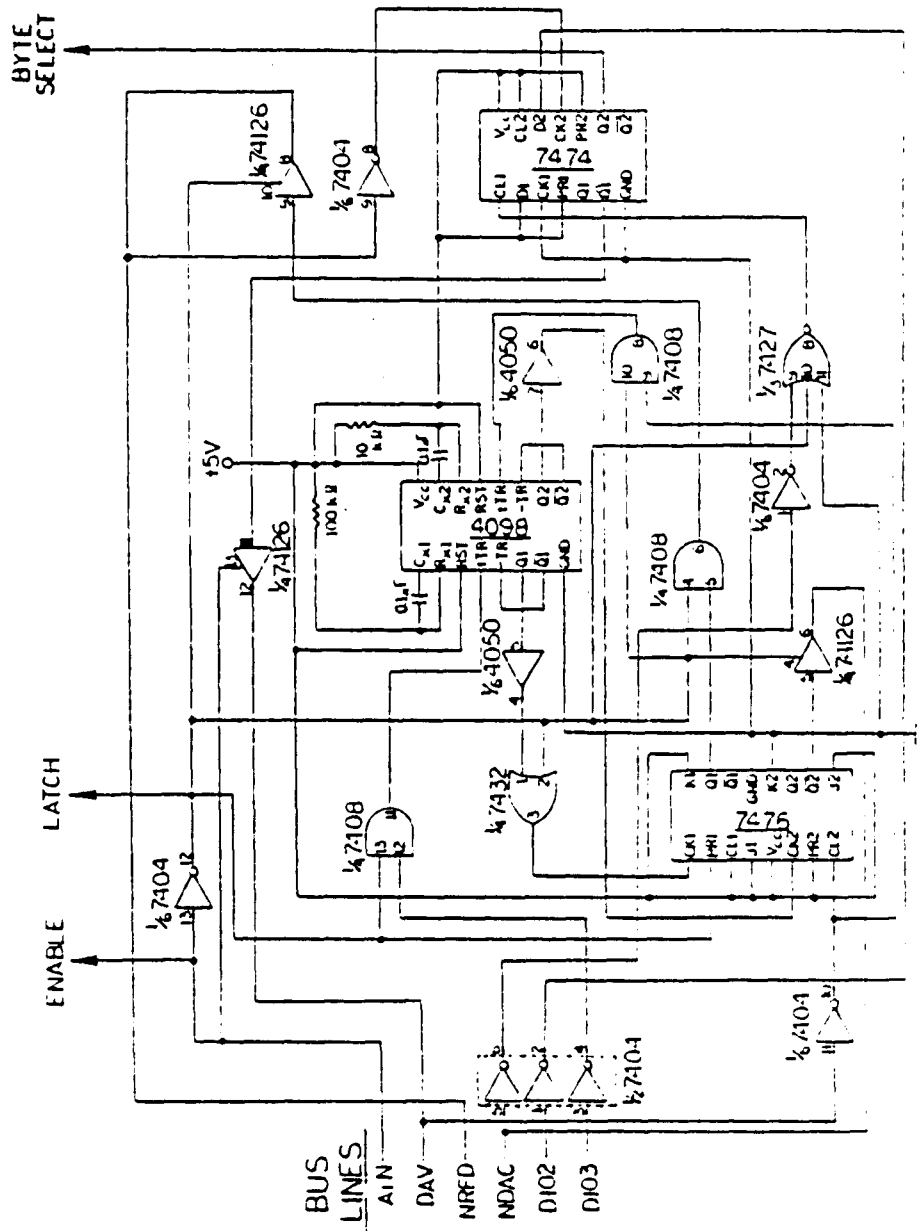

Appendix A : Schematic of Lidar Interface.

Control and Handshaking Circuitry

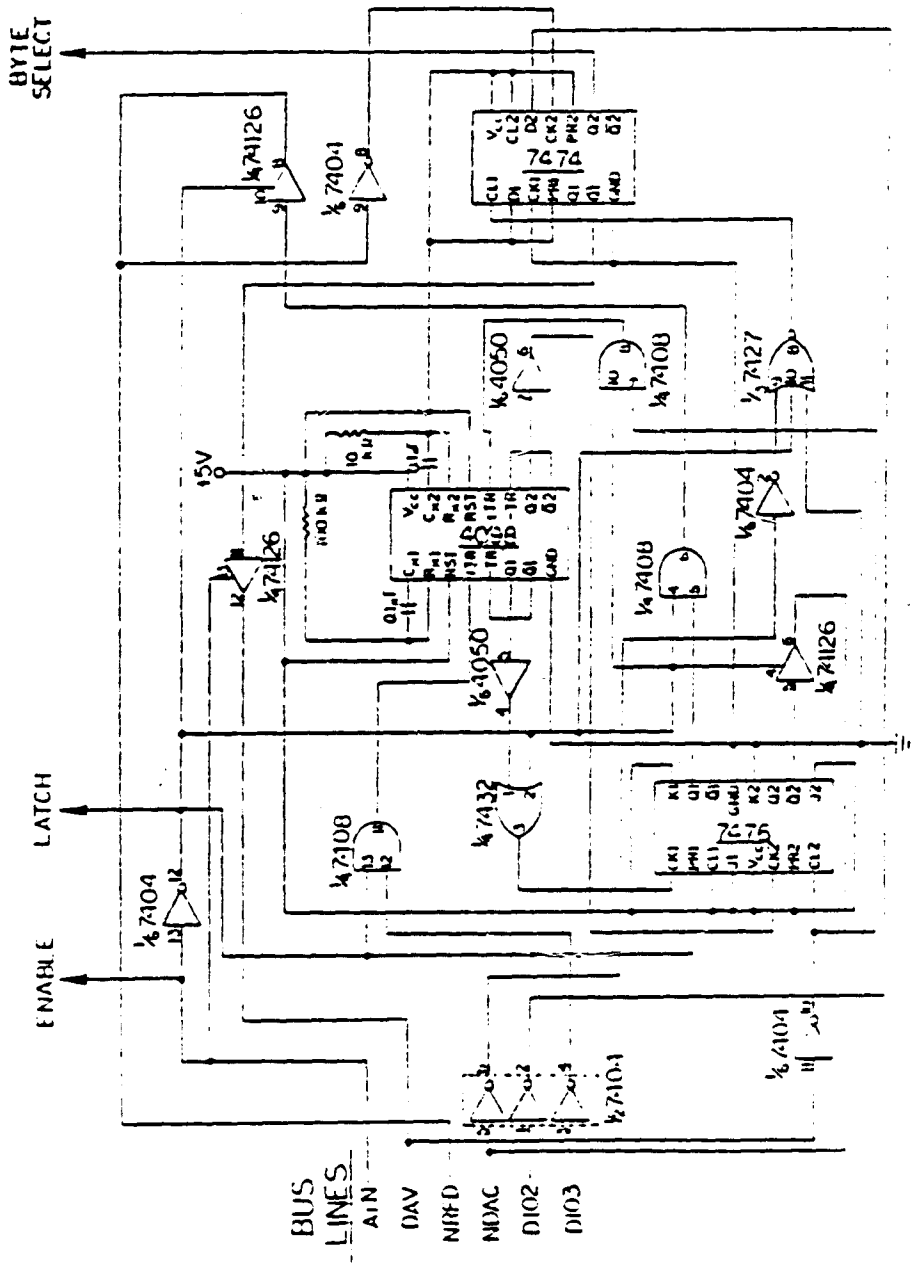

DATA SELECTION CIRCUITRY

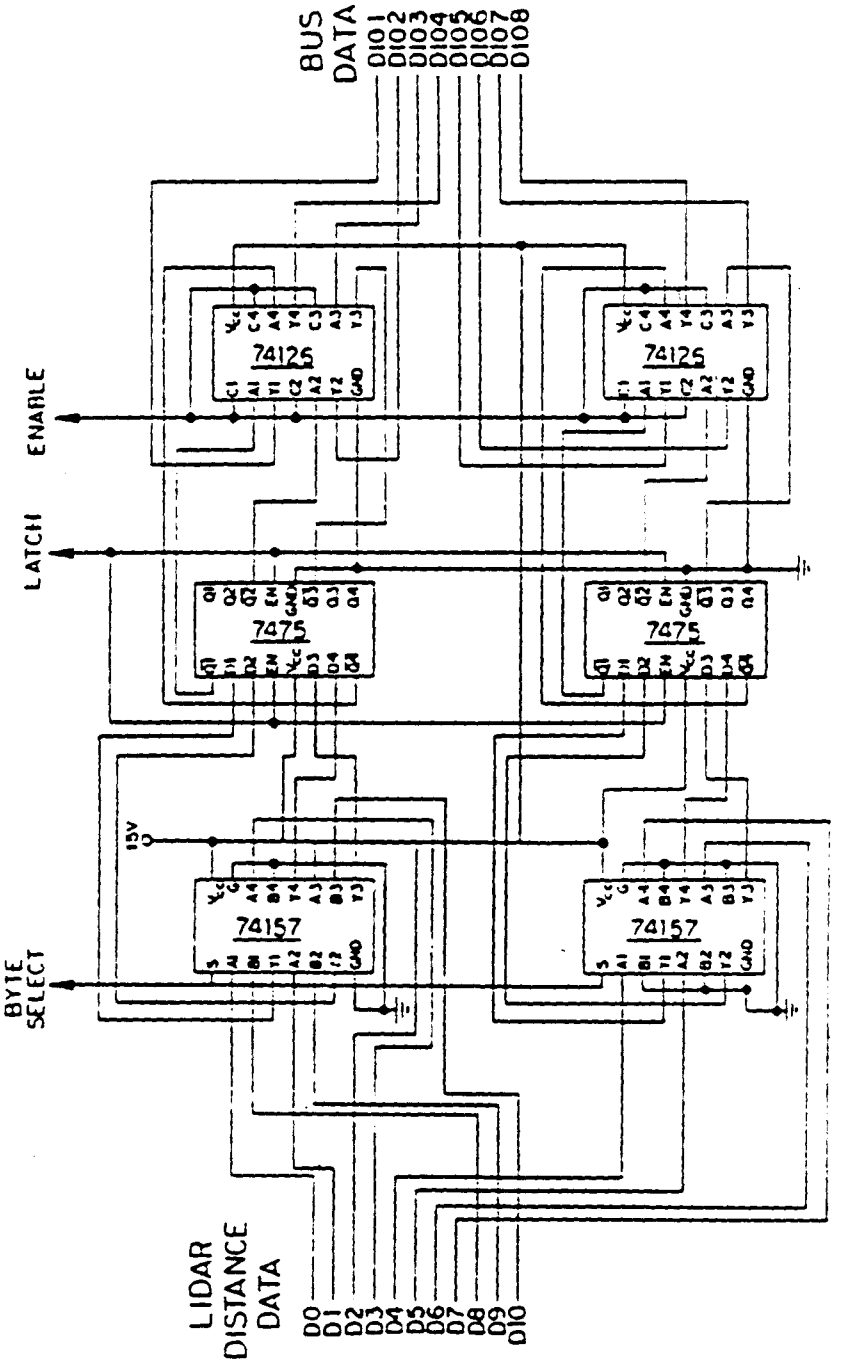

Timing Diagram for Interface

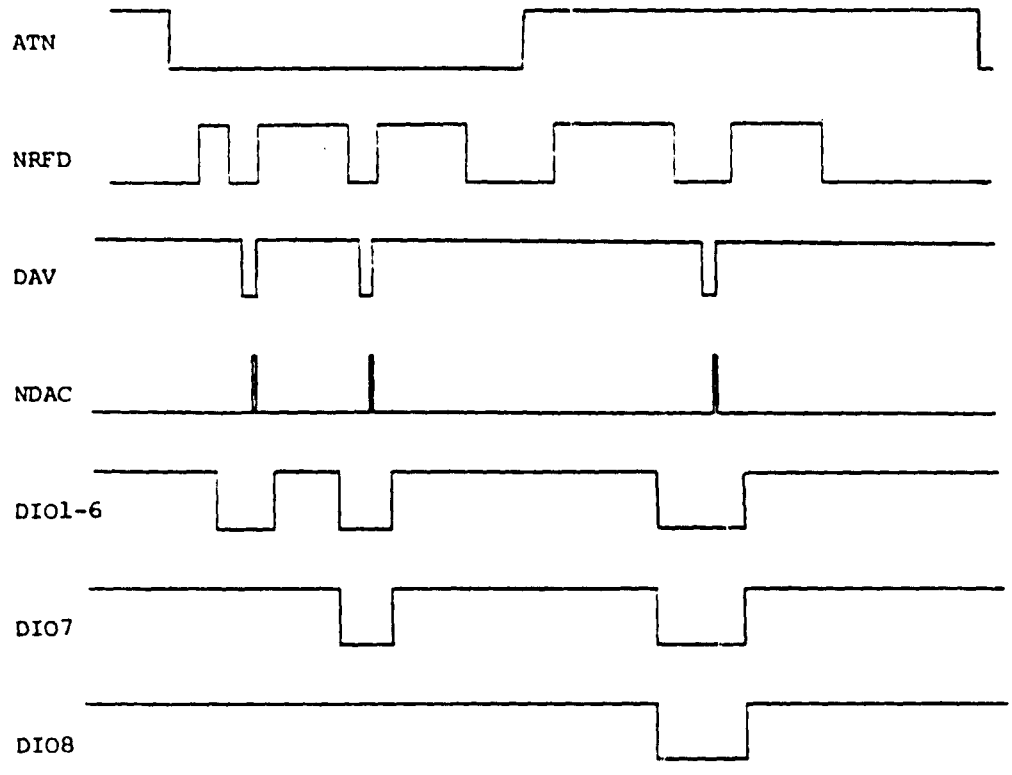

APPENDIX B : LOW PASS FILTER CIRCUIT AND ANALYSIS

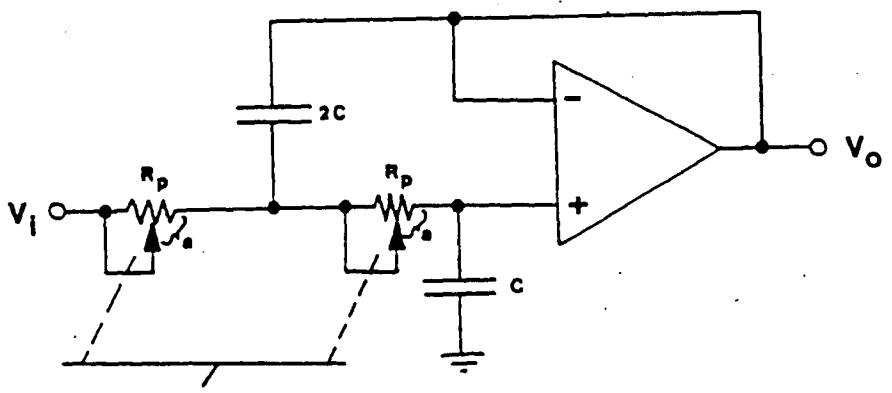

$$R = a\,R_p$$

$$V_o = \frac{1}{s\,C}\,I_1 \quad : \quad I_1 = sCV_o$$

$$I_1\,R = I_2\,\frac{1}{2sC}$$

$$I_2 = 2sCR\,I_1 = 2(sC)^2 R\,V_o$$

$$V_o = V_i - (I_1 + I_2)\,R - I_1\,R$$

$$V_o\,(1 + sCR + 2(sCR)^2 + sCR) = V_i$$

$$\frac{V_o}{V_i} = \frac{1}{1 + 2sCR + 2(sCR)^2} = \frac{1}{-2(f/f_o)^2 + 2j(f/f_o) + 1}$$

$$\left|\frac{V_o}{V_i}\right| = \frac{1}{\sqrt{(2f/f_o)^2 + [1 - 2(f/f_o)^2]^2}} = \frac{1}{\sqrt{1 + 4(f/f_o)^4}}$$

$$f_o = 1.414\,f_{3dB}$$

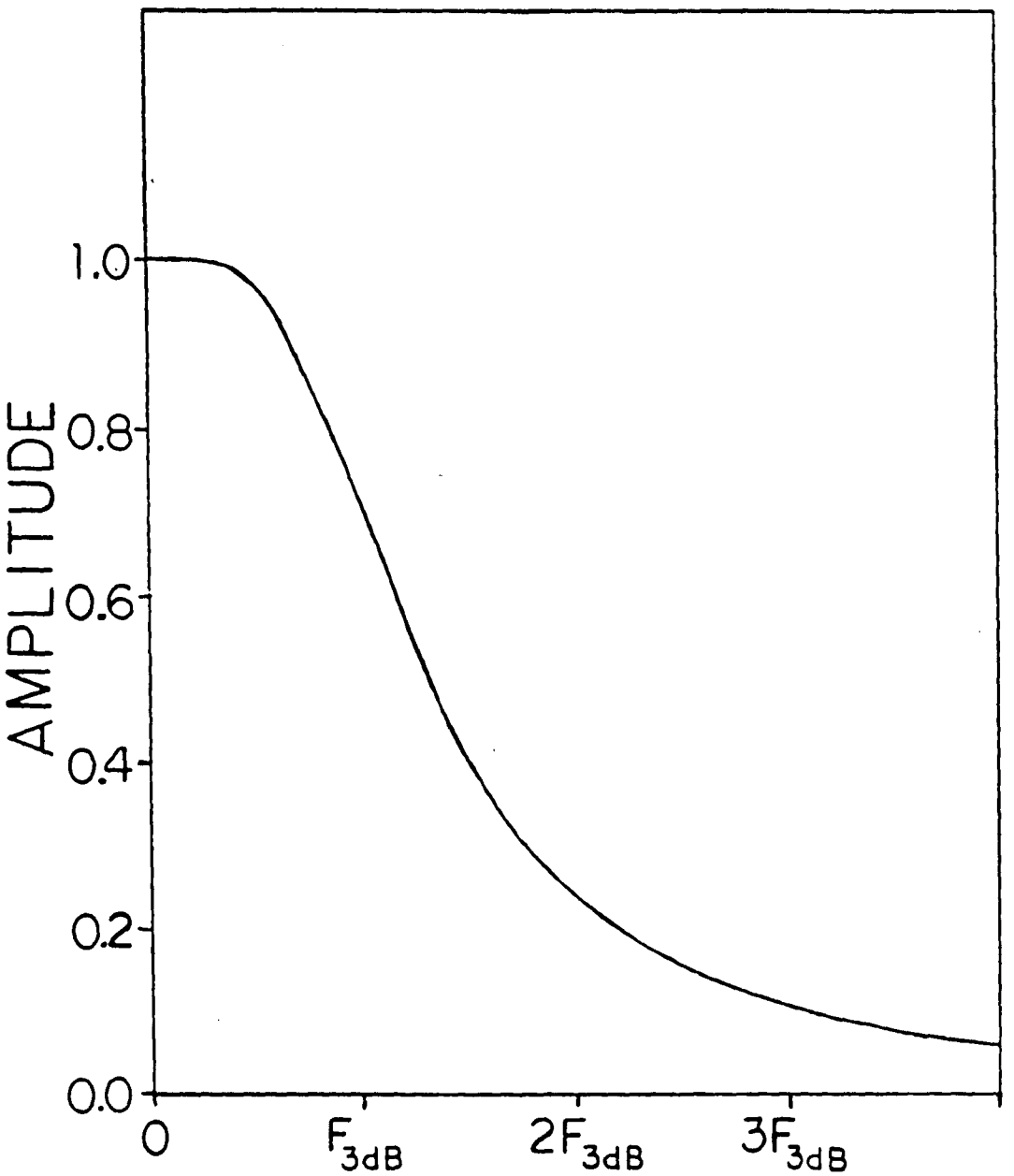

LOW PASS FILTER RESPONSE

APPENDIX C : Flowchart for theoretical curve plotting program.

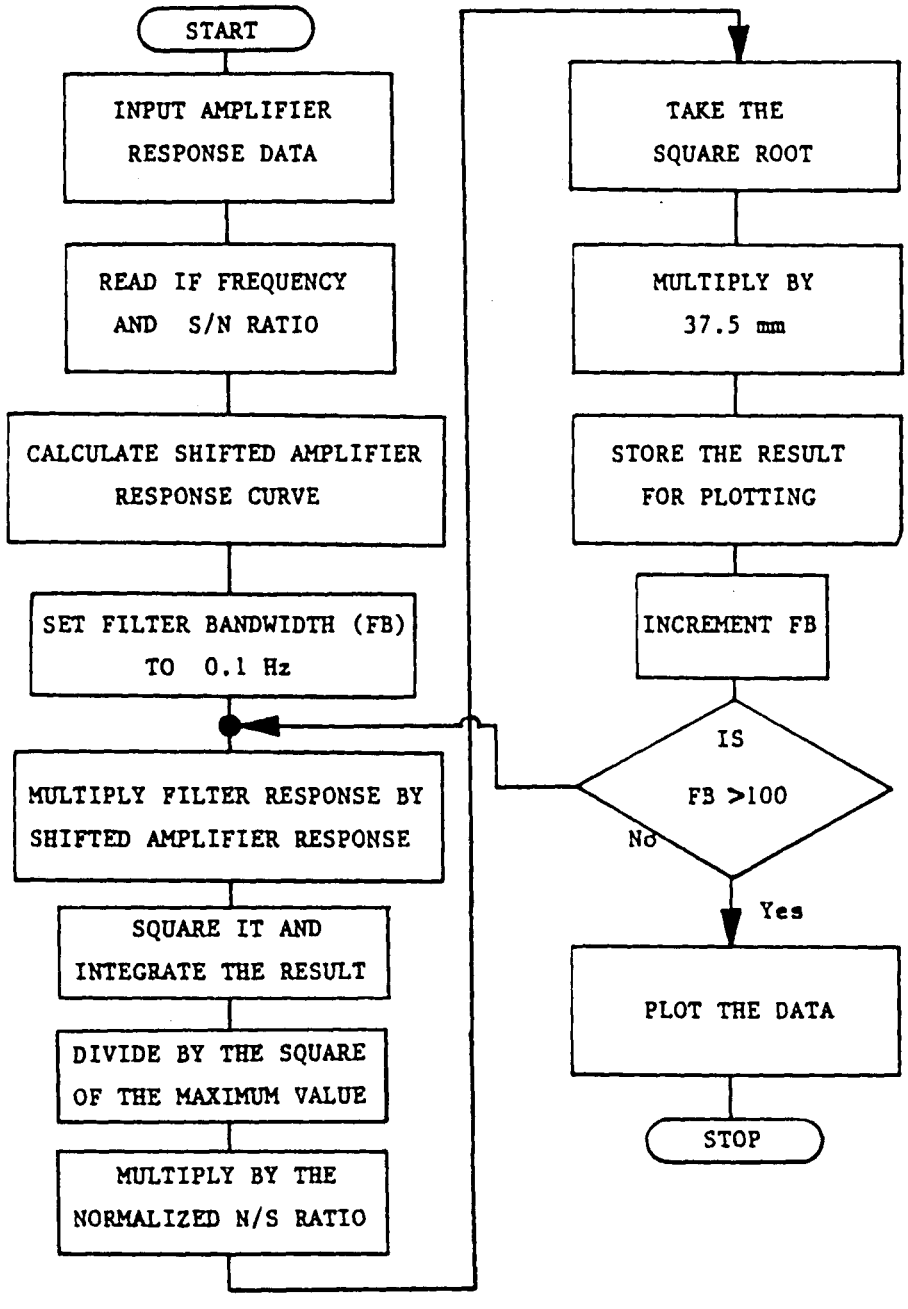

APPENDIX D : Laser Focusing Calculation.

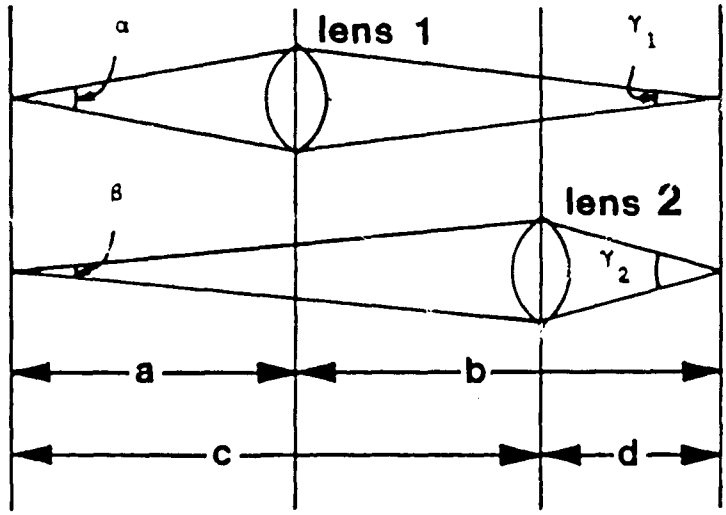

$a + b = c + d$

f is the focal length of lens 1

$$\frac{1}{a} + \frac{1}{b} = \frac{1}{f}$$

g is the focal length of lens 2

$$\frac{1}{c} + \frac{1}{d} = \frac{1}{g}$$

Want to force $\gamma_1 = \gamma_2$

h_1 = size of the image at a in the vertical plane

h_2 = size of the image at c in the horizontal plane

$$h_1 = 2a \tan(\alpha/2)$$

$$\gamma_1 = 2 \tan^{-1}(h_1/2b) = 2 \tan^{-1}[(a/b)\tan(\alpha/2)]$$

$$h_2 = 2c \tan(\beta/2)$$

$$\gamma_2 = 2 \tan^{-1}(h_2/2d) = 2 \tan^{-1}[(c/d)\tan(\beta/2)]$$

Set $\gamma_1 = \gamma_2$

$$2 \tan^{-1}[(c/d)\tan(\beta/2)] = 2 \tan^{-1}[(a/b)\tan(\alpha/2)]$$

$$\frac{c}{d} \tan(\beta/2) = \frac{a}{b} \tan(\alpha/2)$$

$$\frac{a}{b} = \frac{\tan(\beta/2)}{\tan(\alpha/2)} \frac{c}{d} = K \frac{c}{d}$$

where $K = \frac{\tan(\beta/2)}{\tan(\alpha/2)}$

$$\frac{1}{a} + \frac{1}{b} = \frac{1}{f} \quad : \quad \frac{1}{b} = \frac{1}{f} - \frac{1}{a} \quad : \quad b = \frac{1}{1/f - 1/a} = \frac{a f}{a - f}$$

$$\frac{1}{c} + \frac{1}{d} = \frac{1}{g} \quad : \quad \frac{1}{d} = \frac{1}{g} - \frac{1}{c} \quad : \quad d = \frac{1}{1/g - 1/c} = \frac{c g}{c - g}$$

From above $\frac{a}{b} = K \frac{c}{d}$

$$a \left(\frac{1}{f} - \frac{1}{a}\right) = Kc \left(\frac{1}{g} - \frac{1}{c}\right)$$

$$\frac{a}{f} - 1 = K \frac{c}{g} - K$$

$$\frac{a}{f} = K \frac{c}{g} + (1 - K)$$

$$a = Kc \frac{f}{g} + (1 - K) f$$

From above $a + b = c + d$

$$a + \frac{a f}{a - f} = c + \frac{c g}{c - g}$$

$$[a^2/(a - f)] = [c^2/(c - g)]$$

$$\frac{[Kc(f/g) + (1 - K)f]^2}{[Kc(f/g) + (1 - K)f - f]} = \frac{c^2}{c - g}$$

$$\frac{[Kc(f/g) + (1 - K)f]^2}{K(f/g)\,[c - g]} = \frac{c^2}{c - g}$$

$$[Kc\,\frac{f}{g} + (1 - K)f] = (K\,\frac{f}{g})^{1/2}c$$

$$c = \frac{(1 - K)\,f}{(K\,\frac{f}{g})^{1/2} - (K\,\frac{f}{g})}$$

For a solution to exist : $(K\,\frac{f}{g})^{1/2} > (K\,\frac{f}{g})$

Which implies : $(K\,\frac{f}{g}) < 1$

From above : $a = Kc\,\frac{f}{g} + (1 - K)\,f$

So : $a = \frac{(1 - K)\,f}{(K\,\frac{f}{g})^{-1/2} - 1} - (1 - K)\,f$

Once a is calculated a+b can be determined from :

$$a + b = \frac{a^2}{a - f}$$

Vita

Ralph Wallis Kettell,II was born on July 17,1959 in Baltimore, Maryland and is the son of Nadine B. Kettell of Baltimore. He graduated with high honors from Lehigh University in June, 1980 with a Bachelor of Science degree in Electrical Engineering. He is a member of Tau Beta Pi and Eta Kappa Nu honoraries. He was employed from August, 1980 through August, 1981 as a research Assistant in the Department of Electrical Engineering at Lehigh University. Presently he is employed as an engineer at Bendix Environmental and Process Instrumention Division. Publications include "Metabolism of 1-Hydroxybenzo[a]pyrene", in Chem.-Biol. Interactions 36(1981), and a paper on Computer Graphics Simulation of DNA and RNA Molecular Chains which is presently being published.